

# **Mixed layer heat and salinity variability in the equatorial Atlantic**

**Dissertation**

ZUR ERLANGUNG DES DOKTORGRADES  
DER MATHEMATISCH - NATURWISSENSCHAFTLICHEN FAKULTÄT  
DER CHRISTIAN-ALBRECHTS-UNIVERSITÄT ZU KIEL

VORGELEGT VON  
MICHAEL SCHLUNDT  
KIEL, APRIL 2014





Referent:	Prof. Dr. Peter Brandt
Koreferent:	Prof. Dr. Claus Böning
Tag der mündlichen Prüfung:	19.06.2014
Zum Druck genehmigt:	19.06.2014

---

gez. Prof. Dr. Wolfgang J. Duschl, Dekan





# Zusammenfassung

Das bemerkenswerteste Phänomen der Meeresoberflächentemperatur im tropischen Atlantik ist das saisonale Auftreten der atlantischen Kaltwasserzunge (Atlantic Cold Tongue (ACT)). Die ACT, charakterisiert durch stark reduzierte Temperaturen, entwickelt sich im späten borealen Frühling/ frühen Sommer mit dem Erstarren der Südostpassate entlang des Äquators und hält an bis zum späten Herbst/ frühen Winter. Beginn, Dauer, räumliche Ausdehnung und Stärke der Abkühlung unterscheiden sich stark von Jahr zu Jahr. Das Wärmebudget in der Deckschicht ist einigermaßen bekannt, aber nur an bestimmten Positionen bestimmt oder aus Modellergebnissen abgeleitet. Die Rolle des oberflächennahen Salzgehaltes für den ACT-Beginn und -entwicklung und das Salzgehaltsbudget der Deckschicht sind weit weniger verstanden.

In dieser Arbeit wurden Veränderungen der Temperatur und des Salzgehaltes in der Deckschicht von Mai bis Juli 2011 in einem Kaltwasserzungenexperiment (CTE) untersucht. Das CTE basiert auf zwei aufeinanderfolgenden Seereisen, einem Gleiterschwarmexperiment und verankerten Beobachtungen. Der in-situ Datensatz wurde zusammen mit Satellitendaten, atmosphärischen Reanalysedaten und den Ergebnissen eines Assimilationsmodells benutzt um das Wärme- und Salzgehaltsbudget in der Deckschicht in zwei Regionen zu untersuchen: 1) der westlichen ACT zwischen  $23^{\circ}\text{W}$  und  $10^{\circ}\text{W}$ , eine Region starker Abkühlung während des CTE und 2) einer Region nördlich der ACT, welche durch die nordwärtige Bewegung der Innertropischen Konvergenzzone beeinflusst ist. Die Ergebnisse des Jahres 2011 wurden mit den mittleren Jahresgängen an drei Oberflächenbojen verglichen ( $0^{\circ}\text{N}$ ,  $23^{\circ}\text{W}$ ;  $4^{\circ}\text{N}$ ,  $23^{\circ}\text{W}$ ;  $0^{\circ}\text{N}$ ,  $10^{\circ}\text{W}$ ).

Der starke Wärmeverlust der Deckschicht in der ACT-Region während des CTE ist das Ergebnis einer Erwärmung durch den Nettooberflächenwärmefluss und der Abkühlung durch diapyknische Vermischung an der Basis der Deckschicht und zonale Advektion, welche sich bilanzieren. Die dominierende Rolle der diapyknischen Vermischung wurde sowohl durch Beobachtungen als auch durch Herleitung aus dem Residuum bestimmt. In der nördlichen Region wurde eine schwache Abkühlung durch ähnliche große Anteile des Nettowärmeflusses, der zonalen Advektion und des Entrainments beobachtet. Nur ein

vernachlässigbares Residuum wurde in der Region nördlich der Kaltwasserzunge berechnet.

Während des CTE stieg der Deckschichtsalzgehalt in der ACT-Region leicht an. Ein Süßwassereintrag durch stark variierende zonale Advektion und ein Salzgehaltsanstieg durch den Nettosüßwasserfluss führen zu dieser Bilanz. Ein starker Salzgehaltsanstieg ereignete sich kurz vor dem CTE am Äquator bei 10°W Länge und wurde durch die CTE-Beobachtungen nicht erfasst. Wenn die diapyknische Vermischung mitbetrachtet wird, welche den stark salzhaltigen Kern des äquatorialen Unterstroms erodiert, konnte das errechnete Residuum nur teilweise verkleinert werden. In der Region nördlich der Kaltwasserzunge sorgte der starke Süßwassereintrag durch Niederschlag zu Beginn des CTE zu einer Salzgehaltserniedrigung in der Deckschicht. Zonale Advektion änderte das Vorzeichen während des CTE und trug zuerst zur Salzmindern und später zum Salzgehaltsanstieg bei.

Die Salzgehaltsbilanz am Äquator ist charakterisiert durch schwache saisonale Änderungen. Während des ersten Halbjahres werden Veränderungen des Deckschichtsalzgehaltes durch Süßwassereinträge von Niederschlag, zonaler Advektion und Wirbeladvektion mit Salzgehaltserhöhungen durch Verdunstung, meridionaler Advektion und Entrainment bilanziert. In der westlichen Kaltwasserzungenregion sorgt zusätzlich ein Salzeintrag durch diapyknische Vermischung für eine ausgeglichene Bilanz. Meridionale Advektion sorgt für einen Salzgehaltsanstieg in der ACT-Region, welcher selber nur in schwachem Ausmaß beobachtet wird. Speziell in der zentralen ACT-Region bleibt ein großes Residuum im Sommer und Herbst über, welches im Sommer unter Berücksichtigung von wenigen Messungen diapyknischen Salzflusses teilweise verkleinert werden kann. An der nördlichen Bojenposition (4°N) ist der Jahresgang des Deckschichtsalzgehaltes durch den Halbjahresgang des Niederschlags und der meridionalen Advektion und den Jahresgang des Entrainments und der Wirbeladvektion beschrieben.

# Abstract

The most striking sea surface temperature (SST) phenomenon in the tropical Atlantic is the seasonal appearance of the Atlantic Cold Tongue (ACT). The ACT, characterized by strongly reduced temperatures, develops in late boreal spring/early summer with the strengthening of the southeast trades along the equator and last until late fall/early winter. Onset, duration, spatial extent and strength of cooling vary significantly from year to year. The mixed layer (ML) heat budget terms in the ACT region are rather well estimated, but only locally or with model results. The role of near-surface salinity variations for ACT onset and development as well as the mixed layer salinity budget are less understood.

In this thesis ML temperature and salinity (MLS) changes during ACT development were studied from May to July 2011 by a cold tongue experiment (CTE). The CTE was based on two successive research cruises, a glider swarm experiment, and moored observations. This in-situ dataset together with satellite data, atmospheric reanalysis data, and assimilation model output were used to evaluate the ML heat and salinity budget for two sub-regions: 1) the western ACT between 23°-10°W showing strong cooling during the CTE and 2) the region north of the ACT influenced by the northward migrating Intertropical Convergence Zone. The findings of the year 2011 were compared with mean seasonal cycles at three buoy sites (0°N, 23°W; 4°N, 23°W; 0°N, 10°W).

The strong ML heat loss in the ACT region during the CTE was found to be the result of the balance between warming due to net surface heat flux and cooling due to diapycnal mixing and zonal advection. The dominant role of diapycnal mixing was observed as well as conjectured from the residual of the heat budget by using estimated diapycnal diffusivities and vertical temperature gradients at the base of the ML. In the region north of the ACT the weak cooling was achieved by similar contributions of net surface heat flux, zonal advection and entrainment. Only a small residual remained in the region north of the ACT.

During the CTE, salinity in the ACT region slightly increased with a balance of overall freshening due to strongly varying zonal advection and salinity increase due to the net surface freshwater flux. A strong salinity increase in the ACT region occurred at the

equator,  $10^{\circ}\text{W}$  before the CTE and was not captured by our measurements. The diapycnal mixing, which act to erode the high salinity core of the Equatorial Undercurrent, could only partly be related to the remaining residual. In the region north of the ACT, stronger precipitation resulted in a freshening effect due to a net surface freshwater flux. Zonal advection changed sign during the CTE contributing to a ML freshening at the beginning of the CTE and a salinity increase afterward.

The salinity balance at the equator is characterized by weak seasonal changes. In the first half of the year the MLS changes are caused by the freshening due to precipitation, zonal advection and eddy salt advection, which are balanced by the salinity increasing contribution of evaporation, meridional salt advection and entrainment. In the western cold tongue region, a diapycnal salt flux during February/March and in June is a salt gain for the ML. Meridional salt advection increases MLS during the second half of the year in the cold tongue region. In particular in the central cold tongue region an imbalance during summer and fall remains. In summer this imbalance can be minimized by the implementation of the diapycnal salt flux. At the northern buoy at  $4^{\circ}\text{N}$  the seasonal cycle of MLS is caused by the semiannual cycle of precipitation and meridional advection and the annual cycle of entrainment and eddy salt advection.

# Contents

<b>1</b>	<b>Introduction</b>	<b>1</b>
<b>2</b>	<b>Tropical Atlantic</b>	<b>7</b>
2.1	Temperature . . . . .	8
2.2	Salinity . . . . .	12
2.3	Atmospheric parameters . . . . .	16
2.4	Currents . . . . .	19
<b>3</b>	<b>Data and Methodology</b>	<b>23</b>
3.1	Box averaging strategy . . . . .	23
3.2	Ship data . . . . .	26
3.3	Glider data . . . . .	28
3.4	Auxiliary datasets . . . . .	29
3.5	Methodology . . . . .	42
<b>4</b>	<b>The ACT in boreal summer 2011</b>	<b>51</b>
4.1	Introduction . . . . .	51
4.2	Surface observations . . . . .	51
4.3	Vertical structure . . . . .	58
4.4	Mixing conditions . . . . .	67
4.5	Summary . . . . .	70
<b>5</b>	<b>Mixed layer heat and salinity budget during ACT onset in 2011</b>	<b>73</b>
5.1	Introduction . . . . .	73
5.2	Heat budgets during ACT onset . . . . .	75
5.3	Salinity budgets during ACT onset . . . . .	78
5.4	Residual . . . . .	82
5.5	Summary . . . . .	84
<b>6</b>	<b>Seasonal cycles in the central and eastern equatorial Atlantic</b>	<b>89</b>
6.1	Introduction . . . . .	89
6.2	Seasonal ML heat budgets . . . . .	90
6.3	Seasonal ML salinity budgets . . . . .	92
6.4	Summary . . . . .	103
<b>7</b>	<b>Synthesis</b>	<b>105</b>

Bibliography	I
List of Figures	XIII
List of Tables	XV
Danksagung	XVII
Erklärung	XIX

The following manuscript has been submitted as part of this thesis

**M. Schlundt**, P. Brandt, M. Dengler, R. Hummels, T. Fischer, K. Bumke, G. Krahmann, and J. Karstensen: Mixed layer heat and salinity budget during the onset of the 2011 Atlantic cold tongue. *submitted to Journal of Geophysical Research: Oceans*.

Author Contribution: Michael Schlundt collected the data during two research cruises, conducted data processing and analysis and wrote the manuscript. The co-authors contributed to the manuscript with designing the experiment at sea, data calibration, discussion of the results, and comments and reviews on the manuscript.





# 1 Introduction

The exchange of freshwater between the ocean and the atmosphere is one part of the global hydrological cycle and in terms of exchanged volume the most important (Fig. 1.1). Climate models predict an increased hydrological cycle in future projections (e.g. *Allen and Ingram* [2002]). This means in fact that salty regions of the ocean become saltier and fresh regions fresher. Such oceanic changes are also detected from hydrographic observations (e.g. *Durack and Wijffels* [2010]). The water that evaporates from the ocean to the atmosphere is taken from the ocean surface and the amount of freshwater in a defined volume of sea-water is determined through the salinity. Therefore, the sea surface salinity (SSS) and the near-surface salinity are key parameters for understanding the hydrological cycle and can also be used for reducing the uncertainties in surface freshwater flux estimates in the framework of the ocean rain gauge concept [e.g. *Font et al.*, 2003; *Yu*, 2011].

Almost all physical (related to oceanography) and several biogeochemical processes on the earth obtain their energy from the sun. Since the energy gain for the surface is dependent of the insolation angle, regions where the sun elevation is highest get the largest amount of energy. These regions are the tropical regions and in particular the equatorial regions. Here the sun is twice a year in zenith position. While most of the UV radiation is absorbed in the stratosphere, mostly visible radiation impacts the land and ocean surface. Equatorial oceanic regions constitute a significant part of global oceanic surface. Through the overall positive net surface heat flux in the equatorial regions, a large amount of heat is available for the ocean interior. This heat (together with other parameters like e.g. salinity) is transported in the ocean through several different processes, which lead to spatial and temporal variability of ocean temperatures and salinities on diurnal, intraseasonal, seasonal, interannual and longer time scales and to length scales from a few millimeters to several thousand kilometers.

The global overturning of properties like heat, salt and others happens within the Meri-

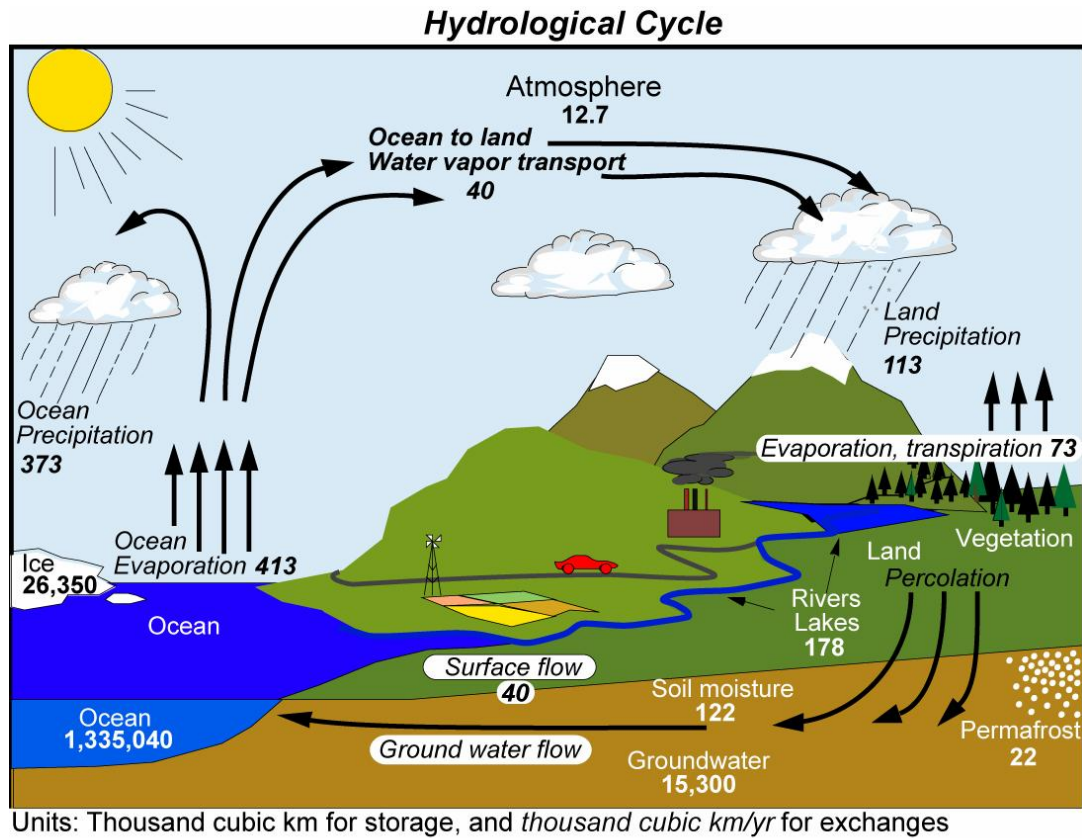


**Fig. 1.1:** The global hydrological cycle. Taken from Trenberth et al. [2007].

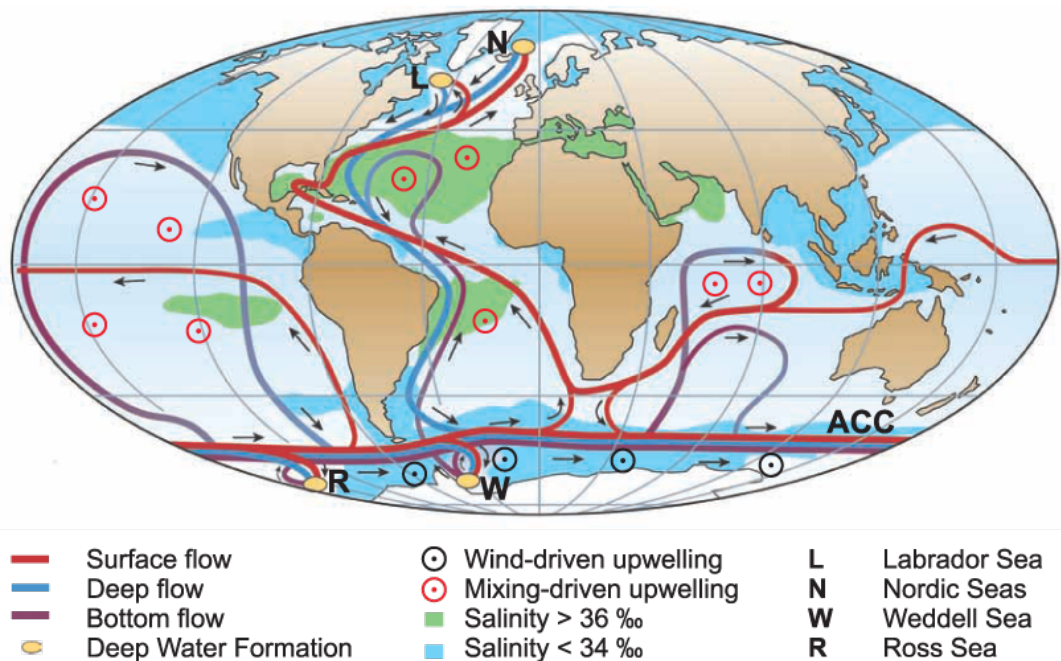


**Fig. 1.2:** The meridional overturning circulation. Taken from Kuhlbrodt et al. [2007].

dional Overturning Circulation (MOC). The MOC combines deep water formations in the North Atlantic and around the Antarctic continent, the flow of these water masses through the oceans basins as well as the upwelling of them in several oceanic regions (Fig. 1.2). In particular, the Atlantic part of the MOC (AMOC) is of special interest, because in this ocean basin the largest volume of ocean water is determined, the North Atlantic Deep Water (NADW). Additionally, the Atlantic is an unique ocean basin, because an overall northward heat transport is observed. The upwelling of deep water can be driven by the wind (*Toggweiler and Samuels* [1998] and references therein). This wind-driven upwelling happens around the Antarctic continent, where an Ekman-divergence caused by the strong westerlies yields upwelling of deep water masses. A second upwelling process is mixing, happening in tropical and subtropical regions. *Sandström* [1908] hypothesized that surface heat cannot drive the overturning alone. Hence, a deep heat source is necessary, which he (and others) connected to diapycnal mixing. This downward mixing of heat lightens the water masses, which then rise in lower latitudes. The mixing itself is caused by internal wave dissipation in the ocean interior [*Munk and Wunsch*, 1998]. Both mechanisms, wind-driven upwelling and mixing, are candidates for driving the AMOC [*Kuhlbrodt et al.*, 2007]. The surface fluxes of heat and freshwater, although not sustaining the MOC, play an essential role for the stability of the MOC, e.g. for the location of deep convection. These exchange of heat and freshwater between the ocean and the atmosphere happens at the surface and the upper layer of the ocean, usually known as mixed layer (ML).

The ML of the ocean is the region where a direct air-sea interaction results in changes on short time scales. Energy through the heat fluxes, momentum through the wind and freshwater through precipitation can be transported from the atmosphere into the ocean. Energy and freshwater can also be transported in the opposite direction. The input of momentum through the wind yields the mixing of physical properties like the temperature, the salinity and the density down to a certain depth and a uniform, well mixed layer results. In addition several biogeochemical properties interact between the ML and the atmosphere (Fig. 1.3). Besides atmospheric forcing and lateral advection through the currents, the ML is also influenced by vertical entrainment and diffusion through the ML base. However, the exact contribution from each term of the ML heat budget to sea surface temperature (SST) and ML temperature (MLT) variability as well as of the ML salinity (MLS) budget to SSS and MLS variability, respectively, is still under debate. Understanding the quantities and dynamics in the ML and the interaction between them is a main issue for researchers in the larger contexts of climate change, hydrological cycle

and also the large-scale overturning of ocean properties within the global MOC.

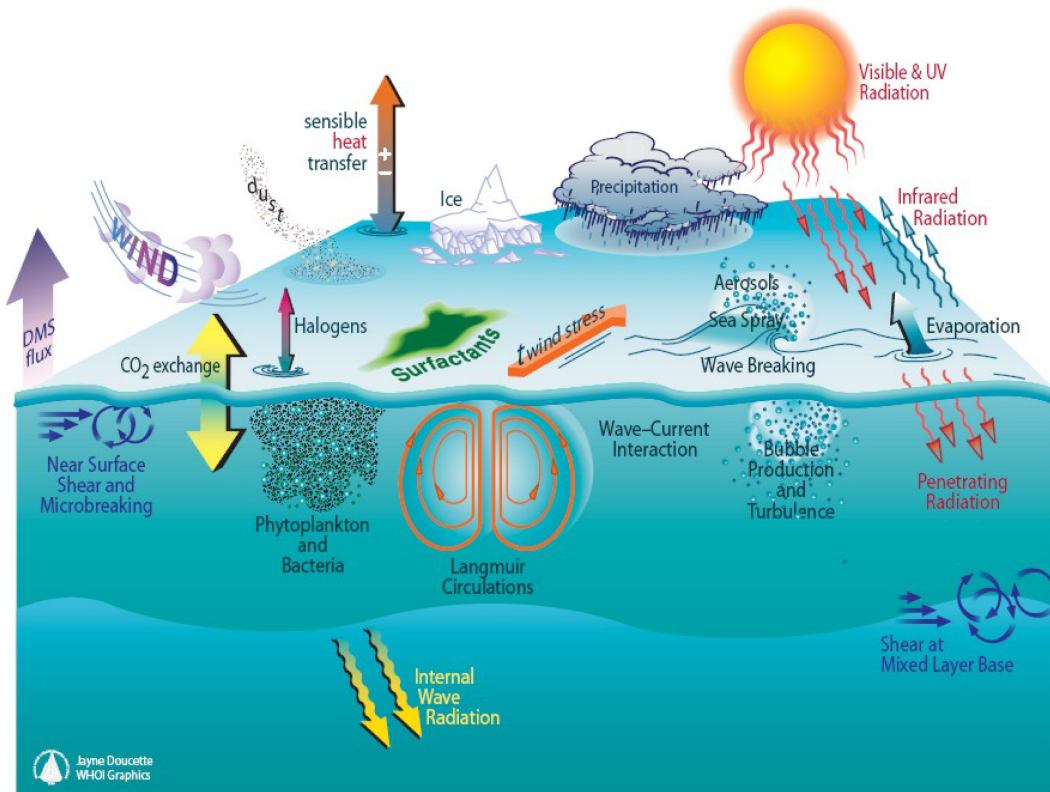


**Fig. 1.3:** Physical and biogeochemical interactions between the Mixed layer and the atmosphere.  
© Jayne Doucette, WHOI.

In this thesis an extensive in-situ dataset is used to investigate the ML heat and salinity budgets concurrently. Hydrographic, together with microstructure observations, and atmospheric data collected during two expeditions on R/V Maria S. Merian in spring/summer 2011 have been combined with simultaneous high-resolution temperature and salinity data from a glider swarm experiment. During this glider swarm experiment six gliders measured hydrographic properties between 2°S and 2°N (one glider track was extended to 4°S) and between 23°W and 10°W. In the following I refer to the observational experiment as the “Cold Tongue Experiment” (CTE). The CTE data set is further augmented by temperature and salinity profiles from Argo floats and time series from PIRATA (Prediction and Research Moored Array in the Tropical Atlantic; *Bourlès et al.* [2008]) buoys and subsurface moorings. The combined extensive in-situ data set is the basis to quantify all terms contributing to the ML heat and salinity budgets during the observational period.

In contrast to former studies about the tropical Atlantic, that concentrated on single mooring locations or empirically defined boxes and examined seasonal ML heat budgets [Foltz *et al.*, 2003; Hummels *et al.*, 2013; Jouanno *et al.*, 2011b; Peter *et al.*, 2006; Wade *et al.*, 2011], seasonal ML salinity budgets [Da-Allada *et al.*, 2013], seasonal SST variability [Carton and Zhou, 1997] or seasonal SSS variability [Bingham *et al.*, 2012; Dessier and Donguy, 1994], this study estimates all terms contributing to the heat and salinity budgets as an average for the entire region associated with the Atlantic cold tongue (ACT) (Fig. 3.1). This enables us to identify the processes responsible for the SST and SSS variability typically observed for this entire region. Due to the amount of ship time required to obtain such an extensive in-situ data set, the CTE covers only two months of the year 2011. The CTE was scheduled between May and July to focus on the processes responsible for the variability of SST and SSS during the development phase of the ACT.

## Thesis outline

This thesis is structured as follows. In chapter 2 the tropical Atlantic is described. All relevant properties are introduced and the mean state of them is marked. The data and the detailed methods are presented in chapter 3. The definition of the boxes is introduced, the several datasets are described and the cross-validation between them is shown. The methods of estimating the mixed layer budgets is described as well. The cold tongue evolution in the year 2011 is shown in chapter 4. Also the data are shown here, which are later used for the budget calculations. The derivation and combination of the relevant contributions to the mixed layer heat and salinity budgets in 2011 are shown in chapter 5. The results of the CTE in 2011 are compared to mean seasonal cycles in chapter 6 and a synthesis is given in chapter 7.



## 2 Tropical Atlantic

The tropical Atlantic is characterized by a complex interaction of different physical mechanisms. In this region the input of solar radiation has a maximum, representing a large source of energy for the ocean and the atmosphere. This input of energy has a clear seasonal cycle, which can be detected in several other parameters too. Most famous is the seasonal migration of the convergence region of the north- and southeasterly trades, the Intertropical Convergence Zone (ITCZ). In the Atlantic the ITCZ is mostly north of the equator [*Philander et al.*, 1996] and this region is defined by strong precipitation, large and high cloud development and a weakening of the trades. These trades interact with the surface and the upper layers of the ocean by Ekman dynamics influencing the evaporation [*Kraus*, 1959] and also resulting in strong zonal currents in the equatorial region, which was shown first by *Sverdrup* [1947]. The strength of these currents is in relation to the strength of the winds [*Philander*, 1990] and the meridional position of the currents is highly correlated with the migration of the ITCZ [*Stramma and Schott*, 1999]. One consequence of the equatorial current structure is elevated vertical shear of horizontal velocity due to these opposing currents leading to elevated mixing in the upper thermocline (e.g. *Hummels et al.* [2013]). Additional variability in the current field is caused by the passage of Tropical Instability Waves (TIWs), propagating westward at and near the equator [*Düing et al.*, 1975; *Legeckis*, 1977]. These waves are generated via barotropic and baroclinic instabilities of the zonal current system [*Philander*, 1978; *von Schuckmann et al.*, 2008].

A particular phenomenon in the Eastern Equatorial Atlantic (EEA) is the annual development of a region of cold SSTs. This so called ACT forms in boreal spring/summer, when the south easterly trades intensify [*Philander and Pacanowski*, 1981], and retracts toward the end of the year resulting in uniformly warm SSTs within the tropical Atlantic. Minimum temperatures of about 22°C are reached within the “center” of the ACT at approximately 10°W [*Jouanno et al.*, 2011b]. This is a reduction of about 6°C compared to the temperatures before the onset of the ACT. The seasonal cycle of SSTs is most

pronounced at this location. Towards the western and southern edges of the ACT the seasonal cycle of SST is clearly evident, but temperatures do not reach the minimum values as found at 10°W at the equator. The interannual variability of the SSTs within the ACT strongly correlates with the interannual variability of the onset of the West African Monsoon (WAM) (*Brandt et al.* [2011]; *Caniaux et al.* [2011]). In general the ACT variability is correlated with the rainfall variability in tropical regions [e.g., *Xie and Carton*, 2004] and the aforementioned currents are related to ACT variability as well [*Hormann and Brandt*, 2007].

In the following subsections an overview over the different quantities is given, which are important and interacting with each other.

## 2.1 Temperature

The temperature in the tropical Atlantic is dominated by the input of energy from solar radiation, which is highest at the location, where the sun is in the zenith. This is only possible between the tropics of Cancer and Capricorn and yields to maximum SSTs in the tropics as seen e.g. in the World Ocean Atlas 2009 Climatology, henceforth WOA2009 [*Antonov et al.*, 2010; *Locarnini et al.*, 2010] (Fig. 2.1). The rotation of the earth around the sun within one year leads at the equator at the top of the atmosphere to a semiannual cycle of shortwave heat input, but at the ocean surface an annual harmonic is more striking [*da Silva et al.*, 1994]. The tropical SST and temperatures within the mixed layer are dominated by this seasonal cycle, while the amplitude of this cycle is weaker in the western parts of the tropical Atlantic [*Reynolds and Smith*, 1994].

A monthly climatology of SST gives a first impression on the intraseasonal variability. Monthly averages of 15 years (1998-2012) of satellite data from the TRMM Microwave Imager (TMI)<sup>1</sup> onboard the Tropical Rainfall Measurement Mission (TRMM) satellite are shown in Fig. 2.2. Main features, similar to the annual average (cf. Fig. 2.1), in the tropics are the maximum temperatures north of the equator around 5°N in the first half of the year in the eastern basin and around 8°N during the second half of the year in the western basin, decreasing north- and southward from these latitudes. The most striking

<sup>1</sup>TMI data are produced by Remote Sensing Systems and sponsored by the NASA Earth Science MEAsURES DISCOVER Project. TMI data are available at [www.remss.com](http://www.remss.com)



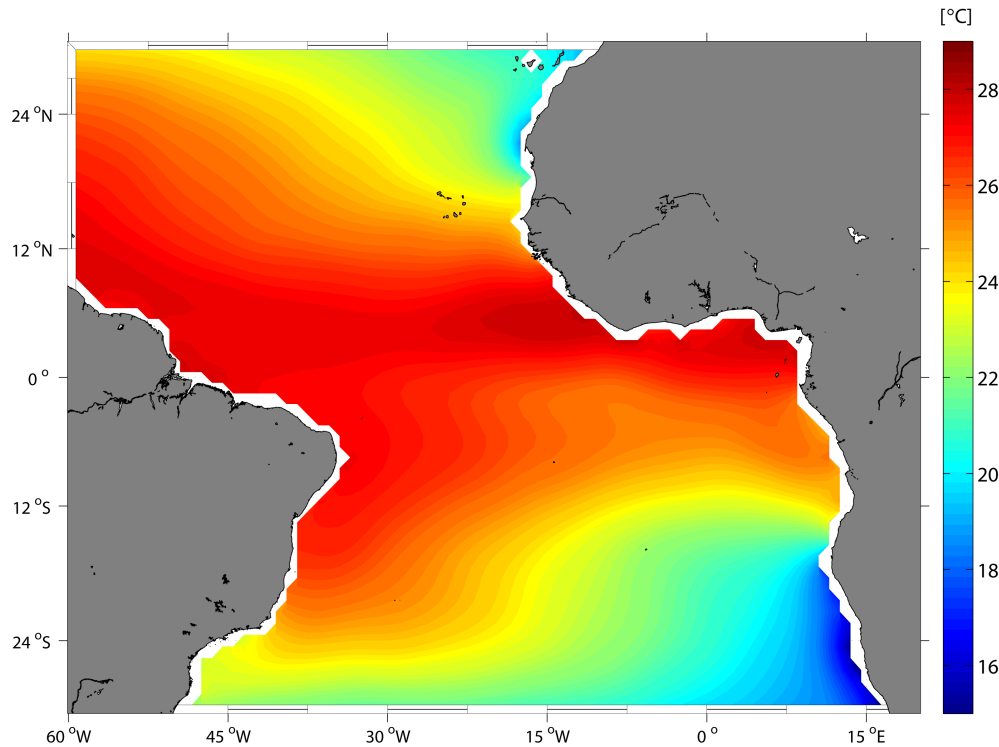


**Fig. 2.1:** Annual mean sea surface temperature from WOA2009.

phenomenon is the cold tongue in the EEA. The onset is mostly in May at the equator and afterwards the cooling develops west-, east and southward during June and July. From August ongoing the cold tongue is connected with cold waters in the eastern basin of the southern hemisphere.

To shortly overview the vertical annual mean temperature distribution (Fig 2.3), again the equatorial maximum is visible. Also the strong vertical gradients below the mixed layer at the equator in the relative shallow thermocline are a striking phenomenon. This thermocline divides the warm water in the upper layer (first tens of meters) and the colder water masses below. Remarkable is an elevation of the thermoclines at around 50 m depth at 1-2°S. This anomaly from the general structure of the thermocline is associated with the Equatorial Undercurrent (EUC). The EUC is a subsurface source of cold water for the entire EEA and will be further described later in this chapter.

Several studies have examined the processes leading to SST and MLT changes in the tropical and equatorial Atlantic. For the western ACT region, *Foltz et al.* [2003] showed the

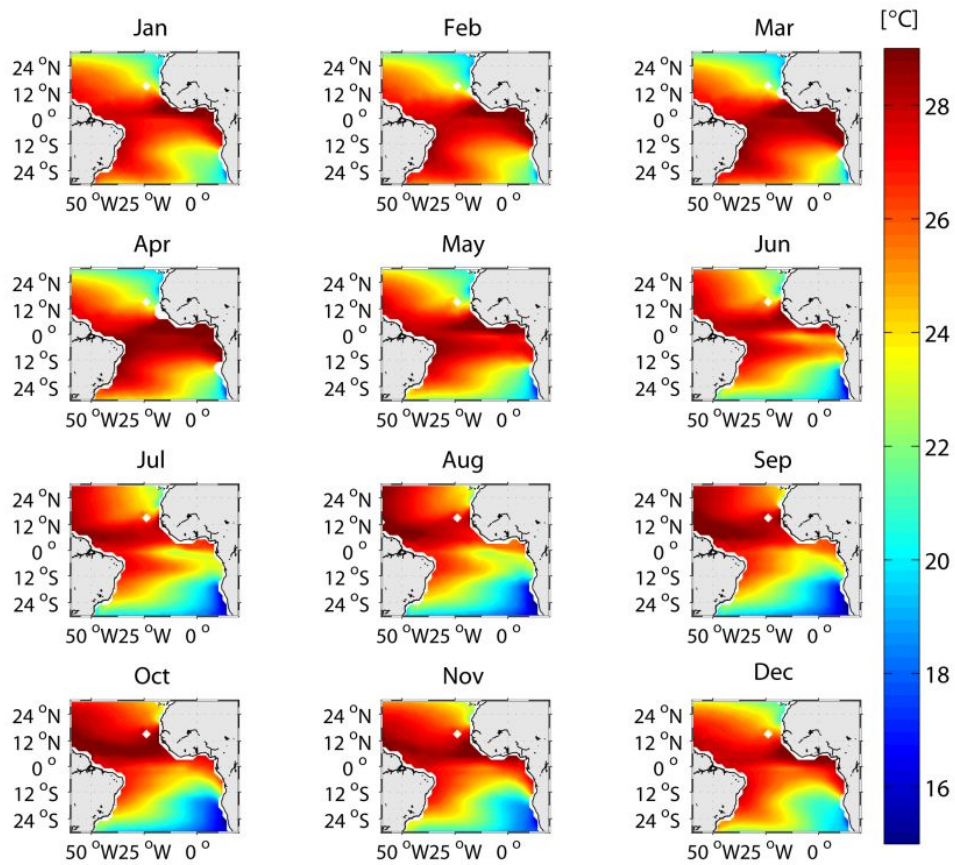


**Fig. 2.2:** Monthly mean sea surface temperature climatology from TMI.

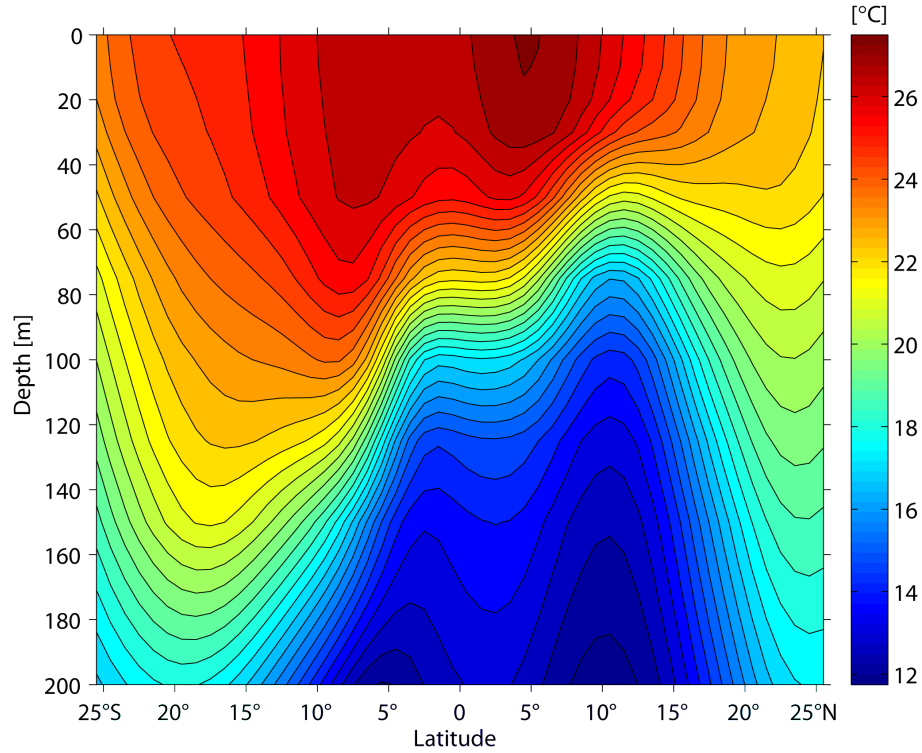


**Fig. 2.3:** Annual mean temperature from WOA2009 averaged between 28.5°W and 22.5°W. Contour interval 0.5 K.

importance of lateral advection by evaluating different terms of the ML heat budget at PI-RATA buoy locations. However, the authors were not able to close the ML heat budget for the equatorial sites at 23°W and 10°W, similar to the majority of other studies conducted within the ACT region [Wade *et al.*, 2011]. They speculated that unaccounted diapycnal mixing at the base of the ML may contribute to their unexplained residual. This contribution was recently estimated by Hummels *et al.* [2013]. Using an extensive set of microstructure observations, they showed that indeed the diapycnal heat flux through the ML base is a dominant cooling term during ACT development on the equator at 10°W. This is also in general agreement to global ocean circulation models as was recently reported by Jouanno *et al.* [2011b]. In a recent work Hummels *et al.* [2014] additionally showed the contributions to the ML heat budget on other buoy locations in the cold tongue region. They described the seasonal cycles and the importance of the several terms in the western (0°N, 23°W), central (0°N, 10°W), eastern (0°N, 0°E) and southern (10°S, 10°W) ACT

## 2.2 Salinity

Fig. 2.4 shows the salinity maxima in the subtropics, the strong freshwater sources of rivers and the relative salinity minimum at the lower latitudes in the annual mean SSS from WOA2009. This minimum is detected in a zonal band around  $5^{\circ}$ - $6^{\circ}$  N, which was shown e.g. by *Schmitt et al.* [1989] as the annual mean latitude of the ITCZ and the corresponding precipitation exceeds evaporation. In the Atlantic the mean ITCZ-latitude is not equal to the equator, but slightly shifted northward. Comparing the distance of the locations of the subtropical maxima from the equator, it is obvious that the North Atlantic salinity maximum is further away (around  $25^{\circ}$ N) than the Southern Atlantic maximum (around  $17^{\circ}$ S), indicating the same northward shift.

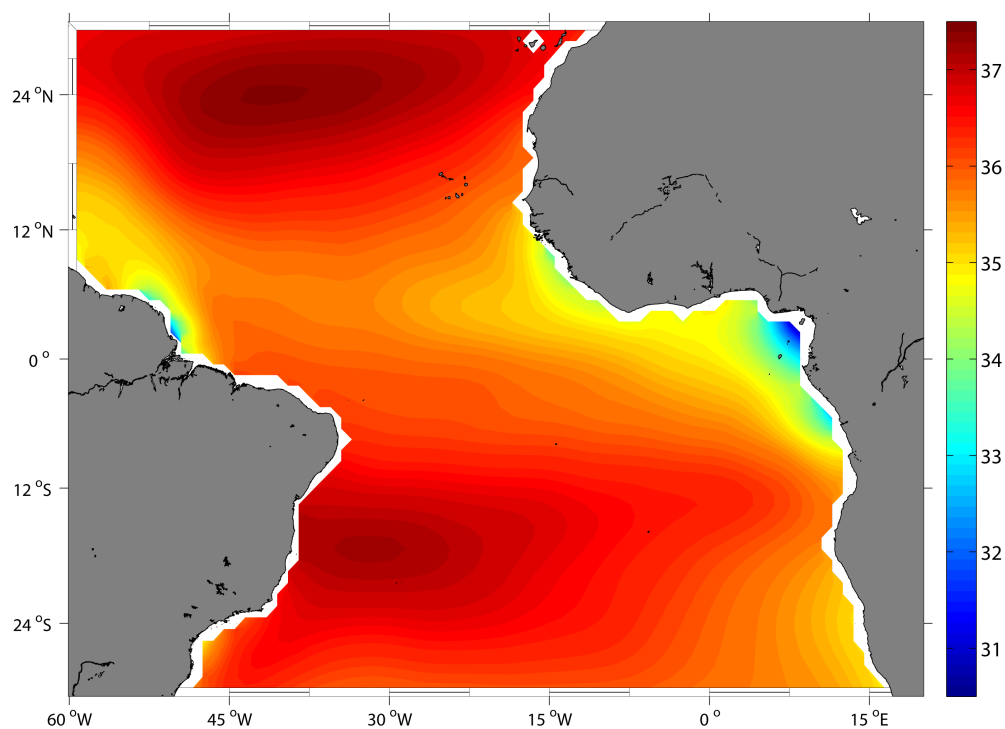


**Fig. 2.4:** Annual mean sea surface salinity from WOA2009.

A monthly climatology of SSS gives a first impression on the intraseasonal variability. Recently, ocean remote sensing has yielded a large increase in available SSS data, particularly important to study the SSS variability of open ocean regions, which were insufficiently sampled in the past by research vessels or Argo floats. Currently, two satellite missions monitoring SSS are operating in parallel, namely the Soil Moisture Ocean Salinity

(SMOS) mission of the European Space Agency (ESA) [Berger *et al.*, 2002; Font *et al.*, 2013] which started in November 2009 and the joint U.S./Argentinean Aquarius/Satélite de Aplicaciones Científicas (SAC)-D mission [Lagerloef *et al.*, 2008] which started in June 2011. The high resolution SSS data provide new insights into oceanic freshwater cycles as well as surface ocean dynamics [e.g. Alory *et al.*, 2012; Lee *et al.*, 2012; Tzortzi *et al.*, 2013] and can be used to improve estimates of the ML salinity budget. Monthly averages of three years of satellite data from SMOS<sup>2</sup> are shown in Fig. 2.5. Main features, similar to the annual average (cf. Fig. 2.4), in the tropics are the freshwater patches along the coasts, resulting from the river run-off into the Atlantic Ocean, and the band of relative low salinities, associated with the ITCZ.

In January the EEA together with the Gulf of Guinea and the central equatorial Atlantic north of the equator are the freshest regions neglecting the river run-offs. Along the equator, a westward SSS gradient is present, which vanishes during summer, when the EEA becomes saltier. In particular, in the cold tongue region the salinity increases remarkably. Later in fall and early winter the whole region along and south of the equator remains salty.

The second striking seasonality is visible along the ITCZ. A pattern, which might belong to ITCZ is first observed during April/May, when a zonal band across the entire Atlantic along  $\sim 5^\circ\text{N}$  with relative low salinities is observed. This band migrates northward and connects later to a second low salinity pattern. This second pattern is related to the freshwater advection with the North Equatorial Countercurrent (NECC). The NECC is gained by freshwater from the North Brazil Current (NBC) [Schott *et al.*, 2004], which is entrained through the large outflow from the Amazonas river. The zonal structure north of the equator vanishes later in the late fall/early winter, when the ITCZ has moved southward again.

Looking at the vertical distribution of the salinity (Fig. 2.6) in the annual mean again the northward shift of the ITCZ is visible with the local salinity minimum around  $5^\circ\text{N}$ . The subtropical maxima in the regions where the evaporation largely exceeds the precipitation are around  $17^\circ\text{S}$  and around  $25^\circ\text{N}$ , so the asymmetric northward shift is clearly recog-

---

<sup>2</sup>All SMOS SSS data used in this thesis were produced by the Barcelona Expert Centre ([www.smos-bec.icm.csic.es](http://www.smos-bec.icm.csic.es)), a joint initiative of the Spanish Research Council (CSIC) and the Technical University of Catalonia (UPC), mainly founded by the Spanish National Program on Space.

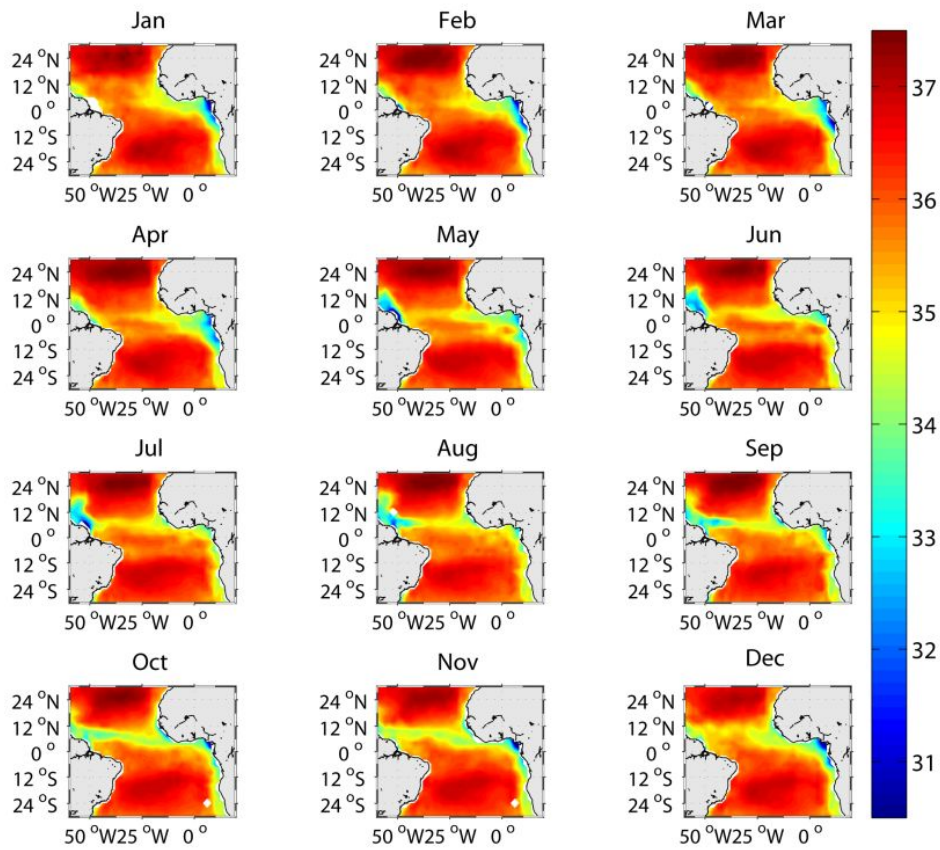


**Fig. 2.5:** Monthly mean sea surface salinity climatology from SMOS.

nizable. A local maximum in a range about 40-70 m depth at the equator is associated with relative high salinities advected eastward with the EUC, which is fed partly by salty subducted water from the southern subtropics within the so-called Subtropical Cell (see sect. 2.4). Lateral gradients are relative small in this depth, but increasing to higher latitudes while the vertical salinity gradients are enhanced in the pycnocline above the EUC pathway. A distinct feature of the upper equatorial thermocline is a pronounced seasonal cycle of salinity in the central and eastern tropical Atlantic [Kolodziejczyk *et al.*, 2014]. During early boreal summer, saline water masses are transported eastward in the upper thermocline to the African coast within the EUC and recirculate westward on both sides of the EUC, while on mid-boreal summer, the EUC weakens in the upper thermocline and the equatorial salinity maximum disappears [Gouriou and Reverdin, 1992; Hisard and Morlière, 1973; Johns *et al.*, 2014; Kolodziejczyk *et al.*, 2014].

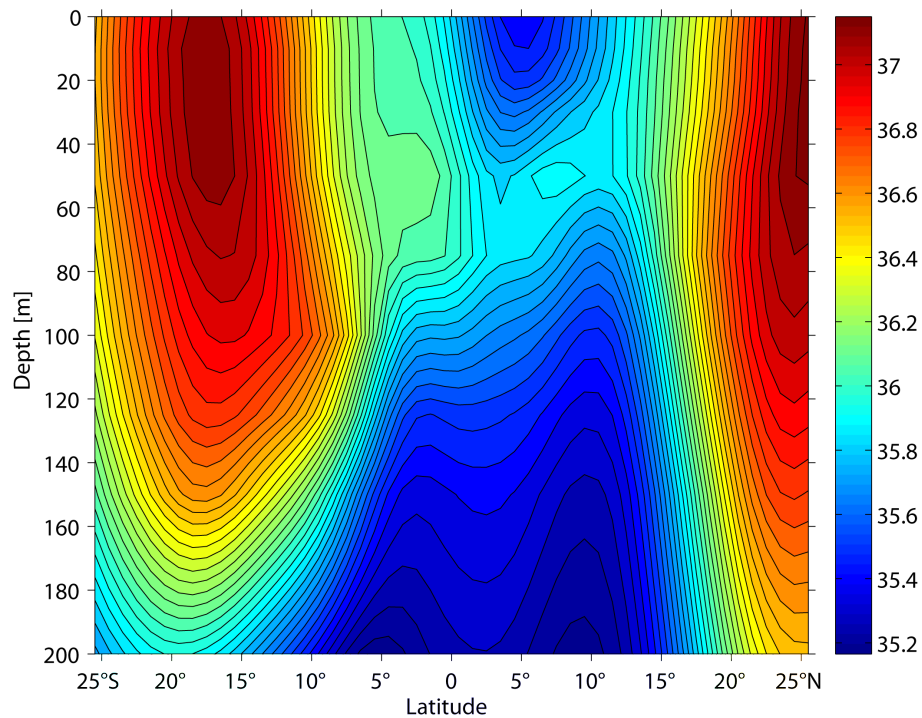


**Fig. 2.6:** Annual mean salinity from WOA2009 averaged between 28.5°W and 22.5°W. Contour interval 0.05 psu.

However, the SSS and also the salinity in deeper layers is variable on different timescales. Curry *et al.* [2003] described a large observed increase over decades at low latitudes. In analogy to the ML heat content variability, the MLS variability is driven by lateral salt (or freshwater) advection, vertical entrainment at the ML base, surface freshwater flux (here



defined as difference of evaporation and precipitation:  $E-P$ ), and salt diffusion. In fact, *Kolodziejczyk et al.* [2014] as well as *Johns et al.* [2014] recently suggested that intense mixing of the high-saline upper thermocline waters with surface waters in the eastern Gulf of Guinea (GG) is responsible for the erosion of the upper thermocline salinity maximum during late spring and summer. In general, the major difference in the evolution of heat and freshwater anomalies in the ML is the lack of a direct feedback between ocean and atmosphere for freshwater anomalies. Comparing the impact on density changes the freshwater anomalies might be smaller in magnitude than heat anomalies, but their persistence can be longer [*Hall and Manabe*, 1997].

Analyses of the ML salinity budget in the western tropical North Atlantic indicated that horizontal advection dominantly contributes to the seasonal cycle in MLS [*Foltz et al.*, 2004; *Foltz and McPhaden*, 2008]. In the central and eastern tropical North Atlantic seasonal variability is dominated by the seasonal cycle in precipitation [*Dessier and Donguy*, 1994; *Foltz and McPhaden*, 2008]. Similar results were found by *Da-Allada et al.* [2013] using a combination of in-situ, satellite, and reanalysis data to constrain a simplified ML model. They showed that horizontal advection, entrainment, and precipitation dominantly contribute to the MLS variability in the eastern tropical Atlantic (ETA), in the GG, and in the Congo region (CO). In their study, the contribution of diapycnal mixing on the upper ocean salinity budget was not considered due to a lack of observational data.

## 2.3 Atmospheric parameters

The atmosphere is permanently in interaction with the ocean. The energy gain of the ocean through the solar radiation and downwelling longwave radiation and the energy loss through outgoing longwave radiation can be merged to the net surface heat flux. Integrated in this net surface heat flux are also the turbulent heat fluxes, namely the latent and the sensible heat flux. One would expect that the mean seasonal cycle at the equator follows in the interior basin, here throughout the year the largest energy gain for the ocean is observed, a semiannual cycle dominated by the semiannual cycle of solar radiation due to the zenith angle of the sun. This is valid with peaks during February/March and from July until the end of the year. However, the peaks are not equal, but the net surface heat flux into the ocean is larger in fall. This is caused by the seasonal cycle of the latent heat flux with a reduction in late boreal summer and fall [*Marin et al.*, 2009]. At the coastal



regions in the west (Amazon outflow) and in the east (GG) different contributions to the net surface heat flux, e.g. an increased latent heat flux, reduce the total gain for the ocean significantly. However, the net surface heat flux is positive for the ocean throughout the year for the entire equatorial region in the Atlantic. This is fundamental for the earth's energy budget. In the atmosphere, the heat is transported poleward directly within the Hadley Cell and over stationary and transient eddies in the midlatitudes. The larger part of the heat excess in the tropics is transported in the ocean interior with the MOC.

Precipitation in the equatorial Atlantic follows an annual cycle with different magnitude at the equator. During the first half of the year, in particular in spring, the equator is influenced by precipitation. The amount of precipitation reduces from the west to the east. During summer the precipitation mostly completely vanishes at the equator due to the northward migration of the ITCZ. Only in the western equatorial Atlantic precipitation is observed but much weaker than during boreal spring. Generally, the tropical precipitation is connected to ITCZ, as the upward component of the Hadley Cell. Therefore, the precipitation (which is only rainfall in these latitudes) is of convective nature.

The wind interacts with the ocean surface through its friction, determining the evaporation and the turbulent heat fluxes. The momentum, which is transferred into the ocean mixes the upper meters of the water column and yields the ML. The wind at the equator in the Atlantic is weak in boreal winter and the early spring. During April and May an increase is observed in the mean seasonal cycle, related to the northward shift of the ITCZ and the ACT onset. Striking is a second minimum from June to August around 10°W. As described before, this region is the center of the cold tongue with the coldest temperatures during this time. The decrease in wind-speed may be explained with the coincidence between SST and surface winds through the stabilization of the atmospheric boundary layer above the cold water as hypothesized by *Wallace et al.* [1989]. This coupling is observed in the Pacific [*Chelton et al.*, 2001] and in the Atlantic Ocean [*Coëtlogon et al.*, 2010]. Later in the year in fall the wind at the equator in the eastern basin has its annual maximum which is related to a second cooling of the EEA [*Okumura and Xie*, 2006]. Generally the wind is stronger in the western basin compared to the eastern equatorial Atlantic.

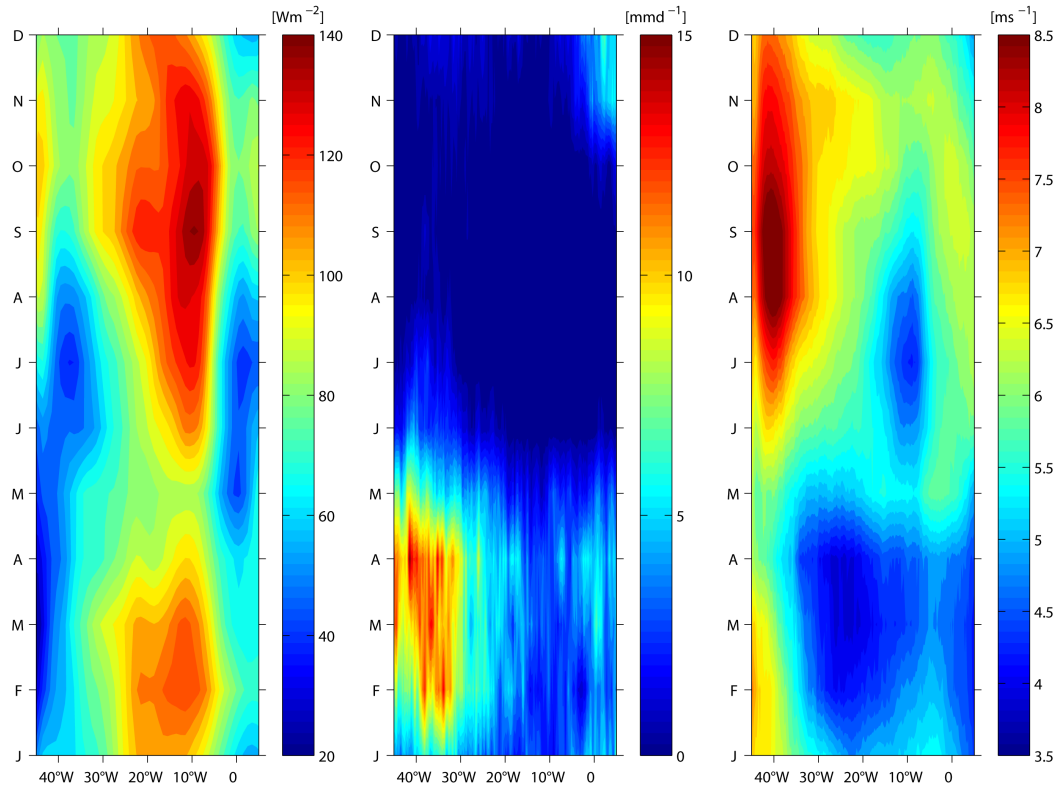


**Fig. 2.7:** Hovmoeller plot of mean seasonal cycle of monthly net surface heat flux (from TropFlux), precipitation (from TMI) and wind speed (from TMI) at the equator. Used are data from the years 1998 until 2012.

## 2.4 Currents

The current system in the tropical Atlantic is dominated by zonal surface and subsurface currents. A direct interaction of the winds with the ocean surface leads to friction, within momentum is transported into and forces the ocean. When away from the equator, the Coriolis force acts on the moving water (to the right (left) on the northern (southern) hemisphere). This leads to a spiral-like layer in the upper tens of meters of the oceans, where frictional force and Coriolis force balance each other. This layer is called Ekman<sup>3</sup>-layer and the depth, where the influence of the wind vanishes is called Ekman depth. When integrating from the surface to the Ekman-depth the transport, orthogonal to the wind stress direction, can be estimated. The most prominent results of Ekman forcing are the subtropical gyres, where the mid-latitude westerlies and the easterly trades lead to a convergence of water masses (elevation of the sea surface) and finally to Ekman-pumping (defined as the divergence of the Ekman-transport or as the curl of the wind stress) of these converged water masses. Another example is the equatorial Ekman-divergence which yields upwelling at the equator.

As a consequence of the Ekman-pumping in the subtropical gyres the density surfaces are displaced resulting in horizontal density gradients. The pressure forces related to this drive the water to reduce these gradients. Again, the Coriolis force acts on this moving water leading in the end to a balance between pressure gradient force and Coriolis force. A circulation, orthogonal to the pressure gradient force, is the result which is called geostrophic circulation. The vertical integral of the geostrophic circulation is the geostrophic transport. When assuming no friction at the bottom and considering the change of the Coriolis parameter with latitude ( $\beta$ -plane), a meridional geostrophic circulation has to balance the Ekman-pumping (both hold e.g. for the subtropical gyres) to not pump into the bottom. These conditions are the Sverdrup<sup>4</sup> regime and the relation between the total meridional transport (the Sverdrup transport) and the Ekman pumping is defined in the Sverdrup relation. While in the subtropical gyre the Sverdrup transport is equatorward (vertical component of wind stress curl is negative) it has to be compensated somewhere. This happens in a western boundary current, like the Gulf Stream in the Atlantic and the Kuroshio in the Pacific. Here bottom friction is included and the western intensification of the gyre circulation was described by and is named after Stommel<sup>5</sup>. All

<sup>3</sup>Vagn Walfrid Ekman, 1874-1954, swedish oceanographer

<sup>4</sup>Harald Ulrik Sverdrup, 1888-1957, norwegian oceanographer and meteorologist

<sup>5</sup>Henry Melson Stommel, 1920-1992, US-american oceanographer

aforementioned concepts describe the so-called wind-driven circulation from where the ocean currents in the top hundreds of meters are the consequence.

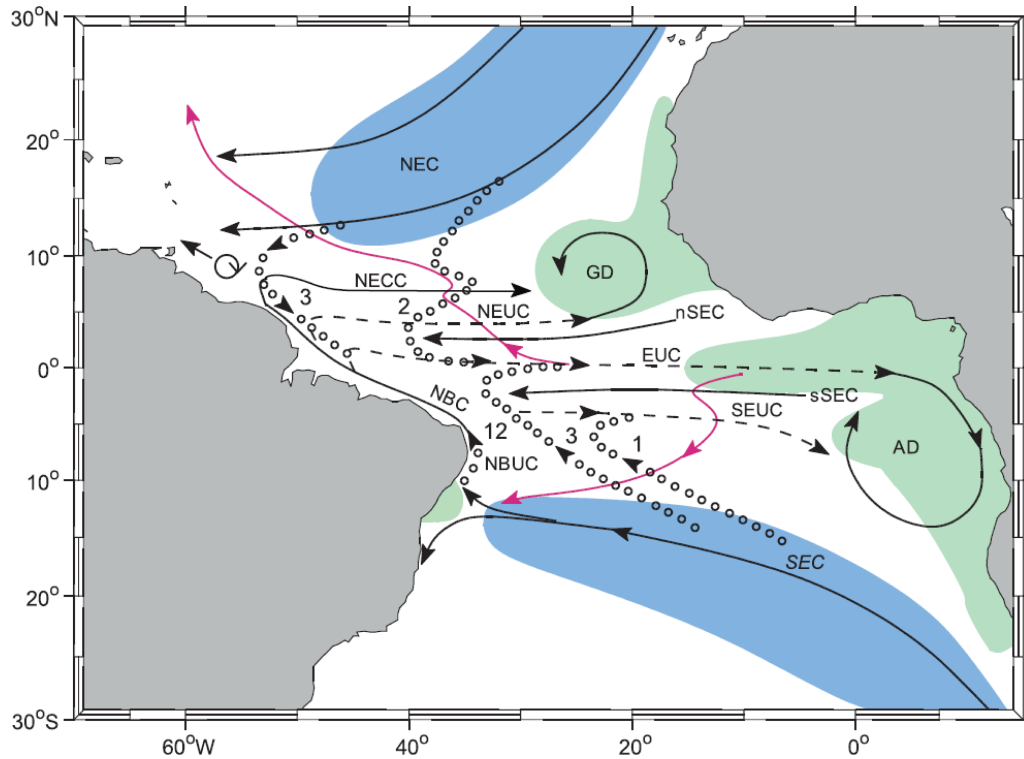


**Fig. 2.8:** Schematic representation of the circulation in the STC in the Atlantic with downwelling (blue) and upwelling (green). Solid lines are surface currents and dashed lines are subsurface currents. From Schott *et al.* [2004].

In Fig. 2.8 the surface and upper subsurface currents are illustrated together with the regions of up- and downwelling and the pathways of subducted water in the subtropics. High saline and warm water is subducted in the subtropics on both hemispheres. The subduction, defined as a mass flux across the ML base [Karstensen and Quadfasel, 2002], has a vertical (Ekman-pumping) and a lateral (advection) component. The subducted water is geostrophically transported equatorward and westward with the North Equatorial Current (NEC) on the northern hemisphere [Qiu and Huang, 1995] and the southern branch of the South Equatorial Current (SEC) on the southern hemisphere [Karstensen and Quadfasel, 2002]. Both latter studies also showed that the main parts of the subducted waters returns poleward on the several hemisphere with the western boundary currents, not entering the STC. However, in the western basin subsurface undercurrents are gained by parts of the subducted waters, mostly with southern hemisphere water over the North Brazil Undercurrent (NBUC). The NBUC becomes the NBC and feeds in the following the est-

ward undercurrents, namely the EUC and the Northequatorial Undercurrent (NEUC) as one MOC pathway (the other pathway of northward heat transport within the MOC is over ring shedding at the NBC retroflexion) [Schott *et al.*, 2004]. The Southequatorial Undercurrent (SEUC) is supplied by a mixture of NBUC and SEC waters. All these undercurrents bring a large amount of water into the eastern basin. Here, a remarkable part is transported to the surface by mixing or upwelling at the equator, in the Angola Dome or in the Guinea Dome. This water, now close to or at the surface, recirculates back poleward with the Ekman transport. McCreary and Lu [1994] described the circulation of subducted water from the subtropics to the equator, upwelling and recirculation away from the equator at the surface and defined this as the Subtropical Cell (STC). The STCs on the northern and on the southern hemisphere are different due to the influence of the MOC on the STCs. The MOC transports over the NBC warm and intermediate water from the South to the North Atlantic [Ganachaud and Wunsch, 2000]. This northward return flow of the MOC results in a stronger STC on the southern hemisphere [e.g. Zhang *et al.*, 2003].

The strongest subsurface current in the tropical Atlantic, in terms of mass transport and/or flow velocities, is the EUC. This current is in fact a balancing subsurface eastward flow of the westward elevation of the surface waters due to the zonal component of the trades. The resulting pressure gradient force is at the surface balanced by the zonal wind component. In deeper layers, where the wind influence vanishes, the eastward pressure gradient yields a downgradient flow, the EUC. Frictional forces slow down the EUC and the geostrophy keeps it centered at the equator. Fig. 2.9 shows, that the eastward EUC, SEUC, NEUC and the NECC with its northern branch (nNECC) are obviously the main zonal currents. In particular, the NECC is quite interesting, while flowing upwind most of the year. It is a nice example of Sverdrup theory and results from the northward shifted ITCZ and the windfield, which is not symmetric at the equator. An Ekman-convergence at the ITCZ latitudes yields a northward pressure gradient force. The resulting geostrophic current, the NECC, flows eastward. These currents, specified above, transport heat, salt, oxygen and other parameters eastward and are essential for the eastern Atlantic. Together with the westward northern and central branch of the South Equatorial Current (nSEC and cSEC, respectively) at the upper tens and hundreds meter of depth, they describe the general circulation in the tropical Atlantic.

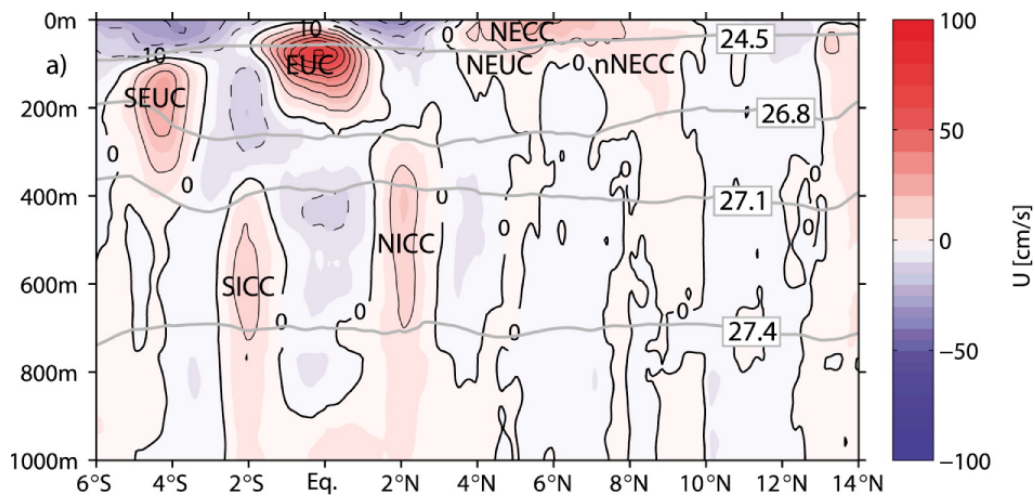


**Fig. 2.9:** Mean zonal velocity between  $28.5^{\circ}\text{W}$  and  $23^{\circ}\text{W}$  during 1999-2008. From Brandt *et al.* [2010].

## 3 Data and Methodology

To determine the various components of the ML heat and salinity budgets, observations of various parameters were required at adequate resolution. In particular this means data for all heat and freshwater flux components between atmosphere and ocean, microstructure observations for the oceanic mixing process, ocean velocities and the hydrography of the ML itself. The strategy pursued here, which is explained in more detail below, requires complementing the in-situ data base with further products, such as satellite observations, reanalysis products for ocean-atmosphere fluxes, surface and ML velocities and the output of a high-resolution assimilation model run. In this study, salinities are reported in practical salinity units (PSS-78).

### 3.1 Box averaging strategy

Time series of glider observations were used to study the variability of the upper ocean mixed layer. The high resolution of data in time (one profile in approximately 4 hours) as well as in space (one profile every 3-4 km) made it possible to examine the spatio-temporal variability. Neglecting daily cycles (see MLD definition) it appeared that the cold tongue region is characterized by relatively homogeneous water masses within the ML. To be able to determine the particular characteristics of the heat and freshwater budgets of the ACT region, we define a second area located to the north of the ACT between the northern ACT boundary and a fixed boundary at 8°N (Fig. 3.1).

Satellite and modeled SSTs were used to define the boxes. The zonal boundaries of the ACT box are 23°W and 10°W representing the western ACT region (Fig. 3.1). We used the meridional gradients of SST to determine the position of the thermal front. The front is often modulated by TIWs. The maximum gradient between 1°S and 4°N is used as the boundary between two boxes, one with strong cooling south of the SST front, repre-

senting the cold tongue region (ACT box) and one with weak cooling north of the SST front. The southern border of the southern box is likewise defined by the maximum meridional SST gradient between 5°S and 2°S. Due to the fact that cooling onset was reached within the onset of our experiment, we can identify a maximum meridional gradient of SST which is small in the beginning of the CTE. A wave-like structure, associated with TIW propagation is weak during May and in the beginning of June in the SST data. In addition, the undulations of the SST front increased in amplitude with the intensification of the cooling. The position of the SST front (maximum meridional SST gradient) defines the boundary between the southern and the northern box. Due to the different phases of TIW propagation the two boxes were defined from the model output with exactly the same approach as well. All individual contributors to the budget are calculated profile-wise or on a regular 1°x1°-grid, and are subsequently averaged in the two boxes.

The time period of 9-11 days that was used for averaging all data in the boxes follows from the decorrelation time scales for tropical oceans. Decorrelation time for zonal currents is suggested between 10-15 days and for the meridional currents between 3-10 days [e.g. *Hansen and Herman*, 1989; *Hansen and Paul*, 1984; *Swenson and Hansen*, 1999].

The profiles in both boxes were averaged by bootstrapping with 1000 realizations. The mean of all realizations was taken as the value for the box (for MLT, MLS, MLD, the temperature difference between MLT and the temperature below the ML base, the salinity difference of MLS and salinity below the ML base). The error was computed as two standard deviations explaining ~95% of the data. Uncertainties for dissipation rates of TKE were estimated by bootstrapping and the propagation of errors was calculated with the procedure of *Ferrari and Polzin* [2005] for diapycnal diffusivities and accordingly for the heat and salt fluxes [*Schafstall et al.*, 2010].

Box-averaged lateral gradients of MLT and MLS were calculated by using satellite SSTs and SSSs. These gridded products are available at 3-day-mean time resolution. Precipitation, evaporation, net shortwave and longwave radiation as well as turbulent heat fluxes (latent and sensible) through the ocean's surface were averaged over the clustered region. The uncertainty of the box-average was determined by taking the error, determined by the comparison with shipboard measurements, at every grid point into account. Errors for the velocities were estimated by comparing satellite derived velocities with in-situ measurements.



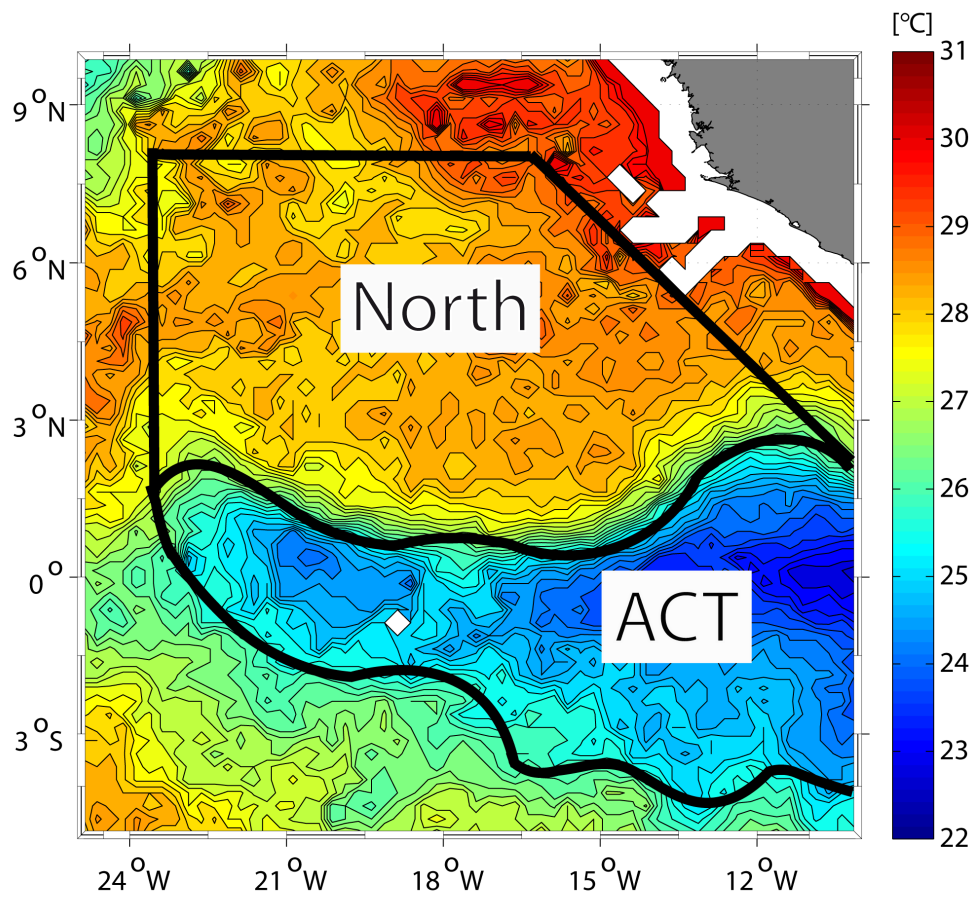


**Fig. 3.1:** Box edges (black lines) and SSTs from TMI (Background colors) between 14th and 17th of June 2011. “ACT” describes the area associated with the Atlantic cold tongue, while the northern box is denoted “North”.

## 3.2 Ship data

During the two research cruises, lasting from the 11th of May to the 11th of July, profiles of conductivity, temperature and depth (CTD) were acquired, as well as continuous observations of the upper ocean temperature and salinity with a thermosalinograph (TSG) (Fig. 3.2) and the currents with two (38kHz and 75 kHz) vessel mounted Acoustic Doppler Current Profilers (vmADCP) [Brandt *et al.*, 2012; Körtzinger, 2011]. CTD profiling was performed with a SeaBird 911 CTD rosette system and was calibrated against bottle salinity samples analyzed with a Guildline Autosol salinometer. The TSG data was recorded every minute using a SeaBird 38/45 system with an intake located at 6.5 m depth in the front of the ship. The TSG observations were calibrated against CTD data from 6-7 m depth and later considered as additional MLT and MLS observations for the box and time averaging and for the comparison with satellite observations. The current observations with the 75 kHz vmADCP were used to study the background velocity field, as seen in chapter 4.3. The velocity data were not used for further calculations.

Along with the CTD profiles microstructure observations were performed at almost all stations. The microstructure data was collected using an MSS-90D profiler manufactured by Sea&Sun Technology. It was equipped with two shear sensors, a fast temperature sensor, an acceleration sensor and a tilt sensor, plus a set of slower response standard CTD sensors. The data was sampled at a rate of 1024 Hz. A detailed description of the probe is given in Prandke and Stips [1998]. From the observed velocity-microstructure it is possible to derive the dissipation rate of turbulent kinetic energy (TKE), from which the diapycnal fluxes of heat and salt can be estimated. The dissipation rate is calculated under the assumption of isotropic turbulence from the shear wavenumber spectrum ( $E_{du'}/dz$ ). The spectrum is integrated between dynamically adapted wavenumber limits with  $\epsilon = 7.5\nu \int_{k_{min}}^{k_{max}} E_{du'}/dz(k) dk$  to estimate the dissipation rate  $\epsilon$  ( $\nu$  is the kinematic viscosity of seawater). Due to the limited resolved wavenumber band, a variance loss correction is applied according to the universal Nasmyth spectrum [Oakey, 1982]. The derivation of dissipation rates is described in detail in e.g., Schafstall *et al.* [2010] and Hummels *et al.* [2013].

Shipboard observations of atmospheric properties during CTE included measurements of the downward shortwave radiation flux with a pyranometer and the downward longwave

radiation flux with a pyrgeometer every 2 seconds (for a description of the devices and the data processing see *Kalisch and Macke [2012]*). Precipitation was monitored using an optical disdrometer [*Großklaus et al., 1998*] and the ship's rain gauge [*Hasse et al., 1998*]. A description of the analysis inferring precipitation from the ship's rain gauge is given by *Bumke and Seltmann [2012]*. The reflected shortwave radiation was computed according to *Taylor et al. [1996]*, while upward longwave radiation ( $F_{LW}$ ) was calculated according to the Stefan-Boltzmann law,  $F_{LW} = 0.97\sigma SST^4$ , where  $\sigma$  is the Boltzmann constant, assuming an emissivity of 0.97 for the sea surface. Turbulent heat fluxes and evaporation were computed from the ship's weather station data by using the parameterization of *Bumke et al. [2014]*.

The

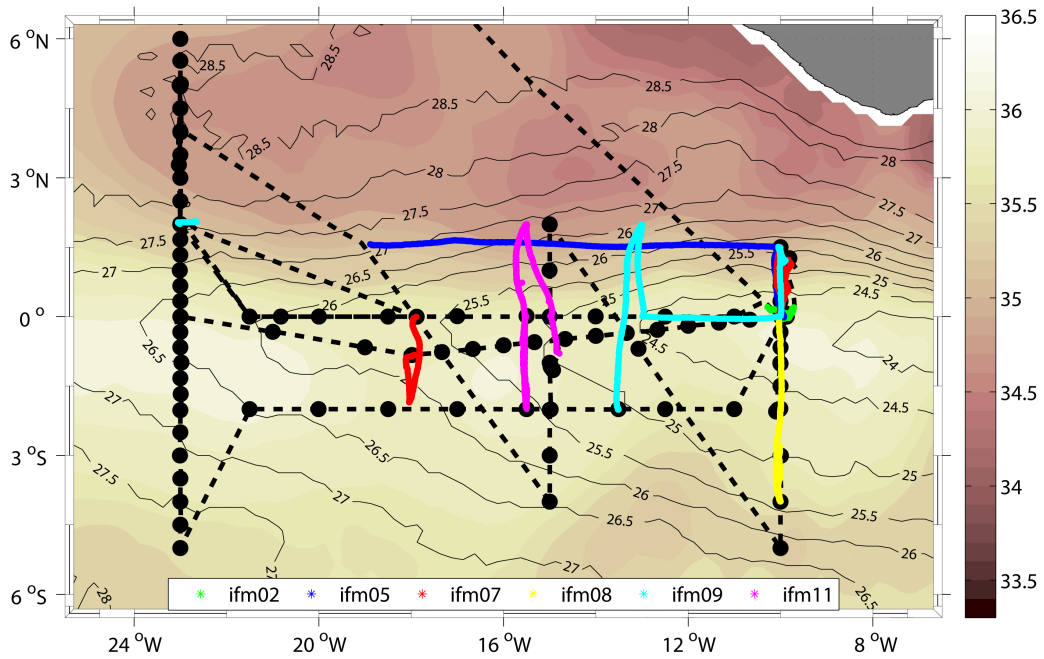


**Fig. 3.2:** Cold tongue experiment conducted between May and July 2011. Colored lines denote the glider tracks, dashed black lines show cruise tracks, and black dots are CTD stations. Background colors show 3-month mean SSS from SMOS with contour interval 0.1, while contour lines show 3-month mean SST from TMI in °C. Contour interval is 0.5 °C.

### 3.3 Glider data

A comparatively new oceanographic measurement device is a glider. Gliders are profiling Autonomous Underwater Vehicles (AUVs), driven thermally oder electrically. They change their density by pumping oil in a rubber bladder. The volume increases (mass is constant) and the glider gets lighter. This up- and downward movement gets an additional horizontal component through the tilting of the glider and the wings. Tilting is achieved through moving a battery package for- and backward. With this movement the center of mass is changed and the glider gets tilted. The shape of the wings finally yields a horizontal movement. A depth-time plot of a glider deployment has ususally a sawtooth shape. The usual payload of a Slocum electric glider, as used at GEOMAR, is a common CTD-system, an oxygen optode and sensors for chlorophyll and turbidity.

Six gliders provided during the CTE temperature and salinity profiles at approximately 3-4 km horizontal resolution and to maximum depths of 800 m. Altogether ten glider deployments (Fig. 3.3), mostly along meridional sections (Fig. 3.2), were performed during the CTE, yielding in a total of about 5600 profiles. Thermal lag hysteresis in salinity calculations was corrected by applying the method of *Garau et al.* [2011], where four correction parameters are determined by minimizing the area between two temperature-salinity curves of successive CTD-casts.

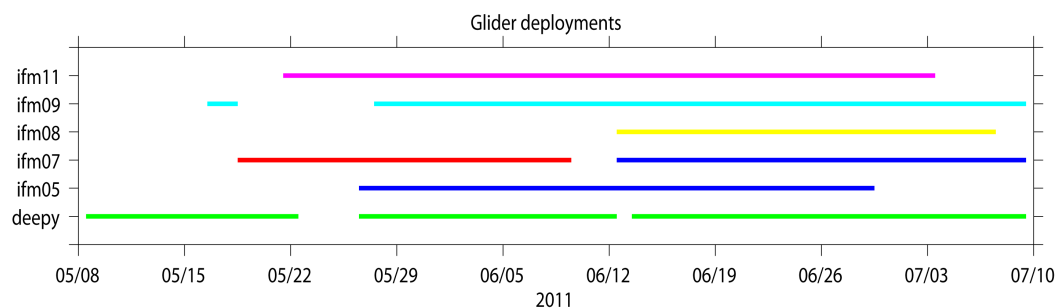


**Fig. 3.3:** Overview of glider deployment times. (cf. Fig. 3.2)

**Tab. 3.1:** Amount of profiles for every glider deployment in 2011. The number of total profiles are all dives (one dive is equal to two profiles). The number of profiles with data results from the use of the scientific sensors.

Glider	Deployment	Period (dd/mm)	#Profiles total(with data)
deepy	14	08/05-22/05	374(289)
deepy	15	26/05-12/06	650(455)
deepy	16	13/06-09/07	796(385)
ifm05	05	26/05-29/06	736(295)
ifm07	06	18/05-09/06	1388(878)
ifm07	07	12/06-09/07	1712(862)
ifm08	04	12/06-07/07	522(510)
ifm09	03	16/05-18/05	50(48)
ifm09	04	27/05-09/07	920(903)
ifm11	03	21/05-03/07	866(529)

## 3.4 Auxiliary datasets

### 3.4.1 Hydrographic data

Temperature and salinity profiles from Argo floats (provided by the US Global Ocean Data Assimilation Experiment (USGODAE)<sup>1</sup>) and time series of temperature and salinity from moored PIRATA buoys (provided by the Pacific Marine Environmental Laboratory (PMEL)<sup>2</sup>) were additionally used to supplement the hydrographic dataset (Fig. 3.4).

Argo floats are similar to gliders in their mode of operation. They are battery driven and climb and sink through density changes. Usually they drift in their parking depth of 1000 m for ~9 days. After sinking down to approximately 2000 m depth, they start climbing to the surface and profiling the water column. Their usual payload is a common CTE and an oxygen optode. Additional sensors can be mounted. After reaching the surface, they transmit their data while drifting at the surface. Finally they sink down again to their parking depth. Argo float profiles were used within the corresponding area of the ACT box or the northern box. Only profiles with quality control flag ,very good‘ and ,good‘ are

<sup>1</sup>Argo data were collected and made freely available by the International Argo Project and the national initiatives that contribute to it (<http://www.argo.net>). Argo is a pilot programme of the Global Ocean Observing System.

<sup>2</sup>PIRATA mooring data were provided by the TAO Project Office of NOAA/PMEL (<http://www.pmel.noaa.gov/tao/disdel/disdel.html>)

used. Time series of temperature and salinity with daily resolution were used for the CTE and for the seasonal cycles.

For the CTE, timeseries of temperature and salinity profiles are used from three different buoys. Two at the equator at 23°W and at 10°W and one from the Northeast Extension at 4°N latitude and 23°W longitude. Here are daily averages used from different depths (Tab. 3.2) and interpolated vertically to a 1 m resolution.

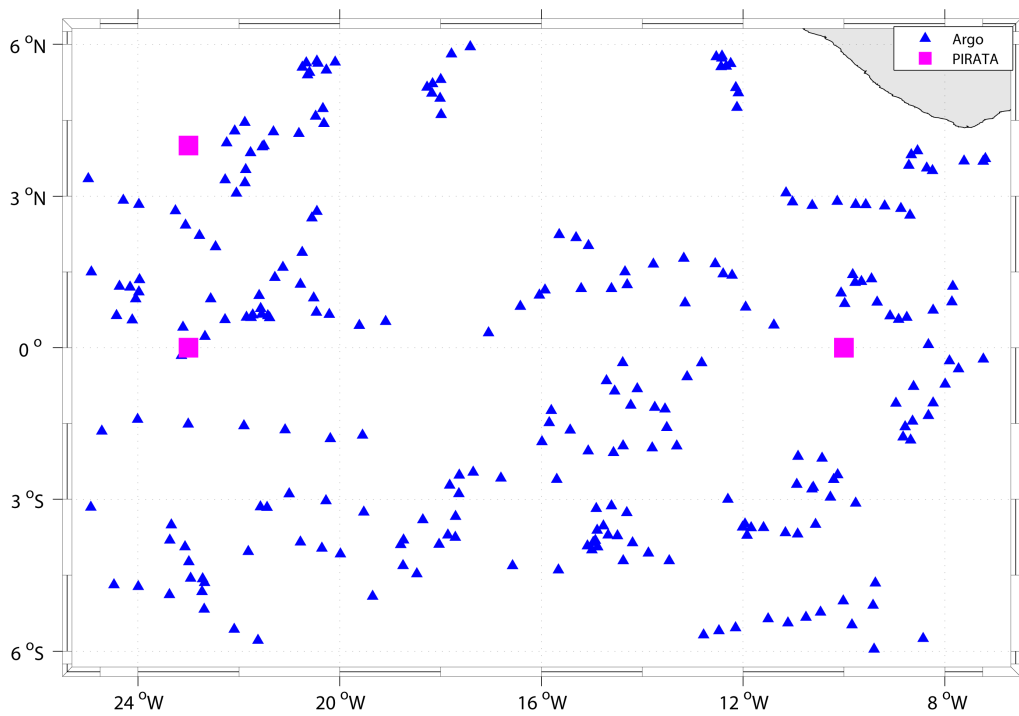


**Fig. 3.4:** Position of Argo floats profiles (blue) and PIRATA buoys (magenta) during the CTE.

### 3.4.2 Atmospheric data

For the calculation of the surface radiative and turbulent heat fluxes and the freshwater flux several products were compared with in-situ shipboard measurements which are a combination of onboard radiation and rain measurement devices, a pyranometer/pyrgeometer system and an optical disdrometer. Several atmospheric data products for the calculation of the surface radiative and turbulent heat fluxes and the freshwater flux were compared with the shipboard measurements.

**Tab. 3.2:** Depth coverage of temperature and salinity data at different PIRATA buoys. The equatorial buoy at 10°W was recovered and redeployed at the 8th of May (no data for this day). Additonal temperature depths (5 and 10 m) since the 9th of May. The equatorial buoy at 23°W was recovered and redeployed at the 8th and 9th of June (no data for these days).

Temperature				
Buoy		0°N, 10°W	0°N, 23°W	4°N, 23°W
Depth[m]				
1		x	x	x
5		x (since 9th)	x	
10		x (since 9th)	x	x
13				x
20		x	x	x
40		x	x	x
Salinity				
Buoy		0°N, 10°W	0°N, 23°W	4°N, 23°W
Depth[m]				
1		x	x	x
10				x
20		x	x	x
40		x	x	x

In particular, the ERA-Interim reanalysis [Dee *et al.*, 2011] from the European Centre for Medium-Range Weather Forecasts (ECMWF) were used for the net shortwave radiation, net longwave radiation, latent and sensible heat flux, evaporation and precipitation. They provide 12-hourly data at  $0.75^\circ$  resolution. The second product that provides all fluxes is the NCEP2 reanalysis [Kanamitsu *et al.*, 2002] from the National Center for Environmental Prediction (NCEP) with daily fields at  $1.875^\circ$  resolution. All radiative and turbulent heat fluxes and evaporation are also provided as TropFlux<sup>3</sup> products [Praveen Kumar *et al.*, 2012] on a  $1^\circ \times 1^\circ$  grid in the tropics ( $30^\circ\text{S}$ - $30^\circ\text{N}$ ) and at daily resolution. On the same spatial (but global) and temporal resolution latent heat flux and evaporation were taken from the Objectively Analyzed air-sea fluxes (OAFlux) data from Woods Hole Oceanographic Institute [Yu *et al.*, 2008].

We computed daily mean heat fluxes and evaporation along the cruise track of the research vessel using meteorological data for the estimation of the turbulent heat fluxes and evaporation. Bulk transfer coefficients were used from the parameterization of Bumke *et al.* [2014]. They estimated the transfer coefficients for the latent and the sensible heat fluxes and the drag coefficient with the Inertial dissipation method from several R/V Polarstern transects across the Atlantic and compared their results with the COARE parametrization of Fairall *et al.* [2003]<sup>4</sup>. In this study also the COARE parametrization was tested and the results were quite similar. All considered atmospheric products were interpolated on a regular  $1^\circ \times 1^\circ$  grid and averaged over 24 hours. The grid-boxes on the  $1^\circ \times 1^\circ$  grid covered by the vessel on one day were then averaged. Bias, standard deviation and root-mean-square of the differences are shown in Tab. 3.3.

A comparison between the shipboard determined evaporation and the aforementioned products (Fig. 3.5) shows a good agreement between all datasets. The comparison of the statistical parameters (bias, standard deviation and rms-difference) of the several products against the in-situ shipboard measurements (Tab. 3.3) indicate a slightly better agreement in the two combined datasets (OA-Flux and TropFlux) against the reanalysis products. Striking in all datasets is the evaporation minimum between the 8th and the 12th of June,

<sup>3</sup>The TropFlux data is produced under a collaboration between Laboratoire d'Océanographie: Expérimentation et Approches Numériques (LOCEAN) from Institut Pierre Simon Laplace (IPSL, Paris, France) and National Institute of Oceanography/CSIR (NIO, Goa, India), and supported by Institut de Recherche pour le Développement (IRD, France). TropFlux relies on data provided by the ECMWF Re-Analysis interim (ERA-I) and ISCCP projects.

<sup>4</sup>Matlab program codes cor3\_0af.m and cor3\_0ah.m, available from [ftp://ftp1.esrl.noaa.gov/users/cfairall/bulka/gcor3\\_0/matlab3\\_0/](ftp://ftp1.esrl.noaa.gov/users/cfairall/bulka/gcor3_0/matlab3_0/)



when the ship headed eastward close to the and slightly south of the equator. A maximum was observed at the 14th of June, when heading northward a region (between 1°N and 4°N) of anomalously dry air was passed, which resulted in enhanced evaporation. The NCEP estimates mostly overseeded the other datasets.

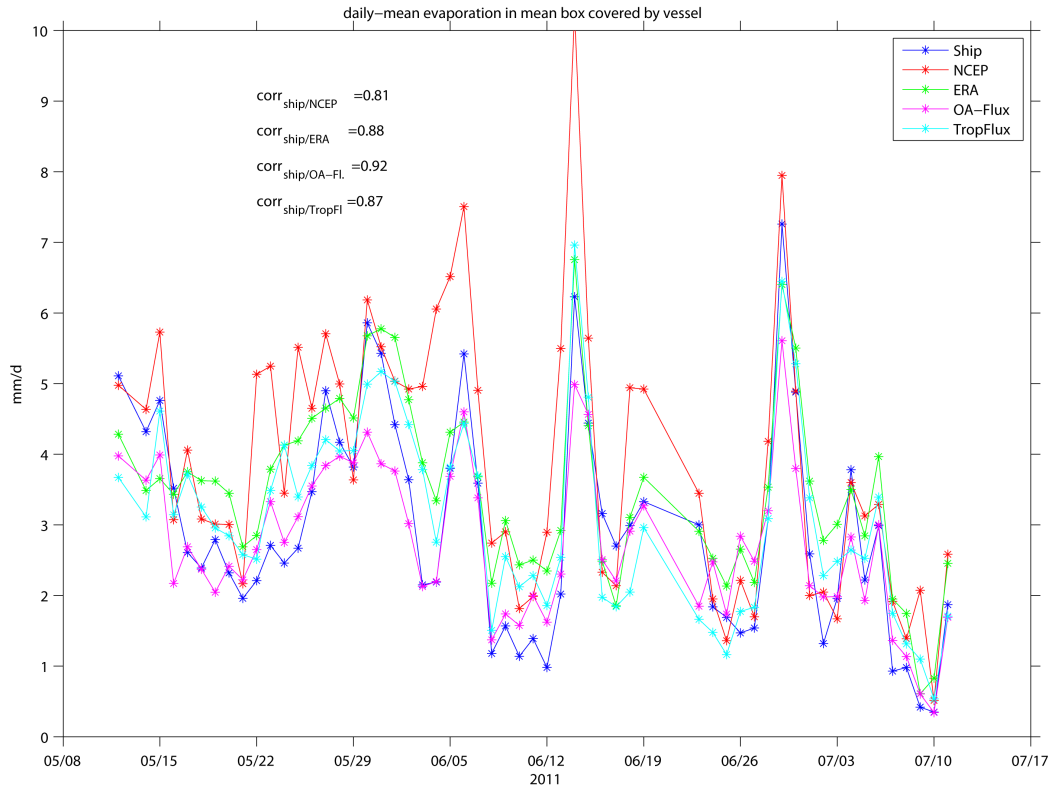


**Fig. 3.5:** Along cruise track comparison of ship data (blue) and reanalysis and satellite data for evaporation.

The comparison for the net surface solar radiation resulted in the best agreement for ERA-Interim (Fig 3.6a) when taking the correlation to the ship data into account. The estimates of NCEP and TropFlux had significantly lower correlations. In particular the strong deviations in the NCEP dataset are striking. The correlation for the net surface thermal radiation between the ship data and the other datasets showed reasonably well agreements for ERA-Interim and TropFlux and less correlation again for NCEP (Fig 3.6b). The results for the latent heat flux (Fig 3.6c) are per definition comparable to the evaporation estimates (cf. Fig. 3.5). The comparison of the statistical parameters (bias, standard deviation and rms-difference) of the several products against the in-situ shipboard measurements (Tab. 3.3) indicate larger than observed latent heat fluxes into the atmosphere

in the equatorial regions in the reanalysis products. These biases were also found in validation studies by *Kubota et al.* [2003] and *Kinzel* [2013]. The sensible heat flux (generally small in magnitude) best agreed in the TropFlux estimate (Fig 3.6d).

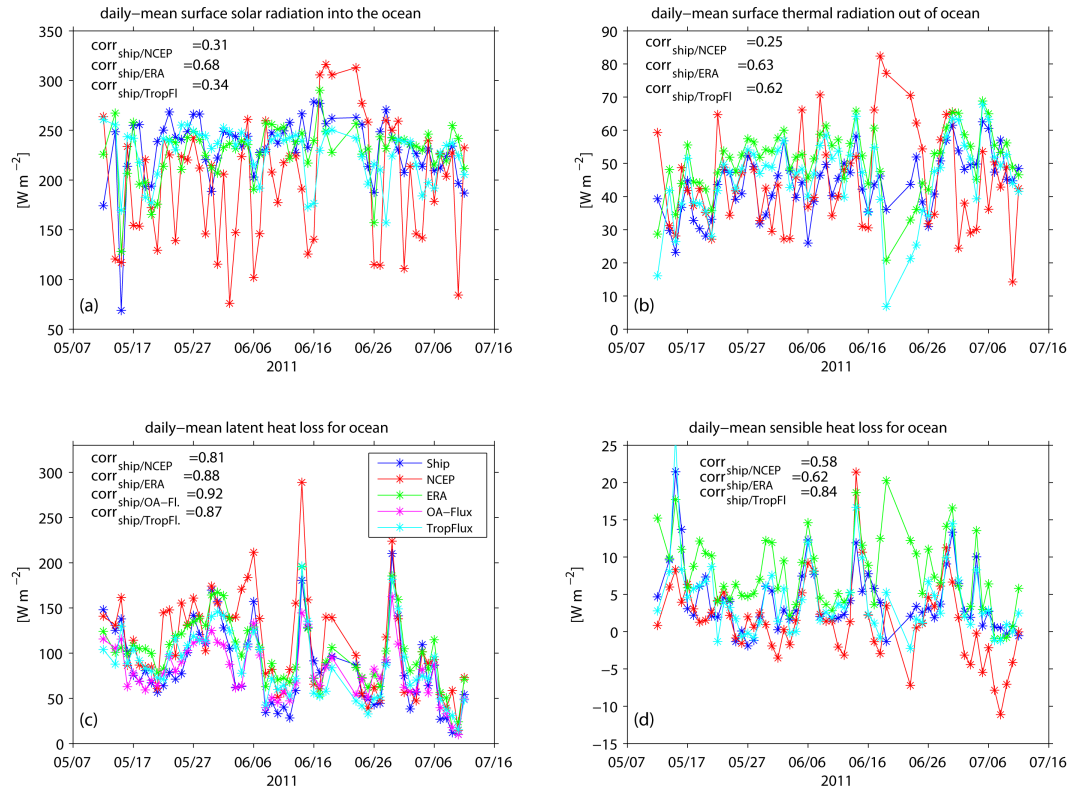


**Fig. 3.6:** Along cruise track comparison of ship data (blue) and reanalysis and satellite data for net incoming surface shortwave radiation (a), net outgoing surface thermal radiation (b), latent heat flux (c), and sensible heat flux (d) out of the ocean.

When considering the several statistical parameters mentioned before the turbulent heat fluxes, evaporation, as well as net surface shortwave and longwave radiation were in the following taken from the TropFlux product. Another product might fit better for a particular heat flux, but overall the TropFlux product showed the best agreement for all fluxes together.

Precipitation was taken from the Advanced Microwave Scanning Radiometer (AMSR-E) onboard the NASA Aqua spacecraft, from TMI, as well as from the Special Sensor Microwave Imager Sounder (SSMIS) F17 onboard the DMSP satellite<sup>5</sup>. The methodology

<sup>5</sup>SSMIS data are produced by Remote Sensing Systems and sponsored by the NASA Earth Science MEa-

**Tab. 3.3:** Bias, standard deviation (std) and root-mean-square of the differences (rmsd) of shipboard in-situ observations and reanalysis/satellite products for evaporation (E), latent heat flux (LHF), sensible heat flux (SHF), net surface shortwave radiation (SSR) and net surface longwave radiation (SLR). Unit for E is  $\text{mm d}^{-1}$  while the unit for LHF, SHF, SSR and SLR is  $\text{W m}^{-2}$ .

	ERA-Interim		NCEP2		OAFlux		TropFlux	
	Bias $\pm$ std	rmsd	Bias $\pm$ std	rmsd	Bias $\pm$ std	rmsd	Bias $\pm$ std	rmsd
E	-0.6 $\pm$ 0.7	0.9	-0.7 $\pm$ 1.1	1.5	0.1 $\pm$ 0.7	0.7	-0.3 $\pm$ 0.7	0.8
LHF	-18.7 $\pm$ 21.0	26.3	-19.2 $\pm$ 31.5	40.2	0.2 $\pm$ 19.3	19.8	-7.2 $\pm$ 21.6	21.5
SHF	-2.9 $\pm$ 4.1	5.4	2.9 $\pm$ 4.5	5.2			0.1 $\pm$ 2.7	2.7
SSR	4.5 $\pm$ 24.9	24.9	28.4 $\pm$ 60.2	68.9			8.6 $\pm$ 34.4	34.6
SLR	-8.3 $\pm$ 8.0	10.5	-1.4 $\pm$ 15.1	15.0			-3.7 $\pm$ 9.6	9.6

used to compare in-situ data and satellite derived precipitation is described by *Bumke et al.* [2012] for the Baltic Sea and adapted here for the equatorial Atlantic.

Due to the high spatial and temporal variability of precipitation, a specific statistical analysis was used that compared in-situ precipitation measurements and satellite derived data or reanalysis data. This analysis follows the recommendations given by the World Meteorological Organization (WMO) for binary or dichotomous forecasts (a detailed description is provided through the “WWRP/WGNE Joint Working Group on Forecast Verification Research”<sup>6</sup>). For comparison we used hourly data. These one-hour averages of measured rain rates were compared to hourly interpolated fields. We allowed 65 km distance between ship and grid-point for AMSR-E, TMI, and SSMIS. For ERA-Interim we used 120 km and for NCEP2 240 km according to the datasets spatial resolution.

The bias score close to 1 for AMSR-E and SSMIS indicates similar rain probabilities as observed, while rain probabilities for NCEP2 are more than four times and that of ERA-Interim 14 times higher than observed. For TMI data, we estimated a bias score of 0.7. The statistical analysis suggests that we have to take into account that precipitation is a rare event. In this case, an estimate of the performance is the so-called threat score

SUREs DISCOVER Project. AMSR-E data are produced by Remote Sensing Systems and sponsored by the NASA Earth Science MEaSUREs DISCOVER Project and the AMSR-E Science Team. SSMIS and AMSR-E data are available at [www.remss.com](http://www.remss.com)

<sup>6</sup>[http://www.cawcr.gov.au/projects/verification/#Methods\\_for\\_dichotomous\\_forecasts/](http://www.cawcr.gov.au/projects/verification/#Methods_for_dichotomous_forecasts/)

or critical success index (CSI) instead of the correct proportion. The CSI is about 0.3 for the AMSR-E and SSMIS data compared to less than 0.15 for NCEP2, ERA-Interim and TMI. These results indicate that SSMIS and AMSR-E data give the most reliable information about precipitation. This is supported by biases in average rain rates, which are of the order of -15% to +30% for SSMIS and AMSR-E, -70% for TMI, +110% for NCEP2, and even +250% for ERA-Interim. The analysis revealed by taking the statistical parameters into account, that the AMSR-E satellite precipitation product was closest to the observations and it was finally chosen.

### 3.4.3 SST and SSS data

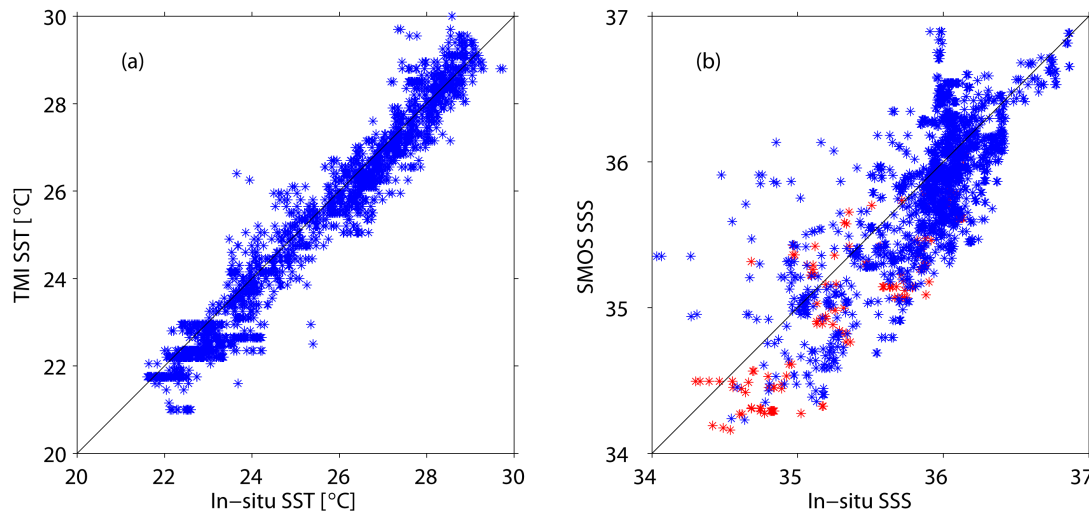


**Fig. 3.7:** Scatter plot of satellite SST with in-situ SST (a) and satellite SSS with in-situ SSS (b). Red dots in (b) denote satellite grid points where SMOS observations coincide with precipitation (rain rate  $\geq 0.1 \text{ mm h}^{-1}$ ) observations. The maximum distance between the closest satellite grid point and in-situ measurement is  $\sim 1/6^\circ$  or  $\sim 10 \text{ nm}$ .

All available surface data from glider, float and CTD measurements were used to compare in-situ and satellite data for the period from the 7th of May and the 11th of July in 2011 (Fig. 3.7). Satellite SST data was taken from the TMI onboard the TRMM satellite to calculate horizontal SST gradients. Three-day-means on a spatial grid of a quarter degree were used for the comparison between satellite SSTs and in-situ SST observations (Fig. 3.7a) and satellite SSS and in-situ SSS observations (Fig. 3.7b). The maximum distance between the closest satellite grid point, from 3-day-mean SST and SSS satellite images, and in-situ measurement is  $\sim 1/6^\circ$  or  $\sim 10 \text{ nm}$ . Satellite and in-situ SST data agree well

(Fig. 3.7a) with a correlation coefficient of 0.98. An offset of  $0.17^{\circ}\text{C}$  was added to the satellite SSTs and a standard deviation of  $0.52^{\circ}\text{C}$  was taken as the error for the satellite SSTs.

Horizontal SSS gradients were calculated based on the SMOS data. SMOS SSS measurements on a  $1^{\circ}\times 1^{\circ}$ -grid and with 10-day composites have, compared to Argo SSS, a current bias of  $\sim 0.3\text{--}0.4$  (Reul *et al.* [2012]; Boutin *et al.* [2012]). Here, we used the 3-day-mean fields on a quarter-degree grid to compare the satellite SSSs with in-situ SSS observations (Fig. 3.7b). As expected for the SSS, the correlation was lower, with a correlation coefficient of about 0.77. The local nature of freshwater anomalies, due to the lack of an air/sea feedback, is expected to be one reason but also the differences in the observed ocean volume contribute. For example the dispersion of a freshwater anomaly due to a local rainfall event will be very much confined to the upper first centimeters of the water column and may not be recognized in the near surface in-situ data. This measurement was typically taken below one meter depth (see e.g. Boutin *et al.* [2013]). This can be evidenced when evaluating SMOS SSS observations coinciding (within 3-day averages) with precipitation events (rain rate  $\geq 0.1 \text{ mm h}^{-1}$ ) as observed by AMSR-E. These data points indicate a mean bias of MLS compared to satellite SSS of  $-0.39$  (SMOS minus in-situ). Since only 8% of the SSS data coincide with precipitation data the total bias reduced to  $-0.11$ . Hence, for all satellite SSS data points an offset of  $0.11$  was added and a standard deviation of  $0.34$  was applied.

### 3.4.4 Velocity data

Surface velocities within the entire study region were required to estimate the advection terms. Due to the temporal resolution of surface velocity data needed for our analysis, the Ocean Surface Current Analysis Real-time (OSCAR) product is used, which is derived from sea level measurements, wind stress and SST data [Lagerloef *et al.*, 1999]. This dataset represents vertical averaged geostrophic and Ekman velocity in the upper 30 m of the ocean [Bonjean and Lagerloef, 2002]. The filtered dataset at a horizontal resolution of  $1^{\circ}\times 1^{\circ}$  with a temporal resolution of 5-days is implemented here. Explanation and validation of the OSCAR product as well as error estimates are described in Johnson *et al.* [2007]. They found significant correlations (0.5-0.8) between the OSCAR velocities with moored current meters (MCMs), mADCPs, drifters and shipboard current profilers in the

variability of zonal currents in near-equatorial regions of the Pacific. Variability of meridional currents is significantly less correlated compared to the correlation of the zonal currents. The Atlantic Ocean was also examined but not shown in the paper and showed similar correlations. *Foltz et al.* [2012] found similar results at two mooring sites (4°N and 12°N) at 23°W in the equatorial North Atlantic by comparing 5-day averaged dates of OSCAR and MCMs. At 4°N they found a correlation of 0.8 for the zonal velocity and no correlation for the meridional velocity.

For the equatorial mooring at 10°W, we found correlations of 0.43 for the zonal velocity and -0.1 for the meridional velocity by applying the same method as *Johnson et al.* [2007] with 5-day averaged data and using almost 13 months of upward looking mADCP profiles. Data in the upper 10-12 meter of these profiles were discarded. To fill the gap of the upper 12 meter we extrapolated the profiles to the surface assuming constant shear. Afterwards the upper 30 m were averaged via trapezoidal integration.

The RMS of the differences was estimated with  $0.21 \text{ m s}^{-1}$  for the zonal velocity and  $0.06 \text{ m s}^{-1}$  for the meridional velocity. The same comparison for the same time period was done at the equatorial mooring at 23°W. A correlation between the zonal velocities of 0.66 and between the meridional velocities of -0.05 showed a slightly better correlation for the zonal component than at the equatorial mooring at 10°W. The RMS difference was estimated with  $0.17 \text{ m s}^{-1}$ . For the meridional velocities, a RMS of the differences of  $0.03 \text{ m s}^{-1}$  was calculated. Finally the mean of the RMS of the differences at both sites was taken as the uncertainty for the horizontal velocities in the ACT box, leading to  $0.19 \text{ m s}^{-1}$  for the zonal velocity and  $0.04 \text{ m s}^{-1}$  for the meridional velocity. The absence of correlation for the meridional velocity at both mooring sites highlights the fact that OSCAR cannot capture TIWs.

A comparison of OSCAR velocities with the mADCP velocities at the equatorial moorings at 23°W and 10°W showed increased variability in the zonal component (Figs. 3.8a and b) for OSCAR, while the variability of the meridional component (Figs. 3.8c and d) from OSCAR was much weaker than the mADCP data. As mentioned before OSCAR does not capture TIWs, which are clearly identifiable in the meridional component of the mADCP data.

In the northern box, the uncertainty estimates of *Foltz et al.* [2013] for the mooring at  $4^\circ\text{N}/23^\circ\text{W}$  were chosen, with a zonal uncertainty of  $0.10 \text{ m s}^{-1}$  and a meridional uncertainty of  $0.08 \text{ m s}^{-1}$ . They compared monthly OSCAR velocities with PIRATA currents (combination of ADCP and MCM) at three mooring sites ( $4^\circ\text{N}$ ,  $11.5^\circ\text{N}$ , and  $20.5^\circ\text{N}$ ) at  $23^\circ\text{W}$ . They excluded the equatorial mooring, which shows a large discrepancy in zonal velocities between OSCAR and the direct measurement in our comparison.

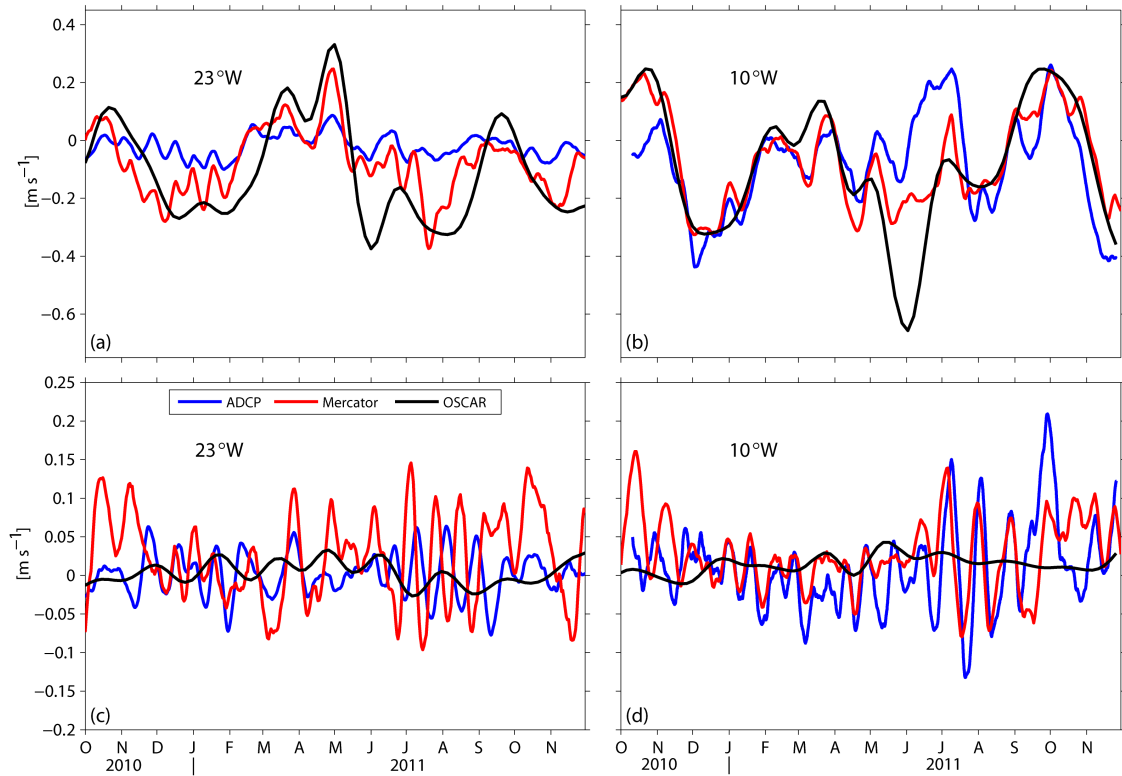


**Fig. 3.8:** ML-averaged zonal (a, b) and meridional (c, d) velocities at the equator at  $23^\circ\text{W}$  (a, c) and at  $10^\circ\text{W}$  (b, d). The black line denotes the OSCAR product and the red line is the Mercator estimate averaged for the same time period as OSCAR. The blue line denotes the 5-day mean subsurface ADCP-data.

### 3.4.5 Mercator assimilation model

In addition to the observational based data products, we used the “Mercator Global operational System PSY2V4R2” model output<sup>7</sup> in the analysis for estimating the horizontal advection terms and the entrainment. The model output correspond to a simulation that assimilates SST and sea level anomaly (SLA) fields, temperature and salinity profiles, and

<sup>7</sup>Mercator model output was provided by Mercator Ocean via contract 2011/SG/CUTD/56.

a mean dynamic topography. Three-dimensional fields of zonal and meridional velocities, temperature and salinity are provided. The horizontal resolution is  $1/12^\circ \times 1/12^\circ$  (9 km at the equator; decreasing pole ward) with daily fields. There are 36 vertical levels in the first  $\sim 1000$  meters. In the model, the vertical spacing changes from nearly one meter close to the surface to about 150 meters at 1000m depth [Lellouche *et al.*, 2013].

These velocities were also compared to the OSCAR and mADCP data (Fig. 3.8). In contrast to OSCAR the meridional Mercator velocities capture TIWs (Figs. 3.8c and 3.8d), which can have effects on the heat budget through horizontal eddy heat advection [Foltz *et al.*, 2003; Giordani *et al.*, 2013; Jochum *et al.*, 2007; Peter *et al.*, 2006]. However, particularly in the western cold tongue region, TIWs were out of phase compared to direct observations (Fig. 3.8c). Zonal velocities from OSCAR and Mercator showed some similar characteristics, such as the same phase and amplitude, but had large differences (Figs. 3.8a and 3.8b). In particular the large westward OSCAR velocities during the CTE in the central cold tongue region (Fig. 3.8b) were not identifiable in the Mercator output.

### 3.4.6 Data for the mean seasonal cycles of MLS

A unique dataset of microstructure shear and temperature profiles and CTD salinity profiles was used to estimate the dissipation rates of TKE. The dataset was collected during 9 cruises to the ACT region carried out in different seasons between 2005 and 2012. A detailed description of data set and post-processing procedures are given in Hummels *et al.* [2013] and in Hummels *et al.* [2014]. For this study, the dataset was supplemented by microstructure data from the R/V Maria S. Merian cruise MSM18/3. From the data set mentioned above, only profiles in proximity to the PIRATA buoys on the equator at  $10^\circ\text{W}$  and  $23^\circ\text{W}$  and to the buoy at  $4^\circ\text{N}$ ,  $23^\circ\text{W}$  were used. At these locations the seasonal cycles of the terms contributing to the seasonal salinity budgets were estimated.

All available buoy and mooring data from January 1999 until December 2012 (first dates used: 01/30/1999 for  $0^\circ\text{N}$ ,  $10^\circ\text{W}$ ; 03/07/1999 for  $0^\circ\text{N}$ ,  $23^\circ\text{W}$ ; 06/12/2006 for  $4^\circ\text{N}$ ,  $23^\circ\text{W}$ ) and several climatological products were used. Surface velocities were constructed from a combination of the YOMAHA'07 data set [Lebedev *et al.*, 2007] and available drifter trajectories. The YOMAHA'07 velocities were derived from ARGO float trajectories and provided from the Asia-Pacific Data Research Center and the International Pacific Re-



search Center (APDRC/IPRC). The drifter data are downloaded from the Drifter Assembly Center (DAC<sup>8</sup>). A detailed description of the construction of the combined velocity product is given by *Perez et al.* [2013]. For comparison, the YOMAHA'07 velocities and the drifter velocities were used on their own as well.

The horizontal salinity gradients were constructed from the global monthly mean salinity dataset from the Japan Agency for Marine-Earth Science and Technology (JAMSTEC<sup>9</sup>). This dataset is derived from Argo float observations which are binned to  $1^\circ \times 1^\circ$  monthly means from January 2001 ongoing [*Hosoda et al.*, 2008]. We used the data until December 2012.

Monthly means from AMSRE precipitation (beginning in June 2002) and TropFlux evaporation (beginning in January 1999), and 3-day averages of SMOS SSS (beginning in January 2010) and TMI SST (beginning in January 2010), until December 2012 were used as well. as well. The MLD climatology of *de Boyer Montegut et al.* [2004] was implemented to derive the horizontal gradients of the MLD. The MLDs were interpolated on a  $1^\circ \times 1^\circ$  grid and the gradients were estimated with central differences on that grid.

The atmospheric datasets described in section 3.4.2 were here used again to compare the impact of the particular dataset on the net surface freshwater flux. Two additional monthly precipitation climatologies were implemented, the CPC Merged Analysis of Precipitation (CMAP<sup>10</sup>, *Xie and Arkin* [1997]) and the Global Precipitation Climatology Project (GPCP, *Adler et al.* [2003]). Both monthly datasets are provided on a  $2.5^\circ \times 2.5^\circ$  grid. Finally, the AMSR-E precipitation (beginning in June 2002) and TropFlux evaporation (beginning in January 1999) until December 2012 were used, matchable to the CTE methodology.

<sup>8</sup>[www.aoml.noaa.gov/phod/dac/](http://www.aoml.noaa.gov/phod/dac/)

<sup>9</sup>[http://www.jamstec.go.jp/ARGO/J\\_ARGOe.html](http://www.jamstec.go.jp/ARGO/J_ARGOe.html)

<sup>10</sup>CMAP Precipitation data provided by the NOAA/OAR/ESRL PSD, Boulder, Colorado, USA, from their Web site at <http://www.esrl.noaa.gov/psd/>

## 3.5 Methodology

### 3.5.1 Heat and freshwater budgets

The ML heat balance can be expressed as follows (*Stevenson and Niiler [1983]; Foltz et al. [2003]*)

$$\rho c_p h \frac{\partial T}{\partial t} = -\rho c_p h (\vec{u} \cdot \nabla T + \overline{\vec{u}' \cdot \nabla T'}) - \rho c_p w_e \Delta T + q_0 + R. \quad (3.1)$$

$T$  is the MLT,  $t$  is time,  $h$  is the MLD,  $\vec{u}$  is the ML-averaged horizontal velocity,  $\Delta T = T - T_{-h}$  is the difference between  $T$  and the temperature 5m below the base of the ML ( $T_{-h}$ ), and  $w_e$  is the entrainment velocity.  $\rho$  is the density of the mixed layer,  $c_p$  the specific heat capacity at constant pressure and  $q_0$  is the net heat flux through the ocean's surface corrected for the penetrative shortwave radiation through the ML base.

The local heat storage on the left hand side of equation 3.1 is balanced by lateral temperature advection (divided into a mean and an eddy part), entrainment into the mixed layer, net surface heat flux and a residual term  $R$ . The residual represents the sum of all unresolved physical processes and the accumulation of errors from the other terms. The net heat flux at the ocean's surface is the sum of the net (incoming minus reflected) shortwave radiation - corrected for the amount penetrating below the ML -, the net longwave radiation, the latent heat flux and the sensible heat flux.

Similarly the balance for salinity is after e.g. *Delcroix and Henin [1991]* given by:

$$h \frac{\partial S}{\partial t} = -h (\vec{u} \cdot \nabla S + \overline{\vec{u}' \cdot \nabla S'}) - w_e \Delta S + (E - P)S + R \quad (3.2)$$

$S$  is the average salinity in the ML (i.e. MLS),  $E$  is the evaporation,  $P$  is the precipitation, and  $\Delta S = S - S_{-h}$  is the difference between  $S$  and the salinity 5m below the base of the ML ( $S_{-h}$ ). The first term on the right hand side of equation 3.2 describes the horizontal advection of salt (divided into a mean and an eddy part) and the second term represents salt entrainment through the ML base. The third term is the freshwater flux through the ocean's surface, while  $R$  again represents the residual including the sum of all unresolved physical processes and the accumulated errors of the other terms.

According to *Stevenson and Niiler [1983]* the entrainment velocity may be defined as

$$w_e = H\left(\frac{\partial h}{\partial t} + w_{-h} + \vec{u} \cdot \nabla h\right) \quad (3.3)$$

The entrainment velocity is the sum of the local change in mixed layer depth with the time, the vertical velocity  $w_{-h}$  at the mixed layer base and the horizontal advection of MLD ( $\vec{u} \cdot \nabla h$ ). Only the upward movement (entrainment) in equation 3.3 was considered because downward movement (detrainment) did not affect the temperature or the salinity in the mixed layer. This constraint was implemented with the use of the Heaviside unit function, defined as

$$H(x) = \begin{cases} 1, & x \geq 0 \\ 0, & x < 0 \end{cases} \quad (3.4)$$

### 3.5.2 Calculation of the individual terms for the CTE

#### Mixed layer depth

The ML can be defined as a layer of constant potential density and hence the depth where the density starts to increase is the MLD. A second definition of the ML is a layer of constant temperature. Here, the depth where the temperature starts decreasing is called isothermal layer depth (ILD). The MLD and the ILD are calculated using density and temperature profiles. The ILD was determined as the depth at which temperature is 0.5°C lower than the temperature averaged between 2 and 6 meters depth. The MLD was defined as the depth where the potential density has increased equivalently to a temperature decrease of 0.5°C while salinity and pressure are held constant. The required potential density increase was about  $\sim 0.15\text{-}0.16 \text{ kg m}^{-3}$ . We avoided effects of diurnal cycles in MLD/ILD for the temporal averaging of fluxes through the ML base by using these definitions. Diurnal cycles were present when using 0.2°C ILD-criterion (for MLD  $\sim 0.06 \text{ kg m}^{-3}$ ). No significant difference between MLD and ILD was found in the high resolution glider data at all locations. Therefore the simpler temperature criterion was chosen for our definition of the MLD.

#### Advective transports

Advection of heat and salinity was estimated by calculating  $\vec{u} \cdot \nabla T$  and  $\vec{u} \cdot \nabla S$  using ve-

locities from the OSCAR product and horizontal temperature and salinity gradients from satellites as well as Mercator model output. The advections terms determined from the observations were calculated on the OSCAR-native a  $1^\circ \times 1^\circ$  grid. Horizontal gradients of satellite SST and SSS were calculated using central differences of the  $1/4^\circ$  gridded data set that were subsequently averaged onto the  $1^\circ \times 1^\circ$  grid. Finally, the  $1^\circ \times 1^\circ$  advection terms spatially averaged for the two boxes described in section 3.1.

Velocities as well as horizontal temperature and salinity gradients from the Mercator model were provided as daily averages on a  $1/12^\circ \times 1/12^\circ$  grid. The velocities were averaged in the upper 30 meters using trapezoidal integration in order to be comparable to the OSCAR estimates. Advection of heat and salinity was then estimated by calculating  $\vec{u} \cdot \nabla T$  and  $\vec{u} \cdot \nabla S$  on the  $1/12^\circ \times 1/12^\circ$  grid and subsequent averaging for the two boxes described above. Finally, the advective terms from the observations and from the Mercator model were temporally-averaged as 10-day means.

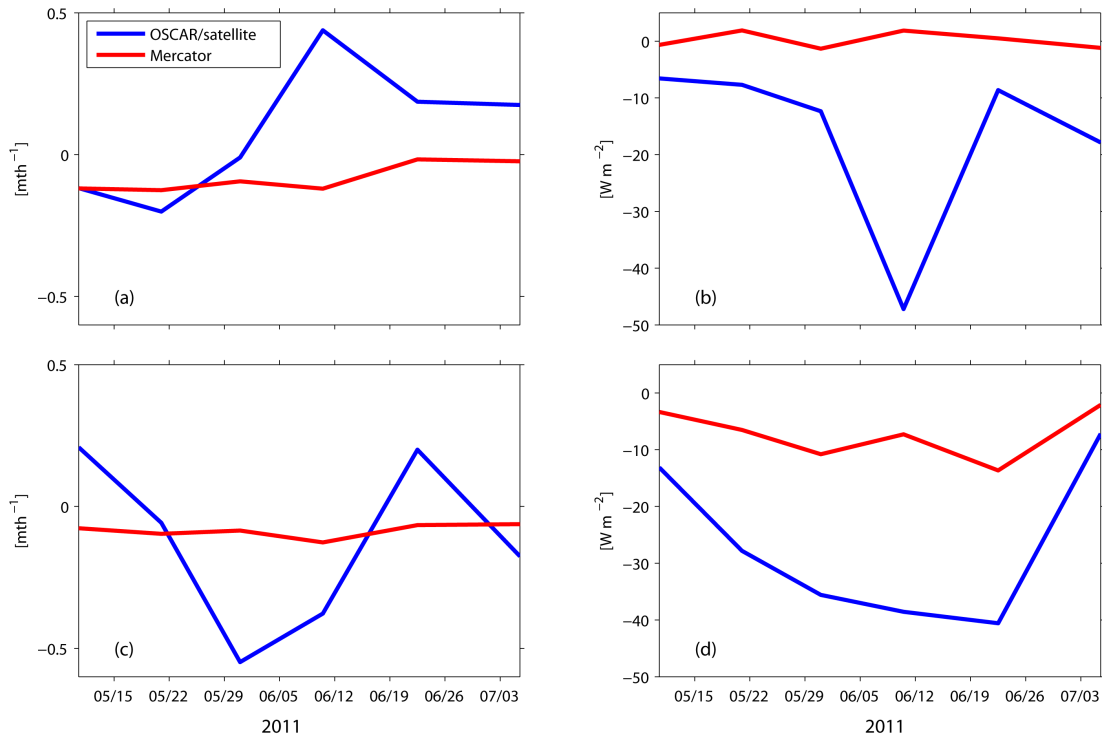


**Fig. 3.9:** Box- and time-averaged zonal salinity (a, c) and zonal heat (b, d) advection for the North box (a, b) and for the ACT box (c, d). The blue line denotes the OSCAR product together with lateral salinity gradients from SMOS and temperature gradients from TMI. Red is the Mercator output. Note, that the model gradients are vertically averaged in the ML.

A comparison of the spatially averaged advection terms in the two boxes showed that zonal heat and salinity advection determined from the Mercator model output was reduced compared to those determined from the observations (Fig. 3.9). The main reason for these discrepancies is the weaker zonal velocity in the Mercator data compared to the OSCAR estimates for the CTE period, e.g. seen at the equatorial buoy sites at 23°W and 10°W (Figs. 3.8a and 3.8b). But, differences in the horizontal gradients are also possible. Here are surface gradients from the satellite products compared with ML averaged gradients from the model output.

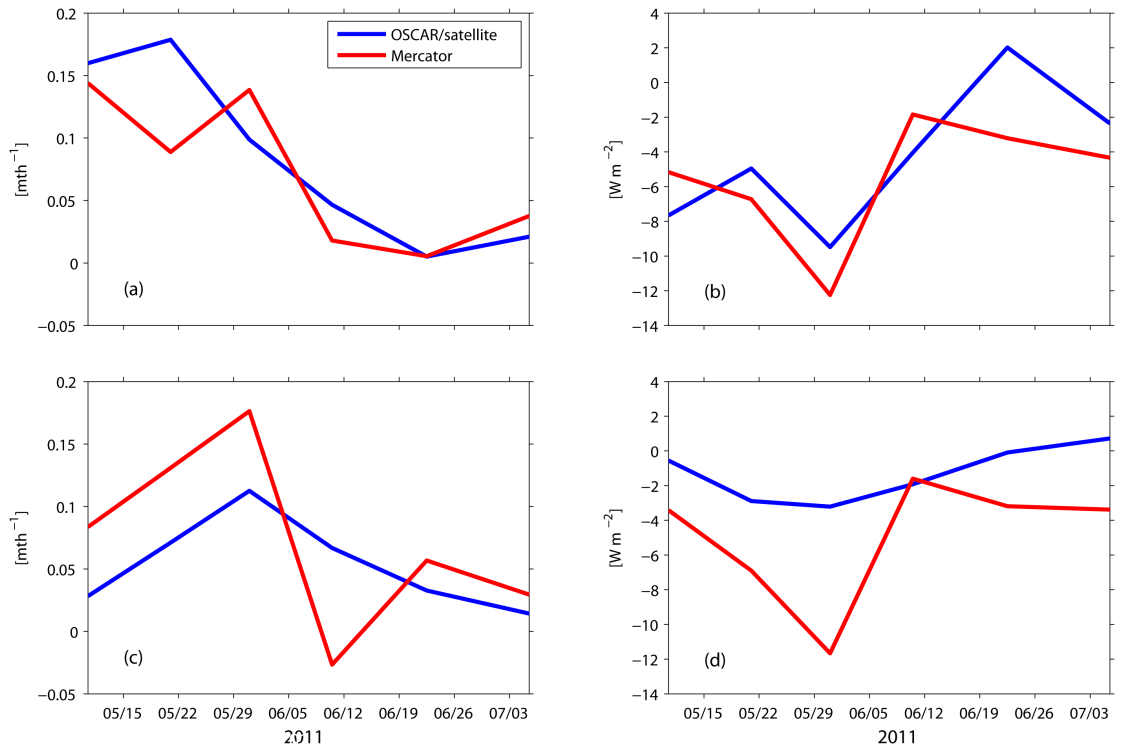


**Fig. 3.10:** Box- and time-averaged meridional salinity (a, c) and meridional heat (b, d) advection for the North box (a, b) and for the ACT box (c, d). The blue line denotes the OSCAR product together with lateral salinity gradients from SMOS and temperature gradients from TMI. Red is the Mercator output. Note, that the model gradients are vertically averaged in the ML.

Differences in meridional heat and salinity advection (Fig. 3.10) between the two calculations were smaller than the zonal differences due to smaller total differences between the OSCAR and Mercator velocities. However, despite OSCAR meridional velocities are close to zero at the equator, the meridional advection terms in the ACT box (Figs. 3.10c and d) are not zero, but smaller than the model estimates. This will be further discussed

in chapter 5. Eddy or transient components of the advection terms were not estimated separately, because the time period considered in this study was too short to fully resolve eddy variability. Averaging over a large period in time and many eddies is necessary to obtain a meaningful contribution from eddy advection.

### Entrainment

Entrainment was calculated from the model output only. There were no observational vertical velocity estimates available at the ML base. The vertical velocity at the ML base was calculated using the continuity equation  $w_{-h} = h(\nabla \cdot \vec{u})$ . Horizontal gradients of ML velocity and MLD were estimated with central differences on the  $1/12^\circ \times 1/12^\circ$  grid. Local changes in MLD were derived on a daily basis.

### Surface heat and freshwater fluxes

All atmospheric datasets were re-gridded on a  $1^\circ \times 1^\circ$  grid. The penetrative shortwave radiation was calculated following *Wang and McPhaden* [1999] assuming an exponential decay of surface shortwave radiation with 25 m e-folding depth.

### Diapycnal diffusivities and fluxes

In regions where the stratification is dominated by temperature the diapycnal diffusivities of heat and mass are similar ( $K_h = K_\rho$ , e.g. *Peters et al.* [1988]). Using the observed dissipation rates the diapycnal diffusivity of mass was estimated following *Osborn* [1980]

$$K_\rho = \Gamma \frac{\epsilon}{N^2}. \quad (3.5)$$

$N^2$  is the buoyancy frequency and  $\Gamma$  the turbulent mixing efficiency.  $\Gamma$  is set constant to 0.2, which is commonly used in several other studies (e.g., *Moum et al.* [1989]; *Hummels et al.* [2013]). Further, the diapycnal heat flux was estimated using

$$J_{heat} = -\rho c_p K_\rho \frac{\partial T}{\partial z}. \quad (3.6)$$

For shear-driven turbulence the diapycnal diffusivity of salt ( $K_S$ ) is equal to the diapycnal

diffusivity of heat (e.g., *Osborn and Cox* [1972]; *Osborn* [1980]; *Schmitt et al.* [2005]) and, thus, equal to the diapycnal diffusivity of mass ( $K_S = K_h = K_\rho$ ). With this assumption the diapycnal salt flux was calculated using

$$J_S = -K_\rho \frac{\partial S}{\partial z}. \quad (3.7)$$

Diapycnal diffusivities, vertical temperature gradients, and vertical salinity gradients were averaged vertically in this study between 5 and 15 meters below the ML base. The upper boundary was chosen to exclude ML values from the average. *Lien et al.* [2008] and *Hummels et al.* [2013] showed that the diapycnal heat flux is highly divergent in the vertical and rapidly decreases below the ML base. Therefore, the average within the narrow layer between 5 and 15 meters below the ML base was used. Due to the limited amount of microstructure profiles available and the large variability inherent in turbulent mixing in the ocean, diapycnal fluxes were averaged for two periods: (1) the first half of the CTE (May until mid-June) and (2) the second half of the CTE (mid-June/July). Uncertainties of the fluxes were estimated from error propagation and boot strapping as detailed in *Hummels et al.* [2013].

### 3.5.3 Calculation of the individual terms for the seasonal cycles

#### Mixed layer depth

The MLD was defined equal to the definition during the CTE. The daily mean MLDs were averaged for all days of the year using all available data until December 2012. Afterwards monthly means were constructed. From these the temporal evolution of the MLD was calculated as well.

#### Advective transports

Horizontal advection was estimated by calculating  $\vec{u} \cdot \nabla S$  at the buoy. Monthly mean velocities were calculated on a  $1^\circ \times 1^\circ$  grid from all available float and drifter data. The monthly mean horizontal gradients of SSS from float observations were calculated with central differences on the same  $1^\circ \times 1^\circ$  grid and afterwards averaged for the mean seasonal

**Tab. 3.4:** Annual mean and annual standard deviation of regression coefficients (in  $^{\circ}\text{C}^{-1}$ ) between SSSs and SSTs. Shown are the values for the three buoy sites for satellite data and PIRATA buoy data.

	Satellite (SMOS/TMI)	PIRATA
0°N, 10°W	-0.25±0.11	-0.21±0.14
0°N, 23°W	-0.17±0.09	-0.18±0.17
4°N, 23°W	-0.12±0.13	-0.27±0.35

cycle. Note, that the salinity climatology captures only the time from January 2001 until December 2012.

Eddy salt advection ( $\overline{\vec{u}' \cdot \nabla S'}$ ) was estimated for the moorings by assuming a correlation between temperature and salinity fluctuations. Using the eddy heat advection ( $\overline{\vec{u}' \cdot \nabla T'}$ ) estimates from *Hummels et al.* [2014], the eddy salt advection was calculated via

$$\overline{\vec{u}' \cdot \nabla S'} = \overline{\vec{u}' \cdot \nabla T'} \frac{\delta S}{\delta T}. \quad (3.8)$$

The regression of SSS and SST ( $\frac{\delta S}{\delta T}$ ) was calculated on a monthly basis by using three years (2010-2012) of 3-day averages of satellite SSS and SST observations in a box  $2.5^{\circ} \times 2.5^{\circ}$  around the mooring and daily PIRATA SSS and SST observations from 1999 until 2012. The regression coefficient for one climatological month is calculated separately for the satellite and the buoy observations by taking the slope of the regression line of all pairs of SSS and SST observations in the particular month in all years. Finally the monthly mean of the monthly satellite and buoy regression coefficients are used. The monthly estimates from the two independent datasets are very similar in their developing over the year and their annual means (Tab. 3.4).

### Entrainment

Entrainment was calculated from the MLD gradients, the divergence of the monthly mean horizontal velocities and the local time derivatives at the PIRATA moorings.

### Surface freshwater flux



For all atmospheric datasets monthly means were used and averaged in mean months of the year.

#### Diapycnal diffusivities and fluxes

The diapycnal diffusivities and the vertical salinity gradients were used to calculate vertical averages below the ML base (MLD+5m to MLD+15m) for each profile accordingly to the CTE procedure. Then the diapycnal salt fluxes were estimated with equation 3.7 and monthly means of the fluxes were calculated afterwards.

#### Harmonic fitting

Annual and semiannual harmonics were fitted to all monthly averaged data. The total error of the fit ( $err_{tot}$ ) combines the data error ( $err_{data}$ ) and the error estimated as the standard deviation between the data and the fit ( $err_{fit}$ ) and is calculated with  $err_{tot} = \sqrt{err_{data}^2 + err_{fit}^2}$ . The data error consists of given uncertainties from the data provider and errors from averaging of daily or monthly data into monthly climatologies using error propagation.



# 4 The ACT in boreal summer 2011

## 4.1 Introduction

An overview over the conditions in the central and eastern equatorial Atlantic during the cold tongue development in 2011 is given in this chapter. On the one hand the observed fields at the surface are described. Main quantities of interest are the temperature and the salinity structure in the equatorial Atlantic and the horizontal gradients of the temperature and the salinity are also shown. The surface wind and the precipitation are other important quantities that directly influence the oceans surface and ML. A second view is the vertical distribution of the important properties. The hydrography (temperature and salinity) directly influences the density of the ocean and hence derive the mixed layer depth. Also the structure of the ocean circulation is described. This means the general structure of the currents as well as the preconditions for mixing related to the current shear. Mixing properties like vertical gradients, dissipation rates and diffusivities as well as an overview over the diapycnal fluxes is given at the end of this chapter.

## 4.2 Surface observations

The long term observations of SST and SSS at the PIRATA buoy sites at 23°W and 10°W on the equator can be used to investigate the exact timing of ACT development during 2011 in a larger temporal context (Fig. 4.1). At 23°W (western part of ACT region) SST (Fig. 4.1a) and SSS (Fig. 4.1c) observations align well with the average seasonal cycle at this location. In contrast, in the center of the cold tongue at 10°W, the onset of cooling was approximately one week earlier and the cooling was stronger in 2011 compared to the climatology (Fig. 4.1b). Similar, SSS exhibited an earlier and elevated increase this year (Fig. 4.1d)). The comparison shows that the time period of our experimental campaign



**Fig. 4.1:** Mean seasonal cycle (blue) of SST (a, b) and SSS (c, d) for the PIRATA buoy at 23°W at the equator (left; a, c) and 10°W at the equator (right; b, d) based on averaging all data from beginning of measuring period (SST/SSS at 23°W: 7th of March 1999; SST at 10°W: 15th of September 1997; SSS at 10°W: 29th of January 1999) to the end of 2012. The red line indicates SST and SSS in 2011, while the dashed vertical black lines illustrate the beginning and end of the CTE.

(May-July 2011) was well chosen in terms of studying the processes during cold tongue development as well as covering the entire cooling period in the center of the ACT. However, a large increase in 2011 SSS occurred most likely before the CTE.

The onset and spreading of the ACT in boreal summer 2011 is apparent in the monthly equatorial SST evolution (Figs. 4.2a, c, e, and g). The strongest cooling, resulting in minimum temperatures of less than 22°C, was found at the equator at around 10°W. In June and July the negative SST anomaly expanded further to the west- and southwest, but with a weaker intensity. The monthly satellite data showed a strong increase in SSS in the eastern equatorial Atlantic from April to May (Figs. 4.2b and d) followed by a period of nearly constant SSS (Figs. 4.2f and h). Away from the equator in the tropical North Atlantic, a reduction of SSS occurs from April through June which is associated with the northward migration of the ITCZ. From June to July, SSS increases in that region.

The zonal temperature advection (zonal velocity multiplied with the zonal temperature gradient at the surface) is shown from assimilation model results and from satellite observations for the months April until July in 2011 (Fig. 4.3). In April a positive temperature advection along the nSEC pathway was determined from the model output. The positive advection remained during the cold tongue development until July eastward of 10°W at the equator and slightly north of it. Westward of 10°W negative temperature advection was observed, in particular in June and July 2011. This was evident in model output data as well as satellite observations. This pattern of zonal advection reflected and confirmed the observation of the center of the cooling at 10°W around the equator. The amplitude of advection is higher in the model data, but the both independent results agreed quite well. It has to be mentioned here that the Mercator output is not at the surface, but is associated with a depth of 0.5 m. The SST data from TMI are per definition surface values (first few centimeters), while the OSCAR output is defined as valid for the first 30 m. When considering the model data from the upper 30 m (the OSCAR depth) the advection is much weaker (cf. Figs. 3.9b and d).

In Fig. 4.4 the monthly mean zonal salinity advection in the equatorial Atlantic is shown from assimilation model results and from satellite observations for the months April until July in 2011. The salinity gradients are taken from the surface. In April strong negative zonal salinity advection was observed in the eastern cold tongue region at and south of the equator (east of 0°E) and at the equator at ~ 8°W. Negative advection mostly north of the

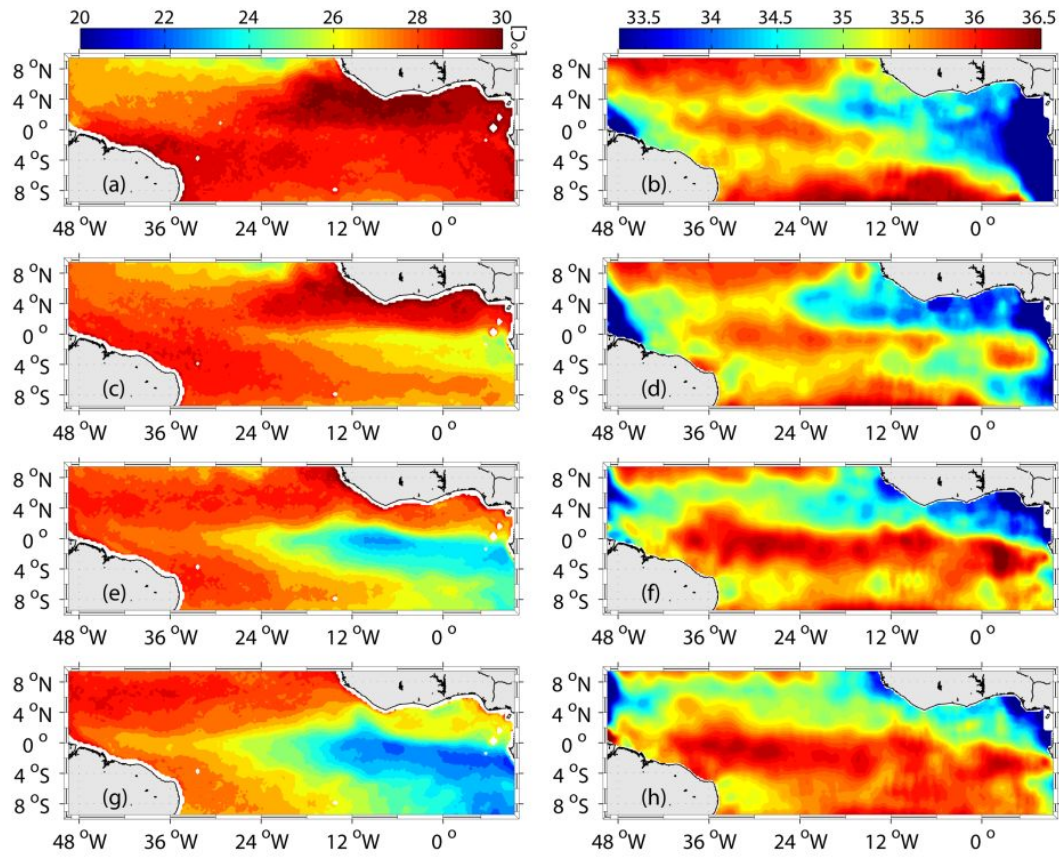


**Fig. 4.2:** Monthly mean fields of SST (a, c, e) from TMI and SSS (b, d, and f) from SMOS. Upper row is April (a, b), upper middle row is May (c, d) and lower middle row is June (e, f). Lower row is July (g, h)

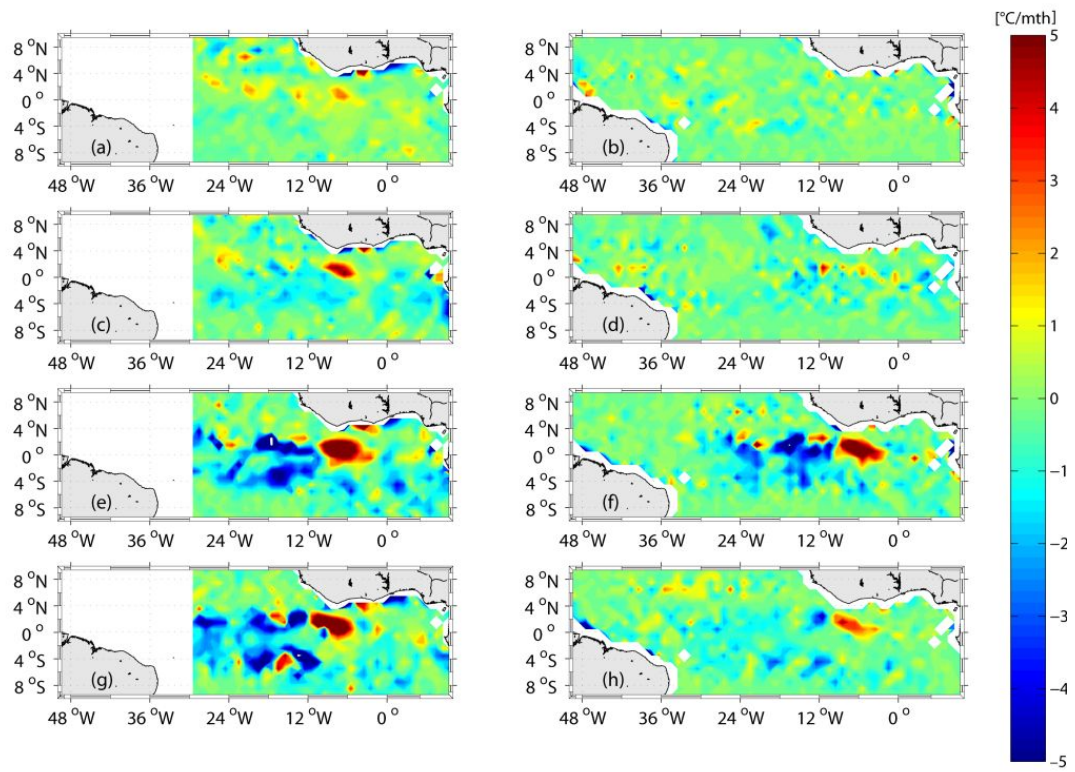


**Fig. 4.3:** Monthly mean zonal temperature advection from April (top row), May (second row), June (third row) and July (bottom row) 2011. Left Mercator model output, right TMI/OSCAR.

equator at the pathway of the nSEC was evident from the model results at the edges of the western cold tongue region. At approx.  $18^{\circ}\text{W}$  a local maximum of positive zonal salinity advection occurred. At the equator and south of the equator in the ACT (between  $23^{\circ}\text{W}$  and  $10^{\circ}\text{W}$ ) weaker advection was observed using the model output. The spatial distribution of the monthly mean zonal advection remained nearly constant throughout the CTE in the model. In July the zonal advection in the western cold tongue region and north of it weakened. The local maximum north of the equator around  $10^{\circ}\text{W}$  was still present in July. The region north of  $4^{\circ}\text{N}$  is mostly influenced through positive zonal advection.

The satellite data showed a strong advection along the path of the nSEC as well. But, in particular in May, the whole central cold tongue region around  $10^{\circ}\text{W}$  was under the influence of zonal advection. In June the region of strong advection again became narrower and covered the nSEC pathway, but still also influencing the equator. A second striking feature of the monthly mean advection is the sign. While the Mercator model output is mostly negative, meaning freshwater advection westward, the advection with the satellite data changed sign. The velocities were also westward, but the zonal salinity gradients partly eastward. This yielded to positive zonal advection, i.e. salt was advected westward. In particular this feature was observed in May and in June. Similar to the model output, the region north of  $4^{\circ}\text{N}$  is mostly influenced through positive zonal advection.

Similar to temperature advection it has to be mentioned here that the Mercator output is not at the surface, but is associated with a depth of 0.5 m. The SSS data from SMOS are per definition surface values (first few centimeters), while the OSCAR output is defined as valid for the first 30 m. However, the Mercator output vertically averaged for the upper 30 m (salinity and zonal velocity) had the same sign of the gradient, but the amplitude was much weaker (cf. Figs. 3.9a and c).

An intensification of the surface winds (Fig. 4.5) at the equator from April to May in 2011 came along with the cold tongue onset. In April weak winds were observed, in particular at and slightly north of the equator (Fig. 4.5a). In May, the southeasterlies crossed the equator in the EEA (Fig. 4.5b). This pattern of surface winds remained during the further development of the cold tongue in June and July 2011 (Figs. 4.5c,d).

The migration of the ITCZ, defined as the convergence region of south- and northeaster-



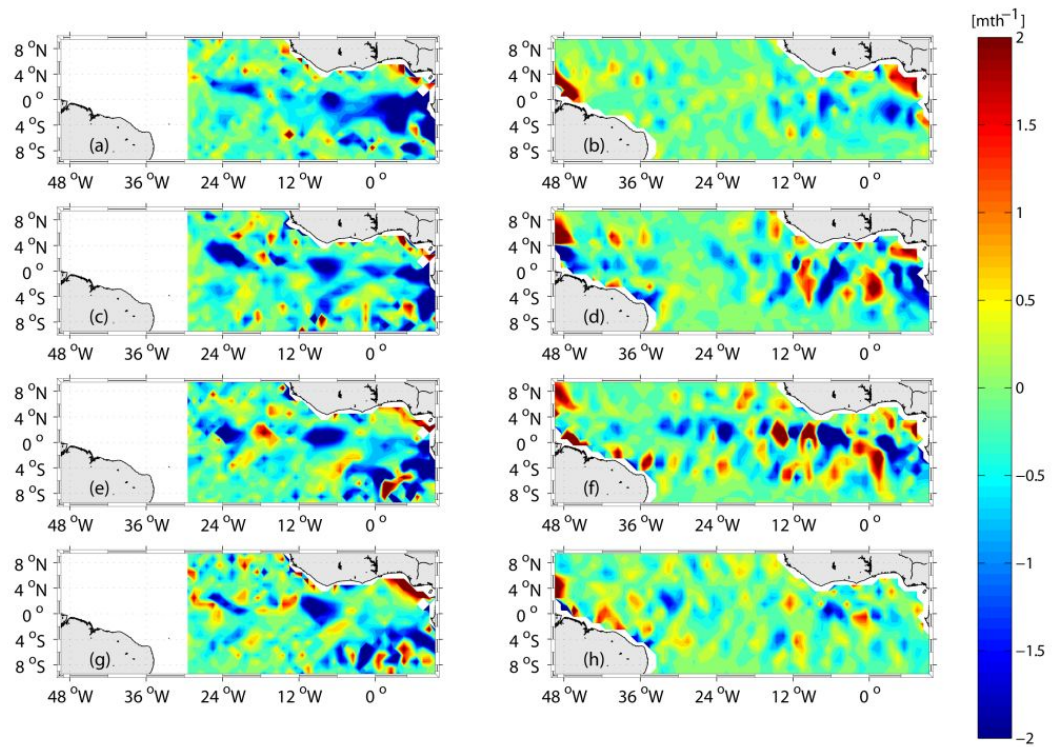


**Fig. 4.4:** Monthly mean zonal salinity advection from April (top row), May (second row), June (third row) and July (bottom row) 2011. Left Mercator model output, right SMOS/OSCAR.

lies with weak velocities and strong precipitation, was congruent to the wind field. The equatorial Atlantic was in April influenced by the ITCZ through precipitation (Fig. 4.5a). The zonal band of strong precipitation moved northward and in May the equator in the East Atlantic was rain-free (Fig. 4.5b). The core of the ITCZ, in May around 3°N, moved during the CTE northward to 8°N (Fig. 4.5c,d). The influence of precipitation for the ACT is expected to be small, while the northern region is at the beginning of the CTE directly below the ITCZ.

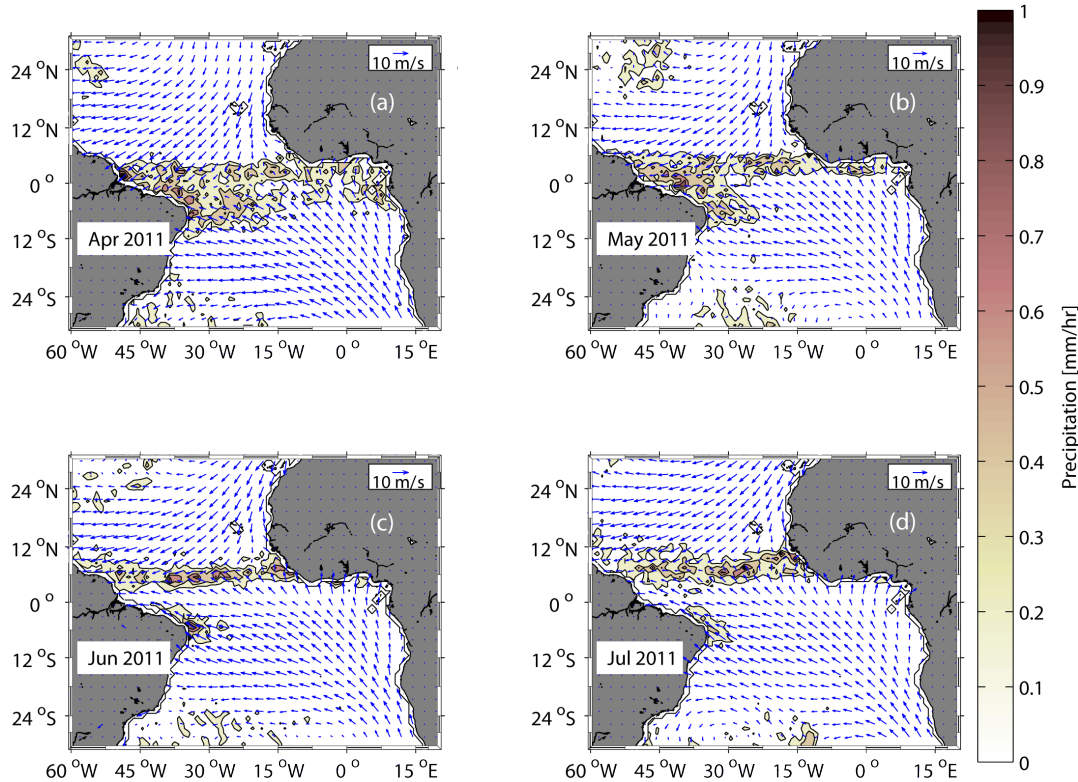


**Fig. 4.5:** Monthly mean surface winds and precipitation from April to July 2011. Shown are AMSRE precipitation and level 3.5 monthly analyzed winds from the CCMP Ocean Surface Wind product [Atlas *et al.*, 2011].

### 4.3 Vertical structure

Subsurface hydrographic changes during ACT development at 10°W were monitored with high spatial and temporal resolution using glider (Fig. 4.6) and moored temperature and salinity recorders. Surface cooling, as evident from the satellite SSTs, was also clearly evident from the glider observations (Fig. 4.6a). In addition the high vertical resolution

revealed the shoaling of the ML during the first month of observations (Fig. 4.6c).

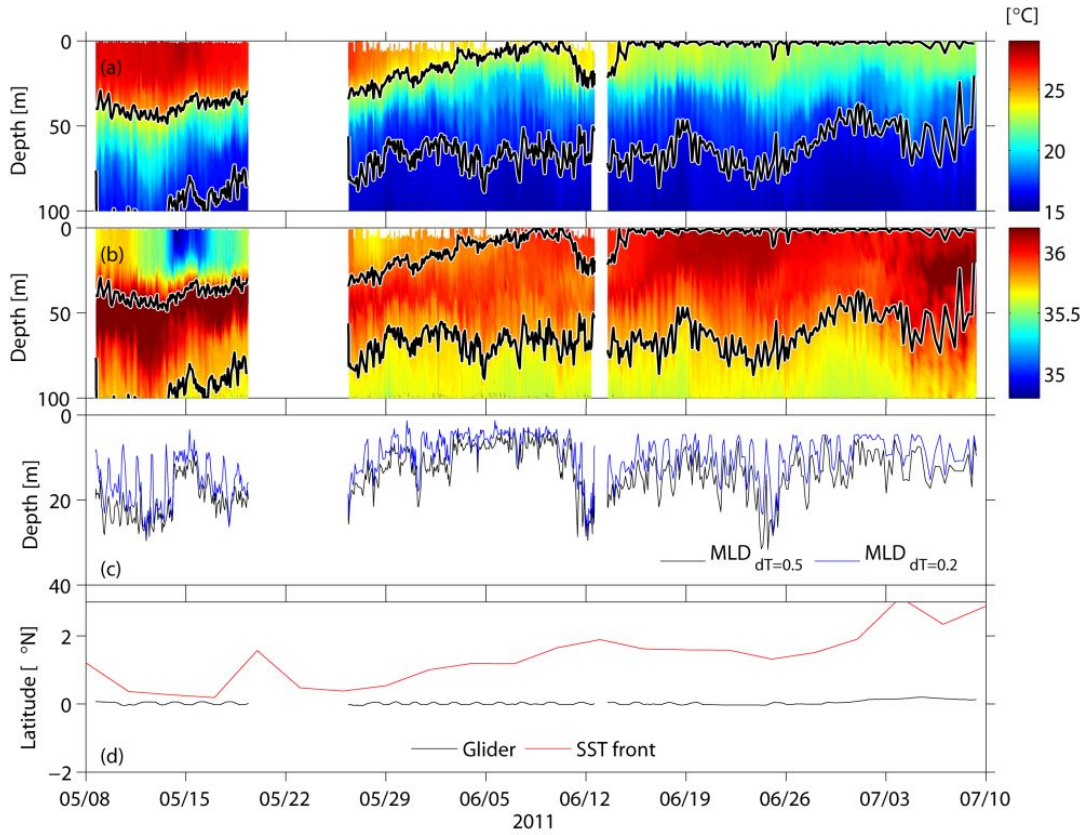


**Fig. 4.6:** Time series of glider ifm02 of temperature (a), salinity (b), MLD (c) and latitudinal position (black; d). In panel (d) the latitude of the SST front at 10°W is denoted in red. The glider profiled all the time close to the PIRATA buoy at 10°W.

The temporal evolution of the vertical salinity structure was more complex. At the beginning of the time series a pronounced salinity maximum existed below a rather fresh ML (Fig. 4.6b). The salinity maximum is related to the eastward transport of saline water from the western Atlantic within the EUC occurring during spring [Johns *et al.*, 2014; Kolodziejczyk *et al.*, 2014]. A strong increase in MLS was observed with the onset of the cold tongue, while the subsurface salinity maximum was reduced. The simplest explanation would be a vertical redistribution and mixing of salinity through exchange processes across the ML base. However, advective processes play the dominant role as will be shown below. MLS remained elevated during the further development of the cold tongue, whereas in the beginning of July the subsurface salinity maximum reappeared. Typically, MLDs are shallowest in tropical upwelling regions [e.g. de Boyer Montegut *et al.*, 2007]. Indeed, at the survey site, MLD never exceeded 30m, irrespective of the use of a tempera-

ture or density criterion (Fig. 4.6c). The abrupt increase in MLT and decrease in MLS on the 14th of May (Figs. 4.6a and b) was a remarkable event in the temperature and salinity time series, which counteracted the trends expected from the cold tongue development. Satellite SST distributions from this period suggested that the anomaly was caused by the propagation of a TIW that moved the SST front north of the ACT southward (Fig. 4.6d).

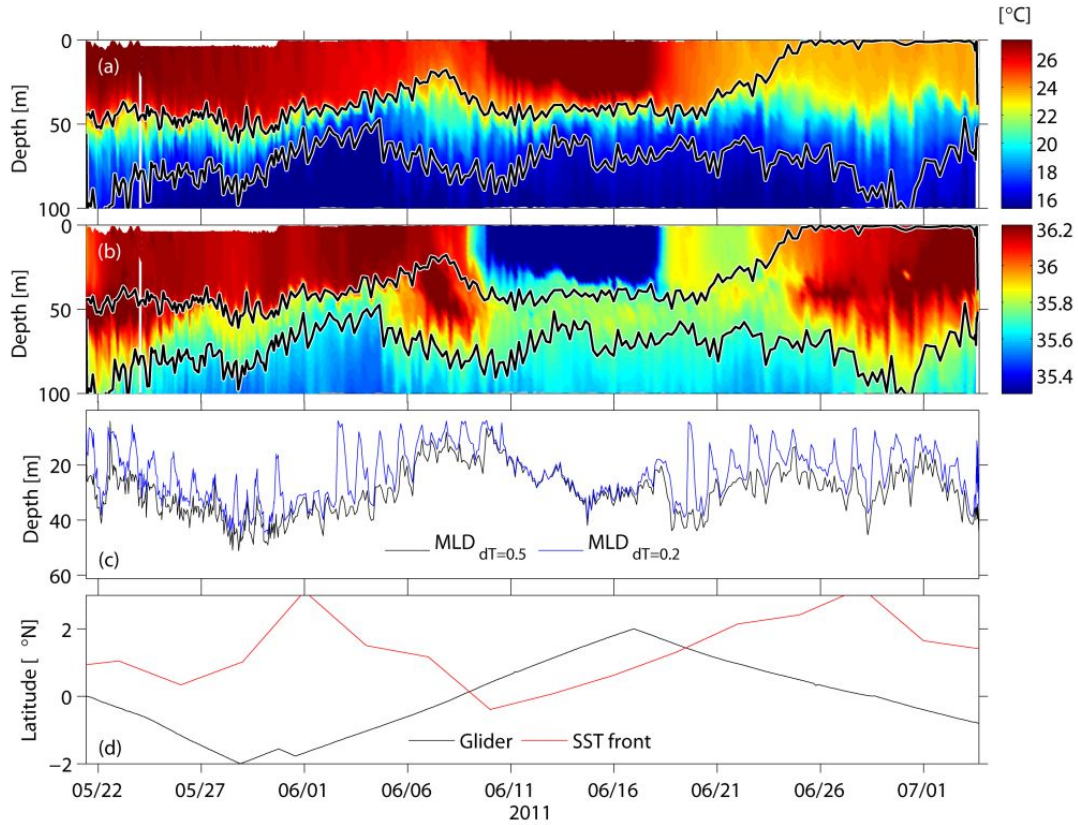


**Fig. 4.7:** Time series of glider ifm11 of temperature (a), salinity (b), MLD (c) and latitudinal position (black; d). In panel (d) the latitude of the SST front at 15.5 °W is denoted in red.

The surveys along meridional or zonal sections (Fig. 3.2) exhibit a mixture of temporal and spatial variability. One glider was assigned to profile along a meridional section at 15.5°W between 2°S and 2°N (Fig. 4.7d). The glider crossed the SST front around June 10th, stayed north of the front, and crossed back at June 18th (Fig. 4.7d). The crossing of the front was clearly visible in the freshening of the ML in association with increased temperatures (Figs. 4.7a and b). North of the front, a diurnal cycle in MLD (using a 0.2°C criterion) is not evident (Fig. 8c). The glider was close to the equator and crossed the EUC core and the subsurface salinity maximum at the beginning of the section, around the 10th of June, and at the end of June (Fig. 4.7b and d). North and south of the equator and away



from the EUC the subsurface salinity maximum was weak or not present.

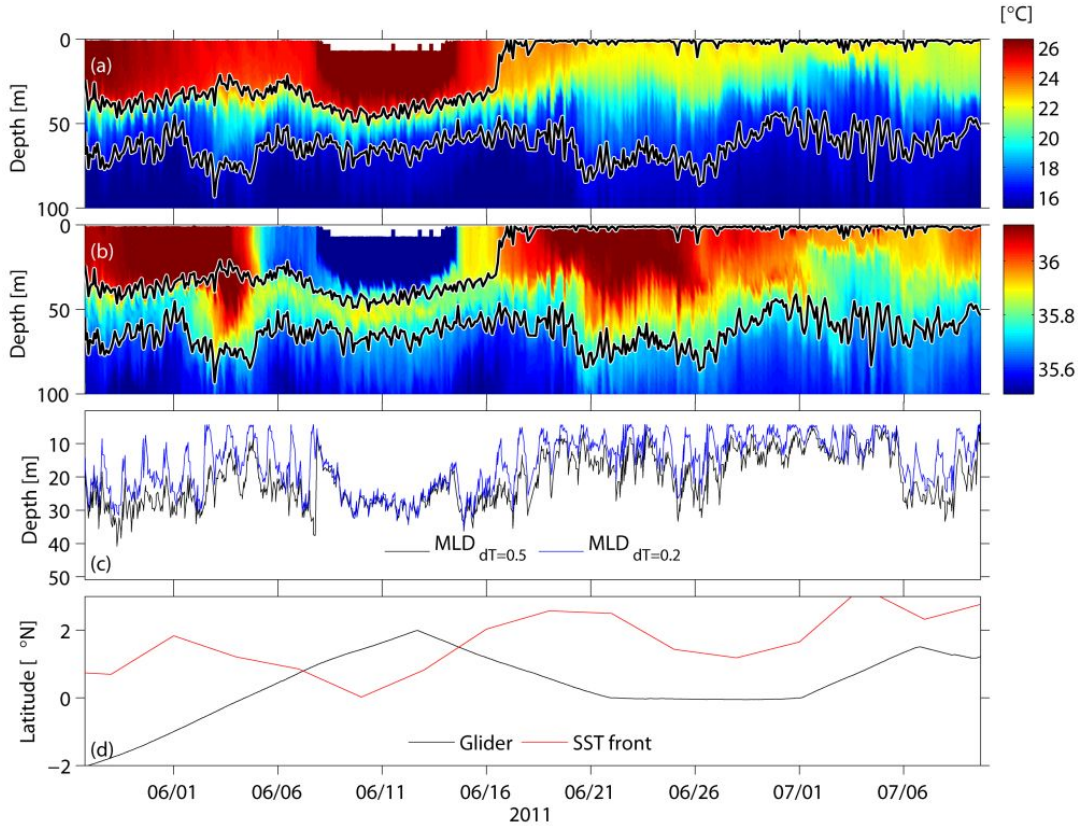


**Fig. 4.8:** Time series of glider ifm09 of temperature (a), salinity (b), MLD (c) and latitudinal position (black; d). In panel (d) the latitude of the SST front is denoted in red.

A combination of a meridional and a zonal section was conducted from glider ifm09 (Fig. 3.2). First, a meridional section was conducted between the end of May and the 22nd of June and between 13° and 13.5°W (Fig. 4.8). Afterwards the glider dived along the equator and changed the direction at around 10°W at the 1st of June to conduct a second short meridional section northward at 10°W. A crossing of the SST front, described before (Fig. 4.7), was observed again with this glider deployment.

Taking all glider, CTD, and Argo float profiles during the CTE into account the spatial structure of MLS and the evolution of the spatial structure can be examined (Fig. 4.9). The patchy structure, already identified with the satellite SSSs (Fig. 4.2), is clearly visible in the MLS field during the CTE as well. A region of high MLS at and south of the equator was surrounded by fresher regions in the north and in the south. At the beginning of the CTE only a few datapoints mostly from Argo floats and the french PIRATA cruise

showed the meridional structure in the central cold tongue region at around 10°W with a local maximum close to the equator (Fig. 4.9a). A westward zonal MLS gradient in the ACT end of May and the beginning of June can be identified with the several meridional sections at different longitudes (Figs. 4.9b-c). This structure was interrupted by local extrema, e.g. a local minimum mid of June close to the equator at around 15°W (Fig. 4.9d). At the end of the CTE the structure remained similar to the weeks before, indicating no significant changes end of June and in the beginning of July.

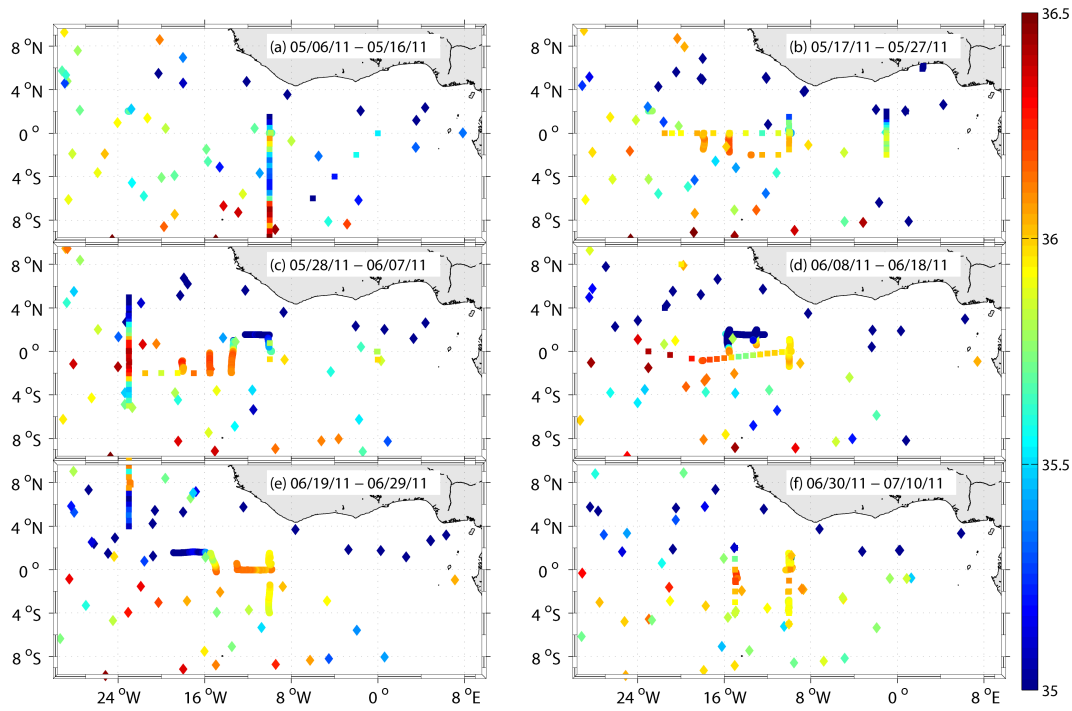


**Fig. 4.9:** MLS from glider profiles (circles), CTD profiles (squares), and Argo float profiles (diamonds) for the CTE. In this figure also data from the french cruise PIRATA-FR21<sup>1</sup> are included.

The vertical salinity maximum in the equatorial regions usually corresponds to the EUC. The upper thermocline layer (TL; defined with the potential density range:  $24.5 \leq \sigma_\theta \leq 26.2$ ) captures the EUC and the salinity maximum. However, the exact meridional position of salinity maximum and zonal velocity maximum is not equal. A meridional cross-equatorial section with CTD-casts and vmADCP observations of zonal velocity at 23°W (Fig. 4.10) shows that the salinity maximum is at the beginning of June (between 30th of May and 7th of June) south of the equator with the center around 1°S and in 50 m depth. During the same time the zonal velocity maximum is at around 0.75°S and at ap-

prox. 60 m depth. These observations confirm the observations by *Fahrbach et al.* [1986].

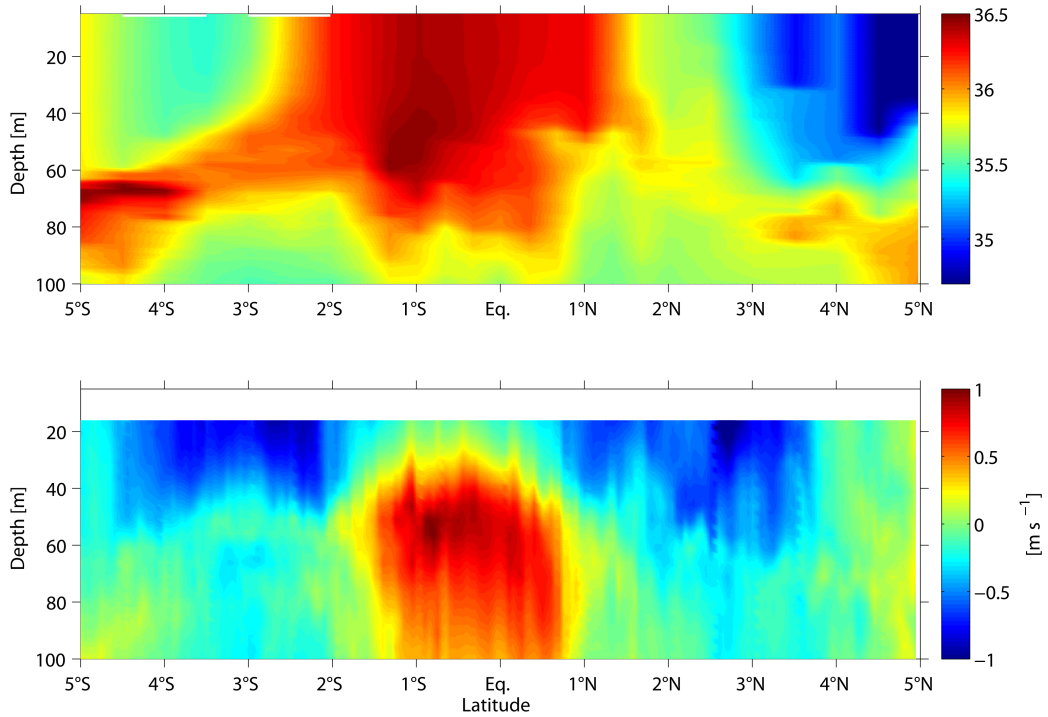


**Fig. 4.10:** Meridional section at 23°W of salinity (upper panel) and zonal velocity (lower panel).

A second meridional section, but southbound, at 10°W in May of CTD salinities and zonal vmADCP-velocities (Fig. 4.11) showed a similar structure than at 23°W, but the maxima were more moved to the equator. A subsurface salinity maximum at around 50 m depth nicely corresponds with the zonal velocity maximum at the same depth. Although these observations are earlier than the 23°W section described before, the depths of salinity maximum and EUC-core are shallower. This confirmed the eastward shoaling of the EUC.

The temporal evolution of the vertical salinity/velocity structure at 10°W can be nicely described by taking a second meridional section into account. This section (Fig. 4.12) was conducted later in the beginning of July. The vertical salinity structure at the equator has changed. At the surface were higher salinities observed than below at around 50 m, indicating a changed vertical salinity gradient. Additionally the core depth of the EUC became shallower and the maximum eastward velocities decreased.

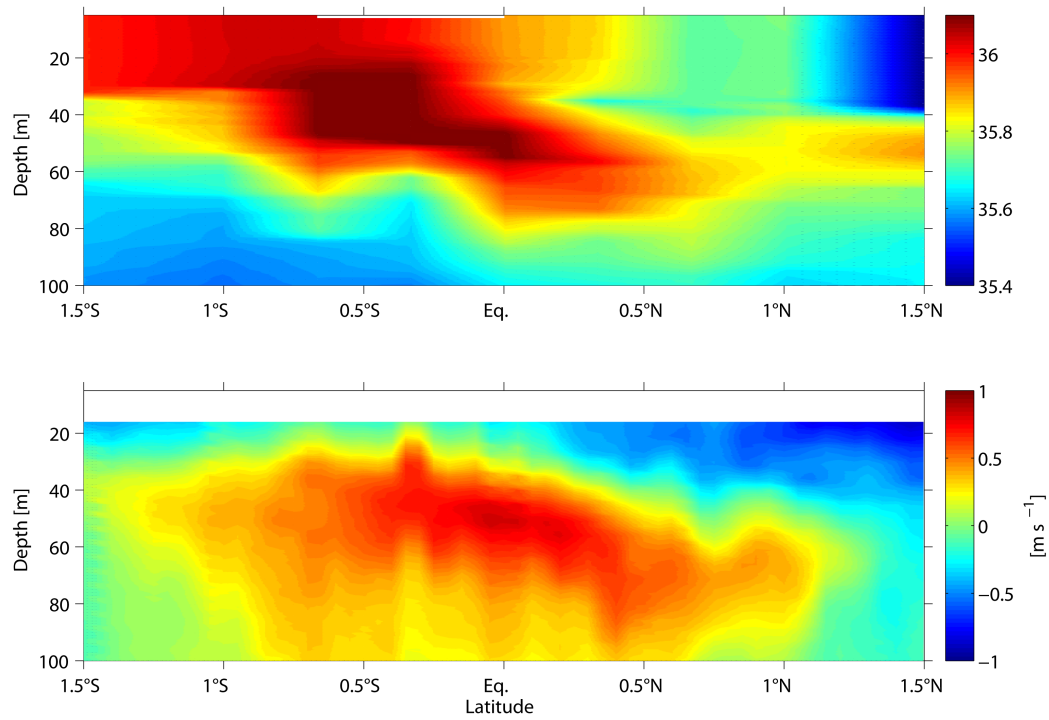


**Fig. 4.11:** Meridional section at 10°W of salinity (upper panel) and zonal velocity (lower panel) in May.



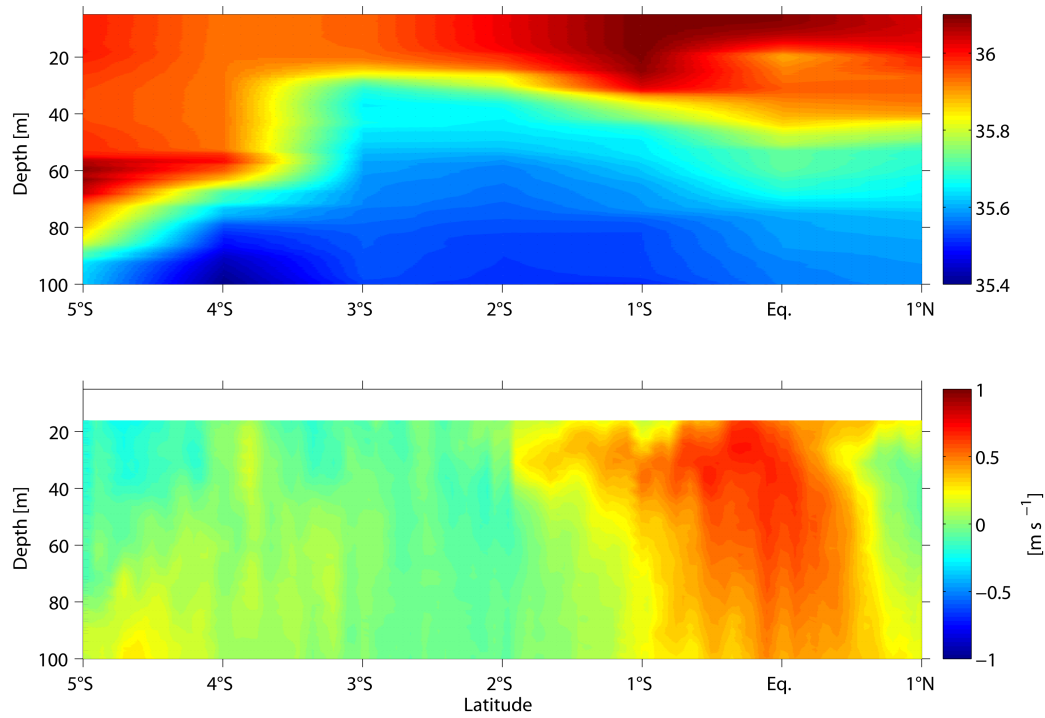


**Fig. 4.12:** Meridional section at  $10^{\circ}\text{W}$  of salinity (upper panel) and zonal velocity (lower panel) in July.

The spatial structure of the salinity maximum in the TL and the temporal evolution during the CTE showed a similar patchy structure as the mixed layer (Fig. 4.13). The meridional position of the salinity maximum is during the complete CTE at and slightly south of the equator. At the beginning of the CTE in May, high salinities were observed in the whole cold tongue region (Figs. 4.13a-b). Later in June and July the maximum in the central cold tongue around  $10^{\circ}\text{W}$  decreased to values lower than 36.2 (Figs. 4.13c-f). Together with the decrease around  $10^{\circ}\text{W}$  a narrower meridional spreading of salinities greater than 36.2 was observed.

The vertical salinity structure showed a change in the vertical salinity gradient (Fig. 4.14). At the beginning of the CTE in the entire ACT region the thermocline layer was saltier than the ML (Fig. 4.14a). During May and the beginning of June the ML was south of the equator in the ACT saltier than the TL (Figs. 4.14b-4.14d). This structure weakened later at the end of June and the beginning of July, when MLS and the EUC-salinity were almost equal in the ACT region (Figs. 4.14e and 4.14f). This time evolution of the difference between mixed layer and thermocline layer is independent of the measurement device and

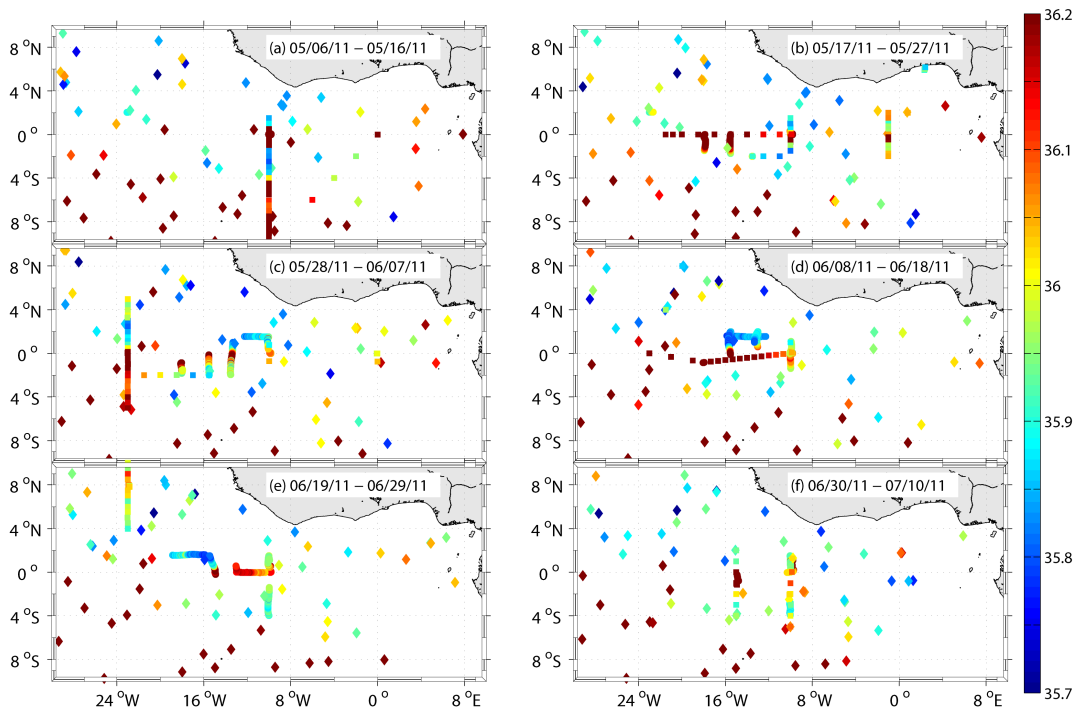


**Fig. 4.13:** Maximum salinity in the thermocline layer ( $24.5 \leq \sigma_\theta \leq 26.2$ ) from glider profiles (circles), CTD profiles (squares), and Argo float profiles (diamonds) for the CTE. In this figure also data from the french cruise PIRATA-FR21 are included.

visible in glider profiles as well as CTD and Argo float profiles. It also appears every, as evident from the monthly mean salinity difference from all Argo years averaged in a box with longitudinal boundaries  $23^{\circ}\text{W}$  and  $10^{\circ}\text{W}$  and latitudinal boundaries  $2^{\circ}\text{S}$  and  $1^{\circ}\text{N}$  (Fig. 4.14g).

## 4.4 Mixing conditions

The aforementioned vertical structure is the key criterion for vertical, or to be more accurately, diapycnal processes. Diapycnal turbulent fluxes of heat and salt are calculated with the turbulent diapycnal diffusivity and the vertical temperature gradient below the ML base (cf. equ. 3.6) or the vertical salinity gradient below the ML base (cf. equ. 3.7). The turbulent diapycnal diffusivity of mass is estimated from the turbulent dissipation rates. These are calculated from the vertical shear of horizontal velocities.

Profile-wise dissipation rates and turbulent diapycnal diffusivities, respectively averaged below the ML base, are shown in Fig. 4.15 for the two periods (period one: 17 May to 5 June; period two: 8 June to 9 July), described above (sect. 3.5.2). The dissipation rates for TKE high during the entire CTE in the cold tongue region, indicating strong vertical shear of horizontal velocities. Using these estimates of dissipation and taking the stratification into account, the horizontal distribution of the vertically averaged diapycnal diffusivities indicates local maxima along the equator and south of it in the central cold tongue region (Fig. 4.15b and d). However, the spatial variability between distinct profiles is high.

The horizontal distribution of the vertical temperature gradient shows, as expected, a positive temperature gradient with height (note that height is decreasing while depth is increasing) (Figs. 4.16a and c). Generally, the gradients larger during the first averaging period when warm surface waters are above the colder subsurface waters below the ML. Later, during strong cooling, the surface is colder resulting in a weaker vertical temperature gradient.

The vertical salinity increased with depth (negative values) along the equator during the first period. Salty subsurface waters, associated with the EUC, are below fresher surface waters. Interestingly at  $23^{\circ}\text{W}$  between  $0.5^{\circ}\text{S}$ - $1^{\circ}\text{N}$  higher surface are salinities are ob-

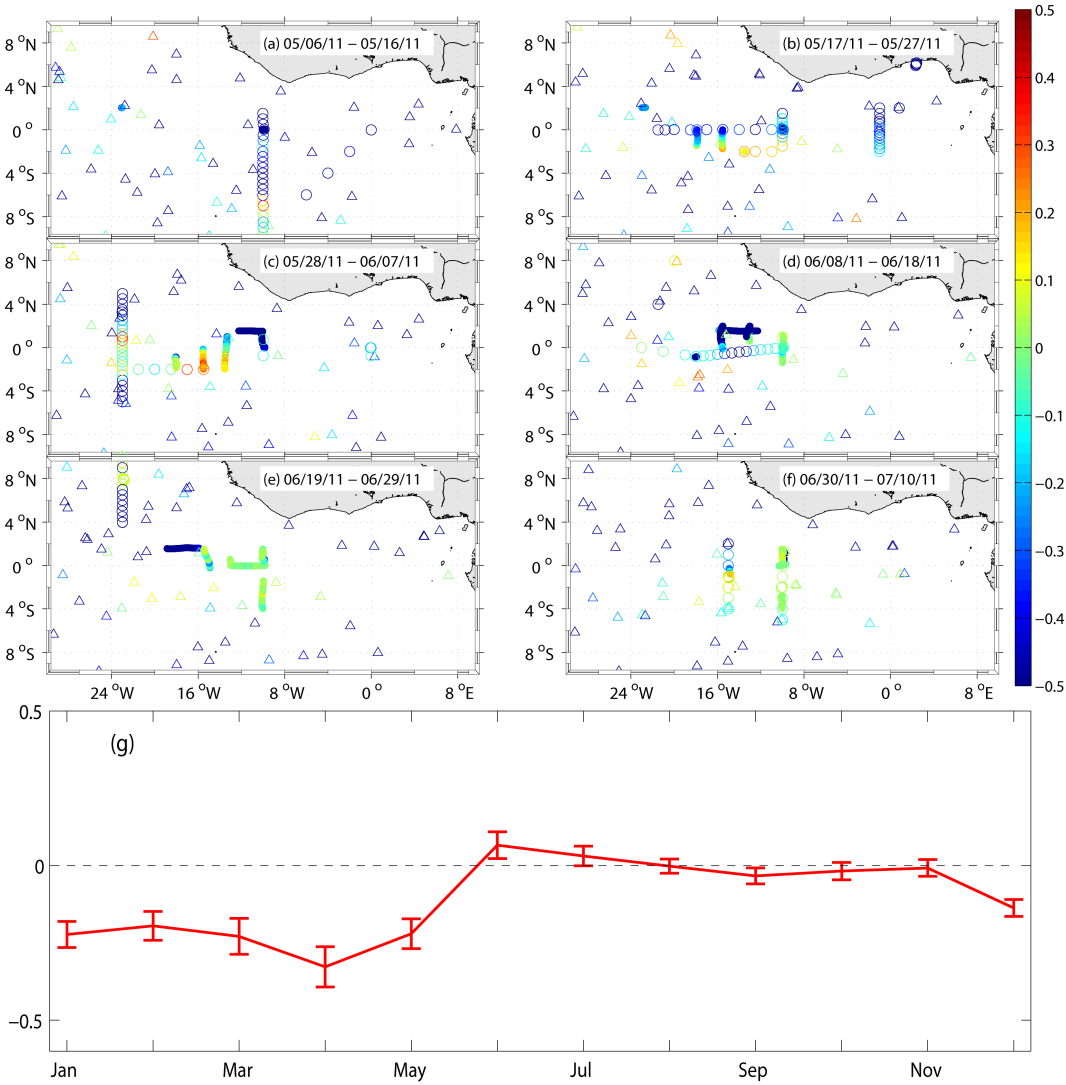


**Fig. 4.14:** (a-f) Salinity difference between MLS and maximum salinity in the upper thermocline layer below the ML ( $24.5 \leq \sigma_\theta \leq 26.2$  or  $\sigma_{MLD} \leq \sigma_\theta \leq 26.2$  if  $\sigma_{MLD} \geq 24.5$ ) from glider profiles (circles), CTD profiles (squares), and Argo float profiles (diamonds) for the CTE. In this figure also data from the french cruise PIRATA-FR21 are included. (g) Mean salinity difference between MLS and maximum salinity in the upper thermocline layer ( $24.5 \leq \sigma_\theta \leq 26.2$ ) from all Argo float profiles from the years 2000-2012 in boxes with the longitudinal boundaries  $23^\circ\text{W}$  and  $10^\circ\text{W}$  and the latitudinal boundaries  $2^\circ\text{S}$  and  $1^\circ\text{N}$ .

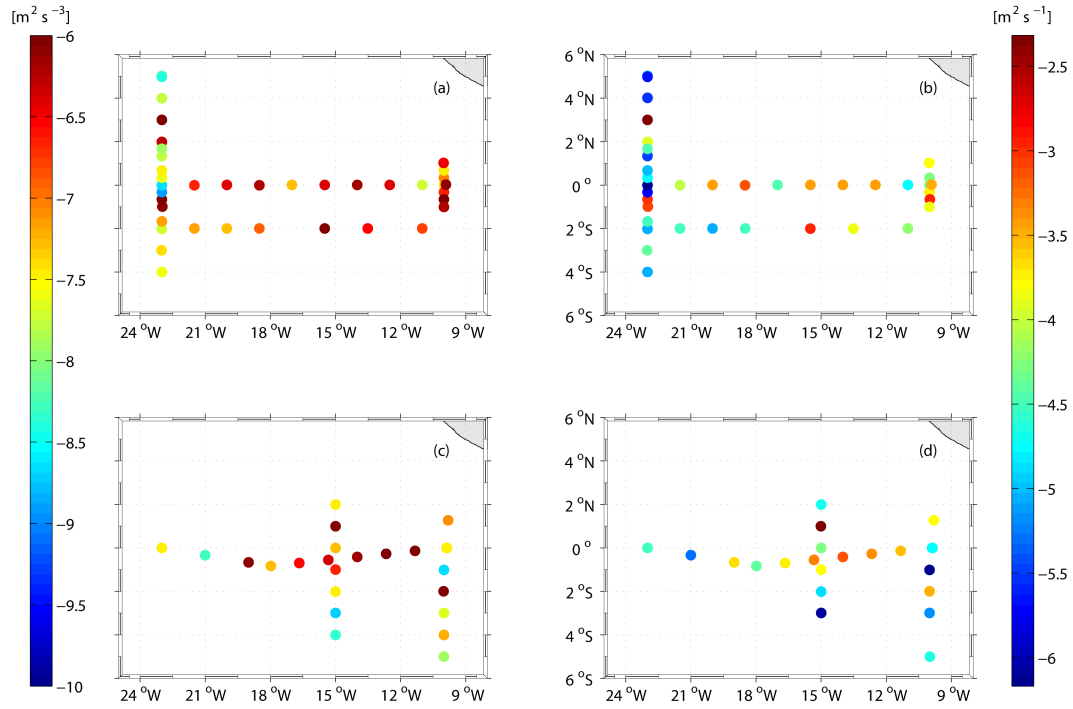


**Fig. 4.15:** Dissipation rates (a and c) and diapycnal diffusivities (b and d) averaged below the ML base for period one (17 May to 5 June; a and b) and for period two (8 June to 9 July; c and d)

served (Fig. 4.16b). These observations are from the beginning of July, when the vertical salinity gradient as well as the jump between the ML and the TL changed sign (cf. Fig. 4.14c). This feature is later also seen south of the equator at 15°W and at and south of the equator at 10°W (Fig. 4.16d)).

The combination of diapycnal diffusivities and vertical temperature and salinity gradients allowed the estimation of diapycnal fluxes of heat and salt, respectively, below the ML. The diapycnal heat flux is downward, i.e. out of the ML, during the whole CTE (Figs. 4.17a and c). The spatial distribution indicated maximum diapycnal heat fluxes at and slightly south of the equator. These fluxes were negative during the entire CTE period (Figs. 4.17a and c), which meant a diapycnal heat flux out of the ML down into the thermocline over the ML base.

A different story tell the pictures from the diapycnal salt flux at the ML base. During the first period until the beginning of June mostly positive diapycnal salt fluxes were estimated along the equator (Fig. 4.17b). This indicated a salt gain for the ML at these sites through the diapycnal salt flux. At a few positions around the equator at 10°W and

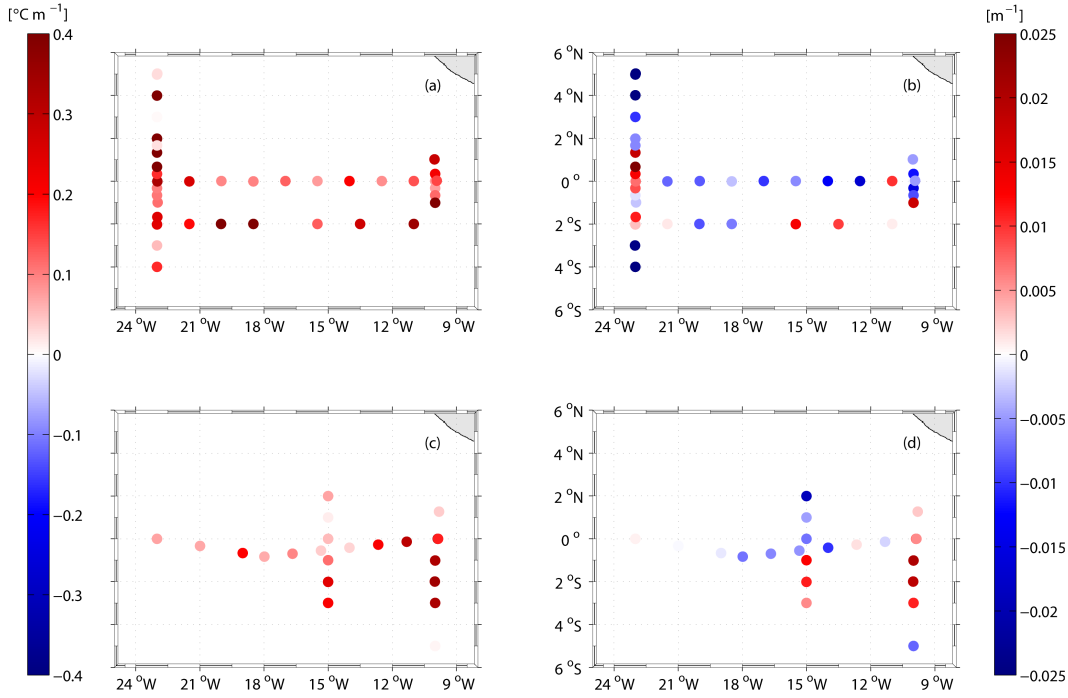


**Fig. 4.16:** Vertical temperature (a and c) and vertical salinity gradient (b and d) averaged below the ML base for period one (17 May to 5 June; a and b) and for period two (8 June to 9 July; c and d)

at 2°S negative diapycnal salt fluxes were observed. Here, the vertical salinity gradient was negative with pressure (positive with height) (cf. fig. 4.16b). This patchy structure remained during the second mixing period (Fig. 4.17d) with freshwater gain through diapycnal mixing at 10°W and 2°S and salt gain elsewhere. The region of freshwater gain at the equator grew westward to around 13°W.

## 4.5 Summary

The ACT in boreal spring/summer in 2011 was partly different compared to earlier years and the mean cold tongue evolution. In the central cold tongue region an anomalous early onset lead to a an early temperature drop end of April/ beginning of May. The early onset was also evident from a large salinity increase during the same time period. The center of the cold tongue was identified at 10°W at the equator, evident from satellite observations as well as assimilation model results. The complex salinity structure is well reflected in zonal salinity advection. While the model output indicated mostly large-scale westward

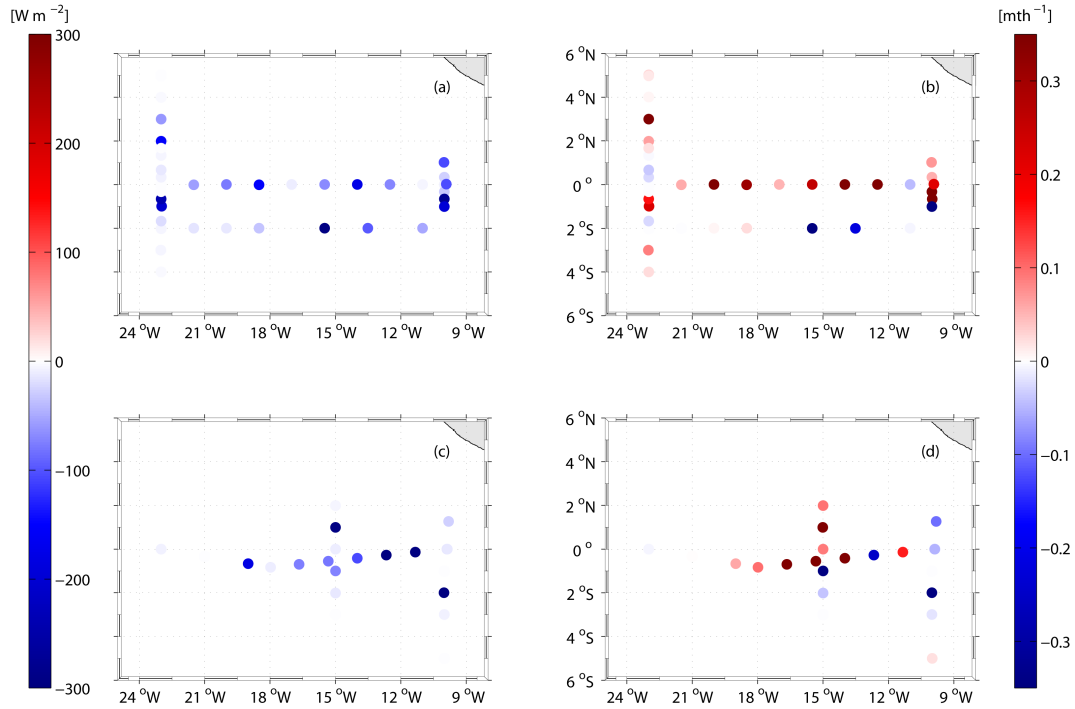


**Fig. 4.17:** Diapycnal heat flux (a and c) and diapycnal salt flux (b and d) averaged below the ML base for period one (17 May to 5 June; a and b) and for period two (8 June to 9 July; c and d)

freshwater advection in the cold tongue region, this pattern is disrupted in the satellite estimates. Here, areas with large westward salinity advection occurred. At and south of the equator the wind influence increased due to increasing windspeeds, while the impact of precipitation became negligible in the cold tongue region during the CTE and was only remarkable north of the cold tongue.

The glider sections showed the general development of the cold tongue at the surface and in the ML with decreasing temperatures and increasing salinities. Together with shallow MLs the glider sections also showed the local changes of the vertical salinity gradients, which lead to a freshwater gain for the ML due to entrainment and diapycnal mixing. This happened only locally at and south of the equator at 10°W. All other equatorial positions showed a subsurface maximum of salinity which is associated with the EUC. The change in vertical salinity gradient is mostly observed southward of the equator to 2°S. Here during the CTE several individual and independent observations showed this structure, in particular in the beginning of June. Float observations from all Argo years confirm this development to be an annual phenomenon. High dissipation rates of TKE and therefore high diapycnal diffusivities lead to locally large diapycnal heat and salt fluxes at and south

of the equator and the changed vertical temperature gradient lead to inverse salt fluxes as well. However, the spatially averaged diapycnal salt flux at the ML base was weak.



# 5 Mixed layer heat and salinity budget during ACT onset in 2011

## 5.1 Introduction

In this study an extensive in-situ dataset is used to investigate the ML heat and salinity budget concurrently. Hydrographic, together with microstructure observations, and atmospheric data collected during two expeditions on R/V Maria S. Merian in spring/summer 2011 have been combined with simultaneous high resolution temperature and salinity data from a glider swarm experiment. During this glider swarm experiment six gliders measured hydrographic properties between  $2^{\circ}\text{S}$  and  $2^{\circ}\text{N}$  (one glider track was extended to  $4^{\circ}\text{S}$ ) and between  $23^{\circ}\text{W}$  and  $10^{\circ}\text{W}$ . In the following we refer to the observational experiment as the “Cold Tongue Experiment” (CTE). The CTE data set is further augmented by in-situ data provided from Argo profile data and by time series data from PIRATA buoys and subsurface moorings. The combined extensive in-situ data set is the basis to quantify all terms contributing to the ML heat and salt budgets during the observational period. This enables us to identify the processes responsible for the SST and SSS variability typically observed for this entire region. Due to the amount of ship time required to obtain such an extensive in-situ data set, the CTE covers two months of the year 2011. The CTE was scheduled between May and July to focus on the processes responsible for the variability of SST and SSS during the ACT development.

The temporally and spatially averaged quantities MLD, MLS and MLT are shown in figure 5.1. The mixed layer during boreal summer is shallow in the equatorial regions. In 2011 the ML was at the beginning of the CTE around 20 m and became shallower throughout the following two months (Fig. 5.1a). While the MLS slightly increased from 35.5 to

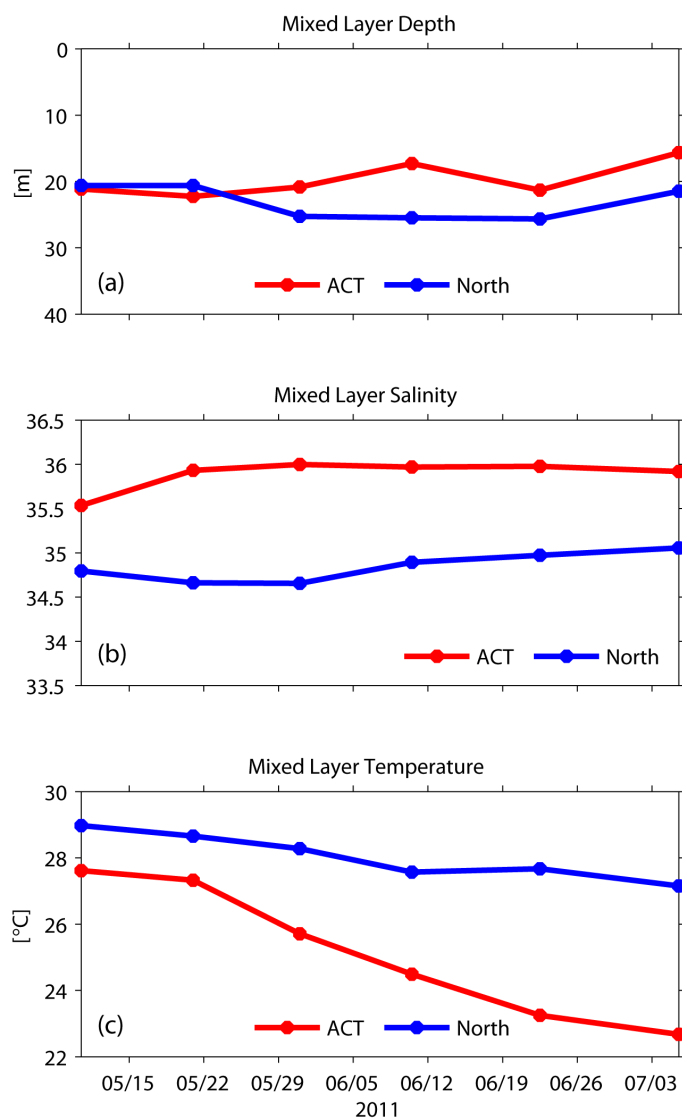


**Fig. 5.1:** MLD (a), MLS (b), and MLT (c) for the ACT box and for the northern box.

almost 36.0 (Fig. 5.1b) during the CTE, the MLT cooled from  $\sim 28^\circ\text{C}$  to less than  $23^\circ\text{C}$  (Fig. 5.1c). The development of these box-averaged quantities is quite similar to the surface observations at the PIRATA buoys at the western and eastern edge of the ACT box (Fig. 4.1).

The northern box (cf. fig. 3.1) became thicker during the CTE and shallower at the end of the CTE. The net change in MLD in the northern box was nearly zero (Fig. 5.1a). The MLS was fresher all the time, compared to the ACT region, reflecting the precipitation impact in this region. However, in total the MLS increased slightly during the CTE from  $\sim 34.8$  to  $35.0$  (Fig. 5.1b). A cooling was also identified in the northern region (Fig. 5.1c), but much weaker compared to the ACT region. The ML cooled from  $\sim 29^\circ\text{C}$  to  $\sim 27^\circ\text{C}$ . These changes in MLS and MLT are caused by several processes. In this chapter the contribution of changes of the ML heat and salinity content are explained.

## 5.2 Heat budgets during ACT onset

### 5.2.1 ACT box

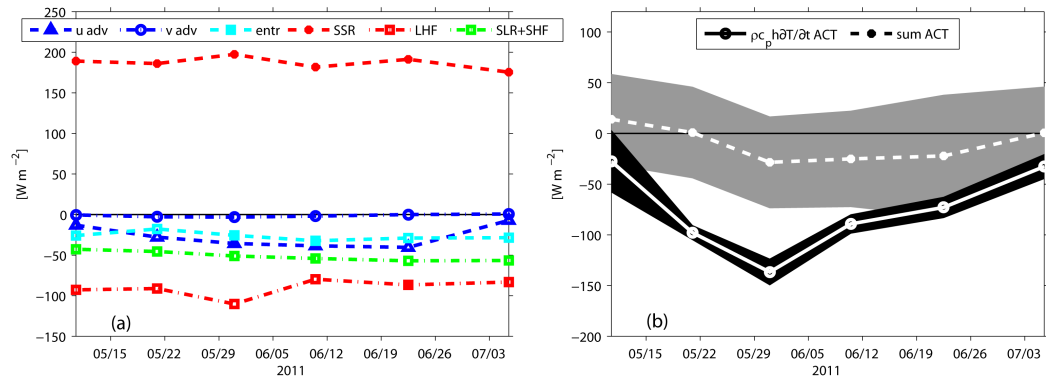


**Fig. 5.2:** The contribution of each term to the ML heat budget (a) and the local heat storage and the sum of the terms (b) for the ACT box.

The contributions of the different processes (Equation 3.1) to the ML heat budget in the ACT box are described in the following. Absorbed shortwave radiation ranged between  $175 \pm 36$  to  $197 \pm 36 \text{ W m}^{-2}$ . The variability is explained by the variability of cloud cover and the thickness of the ML. The latent and sensible heat fluxes as well as the net surface longwave radiation cooled the ML throughout the CTE (Fig. 5.2a). The net surface

longwave radiation in the ACT box was nearly constant ( $41 \pm 10$  to  $56 \pm 10 \text{ W m}^{-2}$ ) during the CTE due to the balance of outgoing and downward longwave radiation. Outgoing longwave radiation slightly weakened with decreasing SSTs and the downward longwave radiation weakened with the reduction of clouds. The latent heat flux ranged between a maximum of  $110 \pm 21 \text{ W m}^{-2}$  and a minimum of  $80 \pm 21 \text{ W m}^{-2}$ . The variability was predominantly associated with varying winds. The magnitude of the sensible heat flux from the ocean to the atmosphere was the smallest compared to the aforementioned heat fluxes with a mean of  $2 \pm 3 \text{ W m}^{-2}$ . The resulting net surface heat flux warmed the ML during the whole CTE with a mean of  $45 \pm 43 \text{ W m}^{-2}$ .

The strong heat loss of the ACT ML in boreal summer can only be explained by ocean dynamics. Zonal heat advection played an increasing role for ML cooling until the end of June with strongest cooling of  $-41 \pm 42 \text{ W m}^{-2}$ , while meridional heat advection was a minor contributor to cooling with a maximum of  $-3 \pm 6 \text{ W m}^{-2}$ . Similar results were obtained for the Mercator model, where meridional heat advection showed a maximum contribution of  $-12 \pm 1 \text{ W m}^{-2}$ . Entrainment consistently cooled the ML with rates between  $-32 \pm 2$  and  $-18 \pm 1 \text{ W m}^{-2}$  resulting from high vertical velocities in combination with a positive vertical temperature difference between the ML and the water below.

In accordance with the reduced SST, the ML heat content tendency in the ACT box was negative during the entire CTE period (Fig. 5.2b). The tendency was weakly negative during early May, but strongly negative during the period end of May to early June, when the ML locally lost up to  $-137 \pm 13 \text{ W m}^{-2}$  of heat. Without considering the diapycnal heat flux (Fig. 5.2b), the mixed layer heat tendency cannot be explained by the sum of processes described above.

The diapycnal heat flux determined from the microstructure data was elevated during the first period of the CTE from the second half of May to the beginning of June. For this period, a mean flux of  $-111 \pm 16 \text{ W m}^{-2}$  was estimated that reduced in magnitude to  $-49 \pm 9 \text{ W m}^{-2}$  during the second half of the CTE (Fig. 5.3a). Unfortunately, microstructure observations were not continuously available for the entire CTE period within the ACT box thus longer averaging periods had to be used to estimate representative diapycnal heat flux contributions. The elevated heat flux during the first period of the CTE resulted from elevated turbulent eddy diffusivities that persisted despite increased upper-ocean stratification during this period.

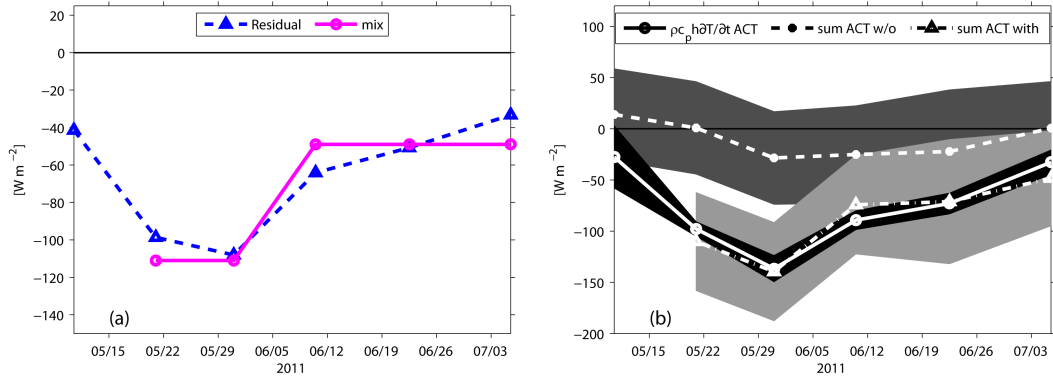


**Fig. 5.3:** The residual of the ML heat budget and the diapycnal heat flux (a) and the local heat storage and the sum of the terms with and without the diapycnal heat flux (b) for the ACT box.

The magnitude and temporal variability of the sum of the individual heat flux contributions including the diapycnal heat flux (Fig. 5.3b) agrees strikingly well with magnitude and temporal variability of the heat content tendency. This indicates that within the uncertainties, the heat budget in the ACT region was closed utilizing the above flux estimates for the sampled period. A discussion of unresolved processes as well as uncertainties is presented in section 5.4 below.

### 5.2.2 Northern box

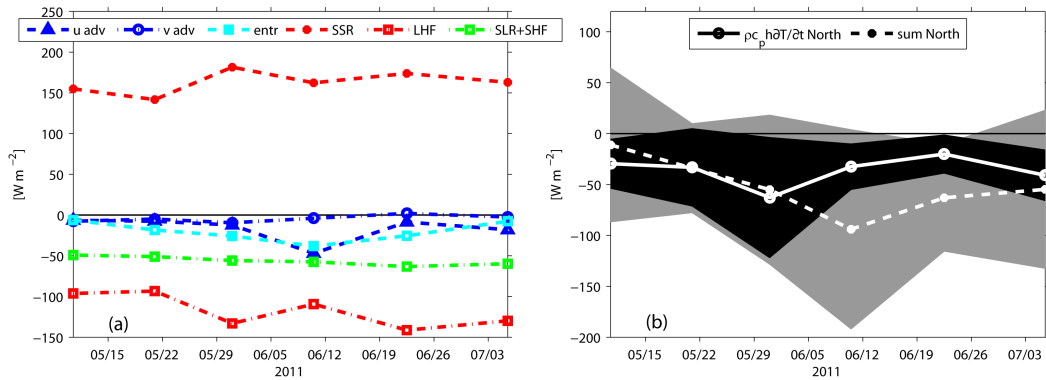


**Fig. 5.4:** The contribution of each term to the ML heat budget (a) and the local heat storage and the sum of the terms (b) for the northern box.

The dominant processes contributing to the heat balance of the northern box differ from those dominating the ACT heat balance. In particular, the net surface heat flux was compa-

rably lower and even changed sign during the CTE. Absorbed shortwave radiation ranged between  $142 \pm 35$  and  $182 \pm 35 \text{ W m}^{-2}$  and was mainly balanced by the heat loss due to the other atmospheric fluxes (sum ranging between  $-142 \pm 24$  and  $-205 \pm 24 \text{ W m}^{-2}$ ) (Fig. 5.4a). However, the net surface heat flux warmed the ML in the beginning of the CTE with  $9 \pm 42 \text{ W m}^{-2}$ , while it cooled the ML during the rest of the experiment with a minimum of  $-31 \pm 42 \text{ W m}^{-2}$  at the end of the CTE. This was mainly caused by the increased cooling contribution of the latent heat flux due to the increased wind.

Zonal heat advection significantly contributed to cooling of the ML only during the beginning of June ( $-47 \pm 62 \text{ W m}^{-2}$ ), but was small during the rest of the CTE period. The contribution of meridional heat advection to ML cooling in the northern box was  $-9 \pm 57 \text{ W m}^{-2}$  at its maximum. The high uncertainties for the advection terms result, on the one hand, from the velocity error, estimated through comparison of OSCAR with direct moored velocity measurements and, on the other hand, from uncertainties of estimating the horizontal temperature gradients from the satellite data. The contribution of entrainment ranged from  $-6 \pm 2 \text{ W m}^{-2}$  to  $-38 \pm 2 \text{ W m}^{-2}$  during the whole CTE and is particularly important for ML cooling in June.

The ML heat content tendency was negative throughout the CTE (Fig. 5.4b). The negative tendency was largest at the end of May/beginning of June ( $-63 \pm 59 \text{ W m}^{-2}$ ) while it was smallest ( $-20 \pm 19 \text{ W m}^{-2}$ ) during mid-June. During the whole CTE period and within the given uncertainties, the sum of the aforementioned individual flux terms balances the ML heat content tendency.

## 5.3 Salinity budgets during ACT onset

### 5.3.1 ACT box

The contribution of the different processes given by Eq. 3.2 to ML salinity budget in the ACT box is described here. Evaporation increased MLS constantly at a rate of ranging between  $0.15 \pm 0.04$  and  $0.21 \pm 0.04$  per month ( $\text{mth}^{-1}$ ), while precipitation reduced the MLS only in the beginning of May. The contribution of precipitation to MLS changes during the development of the ACT was negligible, due to the further northward migra-

tion of the ITCZ (Fig. 5.5a).

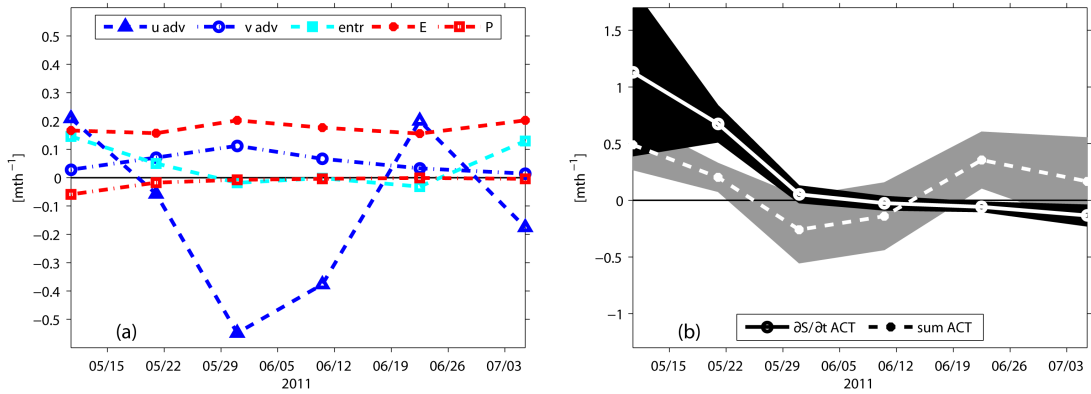


**Fig. 5.5:** The contribution of each term to the ML salinity budget (a) and the local salinity tendency and the sum of the terms (b) for the ACT box.

The contribution of the different processes given by equation 3.2 to the ML salinity budget in the ACT box is described here. Evaporation increased MLS constantly at a rate between  $0.16 \pm 0.04$  and  $0.20 \pm 0.05$  per month ( $\text{mth}^{-1}$ ), while precipitation reduced the MLS only weakly in the beginning of May (Fig. 5.5a). The contribution of precipitation to MLS changes during the development of the ACT was negligible, due to the position of the ITCZ further to the north (Fig. 5.5a). Hence the difference  $E-P$  is at this location dominated by evaporation.

By far, the main contributor to the ML salinity budget was zonal advection. In May and the beginning of June 2011 freshwater was advected into the ACT within the westward branches of the South Equatorial Current (SEC). Maximum advection occurred in late May contributing to a freshening of  $-0.55 \pm 0.21$   $\text{mth}^{-1}$ . However, zonal advection exhibited elevated variability throughout the experiment and even changed sign in the middle of June when it contributed to a salinity increase of  $0.20 \pm 0.21$   $\text{mth}^{-1}$ . This contribution will be examined in detail below.

Meridional salinity advection increased MLS in May and the beginning of June 2011, when peak fluxes of  $0.11 \pm 0.20$   $\text{mth}^{-1}$  were determined (Fig. 5.5a). During the rest of the CTE, the contribution of meridional advection was weak. Entrainment also played a minor role for salinity changes in the ML during the experiment except in the beginning and the end of the CTE when values of  $0.15 \pm 0.03$   $\text{mth}^{-1}$  were reached. As vertical ve-

locities used for the entrainment estimates in the salinity and the heat budget are the same, the reduced role of entrainment for the salinity budget is due to the small vertical salinity gradients as pointed out in chapter 4.

The MLS in the ACT box increased with the cold tongue onset in May 2011, with a maximum tendency of  $1.13 \pm 0.74 \text{ mth}^{-1}$  (Fig. 5.5b). This tendency reduced during the further expansion of the cold tongue and was followed by a period of weak freshening of the ML. With the data sets available for this study, the salinity content change during cold tongue development could not be fully balanced by the individual flux contributions when neglecting the diapycnal salt flux.

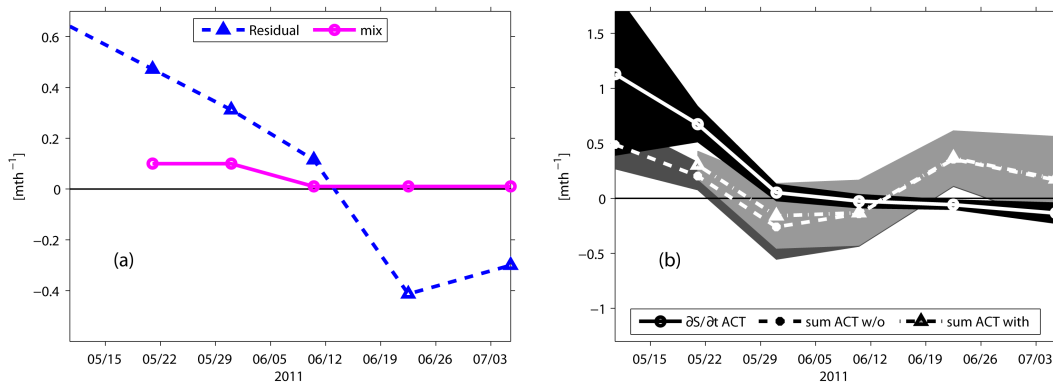


**Fig. 5.6:** The residual of the ML salinity budget and the diapycnal salt flux (a) and the local salinity tendency and the sum of the terms with and without the diapycnal salt flux (b) for the ACT box.

The diapycnal salt flux inferred from microstructure observations increased ML salinity by  $0.10 \pm 0.01 \text{ mth}^{-1}$  during the end of May/beginning of June (Fig. 5.6a). It decreased in June and locally partly changed sign in the end of June/beginning of July around  $10^\circ\text{W}$ , according to a local change in sign of the vertical salinity gradient (Fig. 4.6b). However, the average diapycnal flux determined from all data collected between the second week of June and the end of the experiment resulted in a very weak flux of  $0.01 \pm 0.01 \text{ mth}^{-1}$  (Fig. 5.6a).

As already described above (cf. fig. 5.5b) the salinity content change during cold tongue development, with the data sets available for this study, could not be fully balanced by the individual flux contributions, although contributions of the diapycnal salt flux were eval-



uated as well (Fig. 5.6b). The latter accounted for some of the salinity content increase observed during the beginning of the experiment, but an unresolved residual remained which is further discussed in section 5.4.

### 5.3.2 Northern box

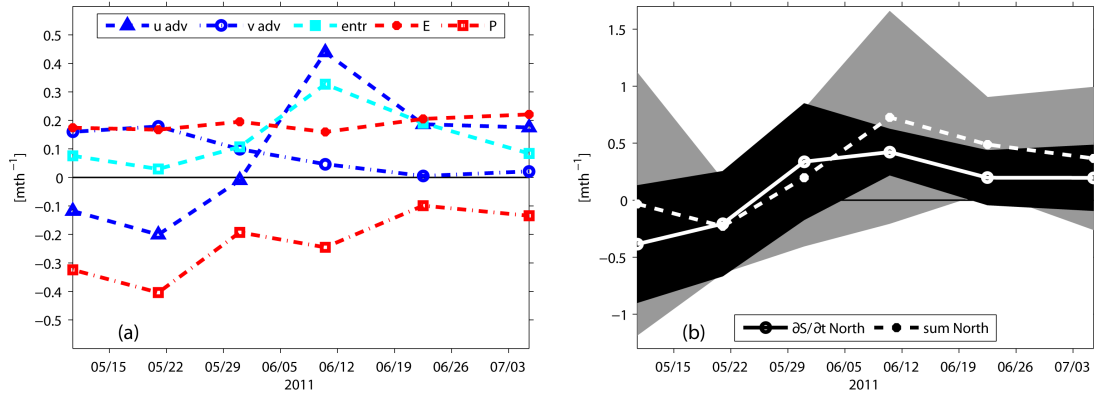


**Fig. 5.7:** The contribution of each term to the ML salinity budget (a) and the local salinity tendency and the sum of the terms (b) for the northern box.

Evaporation in the northern box was similar to the evaporation in the ACT box and weakly increasing during the CTE from  $0.16 \pm 0.03$  to  $0.22 \pm 0.06 \text{ mth}^{-1}$ . In analogy to the latent heat flux, this increase was caused by the increasing wind speed. The main source of freshwater in the northern box during the CTE was precipitation (Fig. 5.7a). The ITCZ occupied parts of the northern box during the CTE, which lead to an elevated freshwater input of predominantly convective rainfall resulting in a maximum salinity decrease of  $-0.40 \pm 0.04 \text{ mth}^{-1}$  in the middle of May. Hence, the difference  $E-P$  was negative during most parts of the CTE and only changed sign in the second half of June.

Again, zonal advection played a key role in salinity changes for the northern box (Fig. 5.7a). During May, westward velocities advected freshwater into the northern box from the east leading to a flux of up to  $-0.20 \pm 0.17 \text{ mth}^{-1}$ . Later in June, elevated zonal salinity advection of  $0.44 \pm 0.57 \text{ mth}^{-1}$  contributed to the MLS increase. Meridional salinity advection was a dominant contributor to the MLS increase during May. Northward velocities advected salty water from the cold tongue into the northern box with a maximum contribution of  $0.18 \pm 0.37 \text{ mth}^{-1}$ . Entrainment derived from model output was weak during the beginning of the CTE, but increased to a maximum contribution of  $0.33 \pm 0.02$

$\text{mth}^{-1}$  in mid-June, and decreased afterwards.

In the northern box, MLS tendency was positive during the whole CTE except for a strong freshening during the beginning of the experiment (Fig. 5.7b). The MLS tendency was balanced within the uncertainties by the sum of precipitation, evaporation, lateral advection, and entrainment during most of the CTE period.

## 5.4 Residual

The above results showed that within the uncertainties of the individual flux contributions and the uncertainty of the mixed layer heat and salinity tendencies, three of the four budgets agreed. The exception was the ML salinity budget within the ACT box, where the salt tendency was significantly larger than the sum of the contributing fluxes during the first half of the experiment and vice versa in the second half of the observational period. Despite this caveat, the uncertainties inherent to the sum of the flux contributions and the tendencies are large, usually within  $\pm 50 \text{ W m}^{-2}$ , thus allowing leeway for neglected contributions.

One of these neglected flux contribution is vertical covariance of temperature (or salt) and velocity, a term describing advective contributions due to baroclinic currents and temperature (or salt, respectively) gradients in the ML. *Swenson and Hansen [1999]* showed that this contribution is small compared to the other terms of the mixed layer heat budget. Similarly, *Foltz et al. [2004]* reported that the salt-velocity covariance term is small compared to the other terms from equation 3.2 on time scales of 10 days and longer. Here, we have followed the results from these previous studies and neglected potential contributions from the vertical covariance.

In several previous heat and salt budget studies from the equatorial Atlantic, observed MLT and MLS tendencies could not sufficiently be described by the sum of flux contributions. Most of these studies lacked turbulence data to determine diapycnal fluxes. Instead, the residuals were interpreted in terms of diapycnal fluxes and average turbulent eddy diffusivities were calculated using the residual fluxes along with average temperature or salinity gradients from below the mixed layer [*Wade et al., 2011; Wang and McPhaden, 1999*]. To verify this approach, the residual of the sum of the flux contributions without

the diapycnal flux and the tendencies was calculated, and “residual” turbulent eddy diffusivity of heat ( $K_{h*}$ ) and salt ( $K_{S*}$ ) were calculated using average vertical gradients of temperature and salinity from below the ML.

For the ACT box, this approach yielded an average eddy diffusivity of heat of  $K_{h*} = 0.8 \times 10^{-4} \pm 0.3 \times 10^{-4} \text{ m}^2 \text{ s}^{-1}$  and an average eddy diffusivity of salt of  $K_{S*} = 2.0 \times 10^{-4} \pm 0.8 \times 10^{-4} \text{ m}^2 \text{ s}^{-1}$ , the latter being enhanced by a factor of 2.5. To serve as a comparison, the average diapycnal diffusivity estimated from microstructure observations within the ACT box yielded  $K_\rho = 1.5 \times 10^{-4} \pm 0.7 \times 10^{-4} \text{ m}^2 \text{ s}^{-1}$  (Tab. 5.1). It should be mentioned that  $K_{S*}$  was estimated from vertical salinity gradients sampled during the first month of the experiment only as in the second period of the experiment, the average vertical salinity gradients below the mixed layer vanished (cf. Fig. 4.14e and f).

The above average diffusivities lead to several conclusions. First of all, and as mentioned in section 3.5.2, the turbulent regime encountered in the equatorial Atlantic below the mixed layer suggests  $\langle K_h \rangle = \langle K_S \rangle = \langle K_\rho \rangle$ . Thus, within the uncertainties, neither  $K_{S*}$  nor  $K_{h*}$  is significantly different from  $K_\rho$ . However, as  $K_{S*}$  is significantly different from  $K_{h*}$ , this approach suggests that the diapycnal flux contribution cannot explain the residual between the sum of flux contributions and the tendency in the heat and salinity balances. Yet, fundamental to this is that the approach outlined above is valid. The analyzed microstructure data set here suggests that this is not the case. Intrinsic to the approach is that within the averaging box, the average diapycnal flux  $\overline{\langle K_\rho \cdot \frac{\partial T}{\partial z} \rangle}$  can be evaluated by using  $\overline{\langle K_\rho \rangle} \cdot \overline{\langle \frac{\partial T}{\partial z} \rangle}$  (or salinity gradients, respectively). This does not hold for the data collected within the ACT region. Here, there is a significant correlation between  $\langle K'_\rho \rangle$  and  $\langle (\frac{\partial T}{\partial z})' \rangle$  (and accordingly  $\langle (\frac{\partial S}{\partial z})' \rangle$ ) originating from regional differences within the ACT box. The magnitude of the correlation, estimated from microstructure observations for the diapycnal heat and salt fluxes, accounts for additional variability of  $0.4 \times 10^{-4} \text{ m}^2 \text{ s}^{-1}$  for  $K_{h*}$  and  $K_{S*}$ .

In the proximity of the EUC and thus in the region of elevated vertical shear where elevated mixing is most common, temperature gradients are reduced while salinity gradients are elevated (cf. Fig. 4.14) compared to elsewhere in the ACT box. In these mixing hot spot regions, higher turbulent eddy diffusivities in the case of temperature while lower eddy diffusivities in the case of freshwater are required for achieving a bulk of the diapycnal fluxes required to close the respective budgets. This fact also explains the discrepancy between the average  $K_\rho$  being larger than  $K_{h*}$  although within the ACT individual heat flux contributions and the mixed layer heat tendency agreed.

**Tab. 5.1:** Diapycnal diffusivities ( $\times 10^{-4} \text{ m}^2 \text{ s}^{-1}$ ) from observations (Obs.  $K_\rho$ ) and estimated from the heat budget residual (Res  $K_h$ ) and the salt budget residual (Res  $K_S$ ). Literature values from Box 7 and Box 8 by Wade *et al.* [2011] (W2011), at the equator at  $10^\circ \text{W}$  by Hummels *et al.* [2013] (H2013), at the equator at  $23^\circ \text{W}$  by Hummels *et al.* [2014] (H2014), and at the equator at  $23^\circ \text{W}$  and in the ITCZ-core region by Foltz *et al.* [2013] (F2013).

	Obs. $K_\rho$	Res $K_h$	Res $K_S$	W2011	H2013	H2014	F2013
<b>ACT</b>	1.4	0.7	2.2	2 (Box 8)	1.3 ( $10^\circ \text{W}$ )	2 ( $23^\circ \text{W}$ )	3.7 ( $23^\circ \text{W}$ )
<b>North</b>	-	-	-	1.5 (Box 7)	-	-	1.2 (ITCZ)

## 5.5 Summary

Within this chapter, the physical processes determining mixed-layer temperature and mixed-layer salinity changes during cold tongue development in 2011 were investigated using an extensive set of in-situ observations, climatological products and the output of a numerical model simulation. In contrast to other studies evaluating the individual contributions to the ML heat and salinity budget at individual locations or empirically defined boxes, the strategy pursued here was to evaluate the individual contributions for an entire box representative for the western ACT region and a region to the north of it. In general, the results concerning the ML heat budget agree with former studies within the same region [Hummels *et al.*, 2013; Jouanno *et al.*, 2011b; Wade *et al.*, 2011], despite the different approaches in terms of averaging regions. The diapycnal heat flux stands out as the dominant cooling term during ACT development for the entire region, which has been inferred here from direct microstructure observations as well as a residual approach and agrees with previous studies [Hummels *et al.*, 2013; Jouanno *et al.*, 2011b]. This gives confidence that the chosen region for averaging is adequate to investigate the contributions to the ML budgets representative for the western ACT.

The salinity budget has to our knowledge not been investigated within this region before. MLS slightly increases during ACT development, but a dominant effect of the diapycnal component could not be assessed for the salinity budget. This is due to the rather weak vertical salinity gradients at this location during the CTE period, partly even reversing in sign. For the salinity budget the horizontal advection, especially its zonal component, plays a more important role. The closure of the salinity budget is not quite as good as for the heat budget, although the diapycnal salt flux is considered. The contribution of the

different processes to MLT and/or MLS changes was examined and the main results for the CTE are:

ACT box

- The heat content tendency of the ML was negative throughout the CTE period. The net surface heat flux constantly warmed the ML. Dominant cooling terms were diapycnal mixing through the ML base, zonal advection of cold water from the GG and entrainment. The sum of these contributions balanced the observed MLT changes within the uncertainties.
- MLS tendency was positive during the beginning of the CTE in May and became close to zero during June and July. Evaporation exceeded precipitation throughout the experiment. Horizontal advection of freshwater was the dominant contributor to the budget from May to mid-June. In the beginning and at the end of the CTE entrainment had an increased effect on MLS, but was negligible throughout the rest of the observational period. The contribution of the diapycnal salt flux was only moderate.

North box

- Heat content tendency was negative during the CTE but considerably lower when compared to the ACT box. Net surface heat flux was small, warming the ML at the beginning of the CTE and cooling the ML afterwards. Horizontal heat advection cooled the ML during the entire CTE, except at the end of June, when advection contributed with a weak warming. Entrainment cooled the ML throughout the CTE. The sum of these contributions balanced the observed MLT changes within the uncertainties.
- The MLS content decreased in the beginning of the CTE during May and increased later in June and July. Precipitation was the main contributor to MLS changes during the beginning of the CTE in May, when zonal and meridional advection cancelled each other out. In June and July, when precipitation and evaporation were of similar magnitude, horizontal salinity advection, mainly the zonal component, and entrainment were the main contributors to the MLS increase, particularly in the beginning of June. The observed MLS tendency was balanced within the uncertainties by the sum of resolved flux contributions.

Zonal advective flux divergence is the main contributor to the MLS budget in the cen-

tral ACT region during the first half of the year. The overall gain of freshwater by zonal advection occurs within the two major branches of the SEC, the nSEC slightly north of the equator (mean position:  $1^{\circ}\text{N}$  at  $10^{\circ}\text{W}$  and  $2^{\circ}\text{N}$  at  $23^{\circ}\text{W}$ ) and the cSEC south of the equator (mean position:  $\sim 3\text{--}4^{\circ}\text{S}$  at  $10^{\circ}\text{W}$  and  $\sim 4^{\circ}\text{S}$  at  $23^{\circ}\text{W}$ ) [see e.g. *Brandt et al.*, 2006; *Kolodziejczyk et al.*, 2009; *Lumpkin and Garzoli*, 2005]. However, its contribution rapidly weakens towards the end of June. Due to the fact that the branches of the SEC are still present during this period, the strong weakening of the divergence of zonal advection results from a decrease of the zonal salinity gradient. In fact, a large MLS increase in the EEA in June and July 2011 was observed in the SMOS SSS (Fig. 4.2). As evaporation increases MLS in the central and eastern equatorial Atlantic homogeneously, the elevated salinities in the ML in the EEA have to have their origin in subsurface processes. Recently, *Kolodziejczyk et al.* [2014] conjectured vertical diffusion toward the sea surface in the GG occurring between May and August as the fate of the high-saline thermocline waters that are transported eastward within the EUC during the spring period *Johns et al.* [2014]. This requires enhanced diapycnal mixing in the GG from late boreal spring through summer, which was indeed indicated by numerical simulations *Jouanno et al.* [2011a].

Although the diapycnal salt flux was weak during the CTE it is in general a salinity-increasing contributor to the ML in the ACT region. This is due to the fact that the EUC core is generally associated with a subsurface salinity maximum and hence diapycnal mixing acts to increase MLS. Surprisingly though on some stations in the central ACT region diapycnal mixing partly contributed to decrease MLS in boreal summer. These local freshening events are due to the local reversal of the vertical salinity gradient below the ML. The question arises which processes are responsible for the reversal of the vertical salinity gradient. According to the findings by *Jouanno et al.* [2011a] and as hypothesized in recent studies by *Kolodziejczyk et al.* [2014] and *Johns et al.* [2014] a possible explanation is that a part of the additional salt in the ML was previously entrained or mixed from the thermocline layer in the GG (and parts of the central ACT) upwards, simultaneously eroding the salinity maximum of the EUC. Evaporation further increased the MLS, finally leading to a strong reduction or reversal of the vertical salinity gradient below the ML. Differing meridional displacements of existing meridional salinity gradients in the ML and the EUC below due to TIWs might as well contribute to local changes in the vertical salinity gradient below the ML, which is illustrated by the glider section at the PIRATA buoy at the equator,  $10^{\circ}\text{W}$ .

Strong local differences of vertical gradients and diapycnal diffusivities at the base of the ML within the boxes were observed. Diapycnal fluxes calculated by using box-averages of vertical gradients and diapycnal diffusivities do not agree with the box-average of locally calculated diapycnal fluxes due to a correlation of vertical gradients and diapycnal diffusivities. Similarly diapycnal mixing as conjectured from box-averaged budget residuals might become erroneous when averaging over larger regions. Microstructure observations as they are used here are still rather sparse. To get more reliable estimates on the variability in space and time of the diapycnal heat and salt fluxes at the ML base other observational platforms have to be used with higher spatial and/or temporal resolution such as e.g. gliders equipped with microstructure sensors or moored microstructure measurements.





## 6 Seasonal cycles in the central and eastern equatorial Atlantic

### 6.1 Introduction

In order to incorporate the different contributions to the ML budgets inferred during the CTE into a broader perspective, the above results are compared to the seasonal cycle of the contributions to the ML budgets estimated at three PIRATA buoy locations within the study area. For the salinity budget, the seasonal cycles of the individual contributions are estimated within the framework of this thesis at  $23^{\circ}\text{W}$  and  $10^{\circ}\text{W}$  on the equator, as well as  $4^{\circ}\text{N}$ ,  $23^{\circ}\text{W}$ . The seasonal ML heat budgets at these locations were already examined in various previous studies [e.g. *Foltz et al.*, 2003, 2013; *Hummels et al.*, 2013]. Hence, the results of the CTE concerning the ML heat budgets are compared to the results of the other studies.

The region around  $23^{\circ}\text{W}$  is associated with the western edge of the cold tongue. The buoy and the attendant mooring were deployed for the first time during the second deployment phase in March 1999 and are working since that time outstandingly. The second equatorial buoy with attendant mooring at  $10^{\circ}\text{W}$  was deployed even earlier during the first deployment phase between September 1997 and February 1998. The region around  $10^{\circ}\text{W}$  is associated with the center of the cold tongue. The annual cooling starts here and the lowest temperatures in the cold tongue region are observed at this site. Buoy and mooring worked and transmitted data very well, although some time lags occurred. In particular, during the first half of the deployment time, long periods without data transmission occurred. The third considered buoy in this thesis at  $4^{\circ}\text{N}/23^{\circ}\text{W}$  was deployed later in 2006. This buoy was deployed together with two other buoys at  $23^{\circ}\text{W}$  (at  $11.5^{\circ}\text{N}$  and at  $20.5^{\circ}\text{N}$ ) and belongs to the Northeast Extension. The region around this buoy site is the ITCZ core region.

## 6.2 Seasonal ML heat budgets

### 6.2.1 Seasonal heat budget in the ACT region

In general, the results on the individual contributions to the ML heat budget estimated during the CTE within this study agree with the individual contributions to the ML heat budget derived in other studies at the PIRATA buoy locations during ACT development. Despite the warming by the net surface heat flux in the central and eastern equatorial Atlantic during boreal summer, which was also shown from a variety of previous works, a strong ML cooling is observed. The largest contribution to the cooling within the ACT box during the CTE was found to be associated with the diapycnal ML heat loss. This agrees well with recent results from model studies *Jouanno et al.* [2011b] and from observations *Hummels et al.* [2013] during ACT development. Both studies showed mixing intensity in the central ACT to be associated with elevated vertical shear of horizontal velocities which is predominantly caused by vertical shear between the westward flowing SEC at the surface and the eastward flowing subsurface EUC. In boreal summer shear is further increased by TIW activity.

The zonal heat advection contributed significantly to the ML cooling, when strong westward velocities from the SEC branches occur together with large negative zonal temperature gradients. Compared to my results *Foltz et al.* [2003] showed a higher contribution during cold tongue onset and further development in boreal summer at the PIRATA buoy at 23°W at the equator and a weaker contribution at 10°W. They used a velocity product obtained by the procedure of *Grodsky and Carton* [2001] together with a monthly climatology of SST gradients from *Reynolds and Smith* [1994]. The contribution at 10°W was confirmed by *Hummels et al.* [2013], who used the same SST gradient climatology together with velocities inferred from surface drifts of Argo floats [*Lebedev et al.*, 2007]. Using the same velocity product as in this study, *Foltz et al.* [2013] estimated a contribution of total horizontal heat advection similar to the results here. However, they only showed the heat budget at the equatorial mooring at 23°W.

Other studies investigated the contribution of the eddy heat advection separately from the

mean advection terms. Close to the equator ( $1^{\circ}\text{S}$  to  $2^{\circ}\text{N}$ ), eddy heat advection, which is in boreal summer predominantly controlled by TIWs, has a warming effect on the ML of the ACT [Foltz *et al.*, 2003; Hummels *et al.*, 2013; Peter *et al.*, 2006; Wang and McPhaden, 1999]. Swenson and Hansen [1999] estimated the eddy heat advection indirectly by subtracting the mean heat advection from the residual of the total, derived from (quasi-Lagrangian) drifter SSTs, and local, calculated from climatological SSTs, temporal derivatives of ML temperature. This method was applied in several observational studies as the coarse temporal resolution (monthly) of surface velocities cannot explicitly resolve TIWs with a period of about a month. However, this approach was not applicable during the CTE covering only few TIW periods or wavelengths.

Due to the dominating effect of TIWs, eddy heat advection consists mainly of the high-frequency component of meridional velocity. Meridional velocities from the Mercator model output have the advantage of including both components of meridional velocity (mean and high frequency fluctuations) (Figs. 3.8c and d). Hence, the meridional heat advection estimated with Mercator velocities accounts for the mean meridional heat advection as well as the eddy advection term. Mean meridional heat advection in the western ACT close to the equator was found to cool the ML [Foltz *et al.*, 2003; Hummels *et al.*, 2013; Peter *et al.*, 2006]. Thus, mean meridional heat advection and eddy heat advection should partly compensate each other. Surprisingly, although meridional velocities from OSCAR do not include TIW activity and rather close to zero most of the time (Figs. 3.8c and d), the estimate of the meridional heat advection with OSCAR velocities shows comparable values to the ones for the Mercator model output. The contribution of meridional heat advection to the ML heat budget in the ACT box is small during the complete CTE with OSCAR velocities (Fig. 5.2c) and only marginally larger with the Mercator velocities (cf. Fig. 3.10d). Note, that our estimate agrees well with the sum of the mean meridional heat advection and the eddy advection taken from Foltz *et al.* [2003] or Hummels *et al.* [2013] during the same season.

Entrainment was calculated from model output and contributed to cooling during the CTE. Previous studies also reported ML cooling by entrainment on the order of  $10\text{--}20\text{ Wm}^{-2}$  during ACT development [Foltz *et al.*, 2003; Hummels *et al.*, 2013; Wade *et al.*, 2011], which agrees in magnitude to the results obtained here. However, Rhein *et al.* [2010], who inferred vertical velocities using helium isotopes, found heat fluxes due to entrainment as large as  $138\text{ Wm}^{-2}$  from data collected during late June in 2006 at  $10^{\circ}\text{W}$ , while for early

June 2006,  $12 \text{ Wm}^{-2}$  were determined. The magnitude of entrainment is crucially dependent on the definition of the temperature change between the averaged ML value and the value considered at base of the ML. Literature values of predefined temperature differences range from  $0.75^\circ\text{C}$  up to  $4^\circ\text{C}$  [Hayes *et al.*, 1991; Seager *et al.*, 1988; Swenson and Hansen, 1999; Wyrki, 1981], or fixed depth intervals, such as e.g. the temperature or salinity 20 meters below the ML base [Chang, 1993; Wang and McPhaden, 1999]. In this study the temperatures 5 meters below the ML were used for defining the difference, which resulted in values between  $\sim 0.7$ -  $1.4^\circ\text{C}$ . These are in agreement to other studies [Hayes *et al.*, 1991; Swenson and Hansen, 1999].

### 6.2.2 Seasonal heat budget in the Northern box

Recently, Foltz *et al.* [2013] showed a climatological heat budget in a box ( $18^\circ\text{W}$ - $28^\circ\text{W}$ ,  $3^\circ\text{N}$ - $8^\circ\text{N}$ ), similar to our northern box, and at the PIRATA buoy at  $4^\circ\text{N}$ ,  $23^\circ\text{W}$ . They reported a ML cooling during boreal summer, which fits to the results obtained during the CTE. In their study region, net surface heat fluxes dominated the ML heat balance and a residual of  $-20$  to  $-25 \text{ Wm}^{-2}$  remained during the CTE time period. Their estimates of latent and sensible heat fluxes, net surface shortwave radiation, and net surface longwave radiation are very similar to our estimates in the northern box. At the PIRATA buoy, they showed a residual of  $-15$  to  $-50 \text{ Wm}^{-2}$  during May/June, which was reduced due to strong cooling by horizontal heat advection in July. Our estimates of horizontal heat advection are even slightly higher than the ones reported in Foltz *et al.* [2013], who only provided information about the total advection, without distinguishing between zonal, meridional or eddy advection. Note, that monthly means from more than ten years of data were estimated.

## 6.3 Seasonal ML salinity budgets

To estimate the seasonal cycles of the contributing terms to the seasonal ML salinity budget (eq. 3.2), several datasets were tested and compared with each other (cf. 3.4.6). The contribution of the several terms, calculated with the different data sets used, to ML changes at the three considered buoy sites is shown for every buoy first. For the budget

calculation finally the chosen data from AMSR-E, TropFlux and the combined drifter and float velocity product are used.

### 6.3.1 0°N, 23°W

The zonal salinity advection at the buoy at 0°N, 23°W is similar in all compared data sets by following a semiannual cycle (Fig. 6.1a). The minima in salinity advection (strongest freshwater advection) are in December/January and June/July. This is in agreement to the seasonal cycle of zonal advection with maximum westward velocities in boreal winter and summer. However, the strength and even the direction of the advection is significant different. The estimates with OSCAR and with direct PIRATA MCM observations change the sign in advection in boreal spring and fall.

The contribution of meridional advection to MLS changes is the most uncertain term (Fig. 6.1c). Almost no advection is present when using OSCAR. This is in agreement to the weak observed meridional velocities at the equator. Using the YOMAHA'07 dataset, the meridional advection contributes during the whole to a MLS increase. In contrast, the estimates with the drifter dataset show a freshening due to meridional advection except in January and February. The combination of both (Yom/Drif) describes an annual cycle with the maximum in boreal fall/winter when southeasterly winds accelerate and advect high saline water from the southern tropical Atlantic equatorward. In boreal summer a southward current advects fresher water from the north southward to the equator.

The seasonal cycle in evaporation is similar in all considered data sets with a weak maximum in April/May. Generally this term is nearly constant all over the year (Fig. 6.1b). Precipitation in the western cold tongue region is present from the late fall until early summer with a maximum in March/April (Fig. 6.1d). This temporal evolution follows the migration of the ITCZ with its southernmost position at 23°W near the equator in March/April. Although the seasonal cycle is similar in all datasets, the amplitude differs significantly. The relative error during boreal fall reaches 50% when comparing the several products with each other.

From January to May precipitation exceeds evaporation in the western cold tongue region in the mean seasonal cycle estimated for the years 1999-2012 at the equatorial PIRATA buoy at 23°W (Fig. 6.2a). Later in the year precipitation is negligible and nearly constant

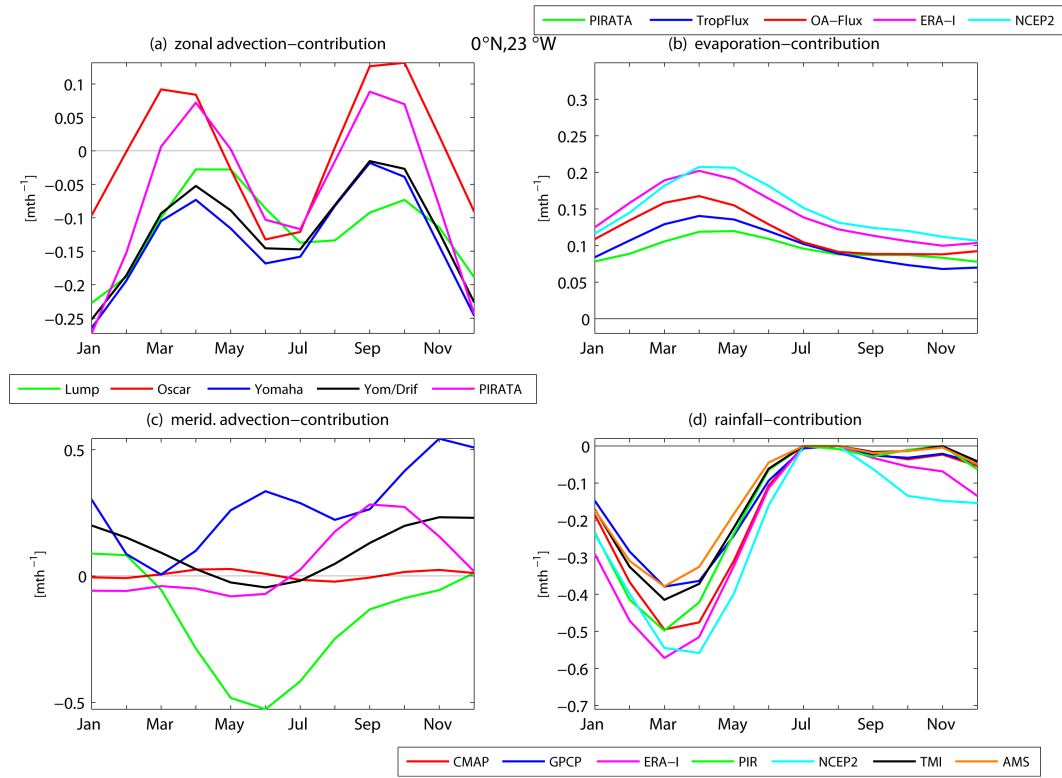


**Fig. 6.1:** Seasonal cycles of the (a) zonal advection, (b) evaporation, (c) meridional advection, (d) precipitation at the PIRATA buoy at 0°N, 23°W with different data sets. PIR or PIRATA denotes the direct observations at the buoy site.

evaporation yields a positive surface freshwater flux. Similarly, in 2011 during the CTE period from May to July, the influence of precipitation on the ML salinity budget was weak in the ACT region and a positive freshwater flux due to excess evaporation with only weak variability was indicated. This freshwater flux contributed to an MLS increase, comparable to the climatological freshwater flux from May to July (Fig. 6.2a).

The mean seasonal cycle of zonal advection at the buoy site shows a freshwater contribution at the western edge of the cold tongue during the entire year having a semiannual cycle in amplitude. While representing a significant contribution to the total salinity budget, the zonal advective freshwater flux peaks in boreal summer and winter. The results for boreal summer are consistent with those from the CTE period, but weaker in magnitude. Meridional advection exhibits a maximum in boreal winter and represents the largest positive flux contribution to the MLS budget. Eddy salt advection reduces MLS content at  $23^{\circ}\text{W}$  and is largest in the boreal winter months. At the end of spring, the contribution is negligible but is again relevant during summer. The sum of the seasonal cycle of mean meridional advection and eddy salt advection at the buoy site is small in boreal summer. Due to the fact that eddy variability at  $23^{\circ}\text{W}$  is dominated by TIWs and the meridional gradients exceed the zonal ones, eddy advection is presumed to consist mostly of the meridional eddy component. Hence, the total meridional advection being small agrees with the results from the CTE (Fig. 6.2a). However, the sum is negative from May to July, indicating meridional freshwater advection, which is different from the results obtained from the CTE.

Within the seasonal cycle, entrainment at the PIRATA buoy at  $23^{\circ}\text{W}$  has its maximum during May and June (Fig. 6.2a) when it contributes to a salinity increase. During the rest of the year, its contribution is weak. Within the ACT and during the CTE period in 2011, the weak salinity difference between the ML and below the ML resulted in weak entrainment contributions to MLS changes, albeit elevated entrainment velocities. Entrainment generally is variable and a comparison between local estimates at the buoy and the box-average fails at this location.

The diapycnal salt flux calculated from individual cruise data (section 3.5.3) exhibits elevated variability within the seasonal cycle at  $23^{\circ}\text{W}$ . Strongest diapycnal fluxes leading to a MLS increase occur during February-March. Additionally, fluxes are elevated in June and November. In May and July, its contribution at  $23^{\circ}\text{W}$  is weak. The results for June

and July are comparable to the CTE results from 2011, when the diapycnal salt flux led to a MLS increase in June and had a negligible contribution in July.

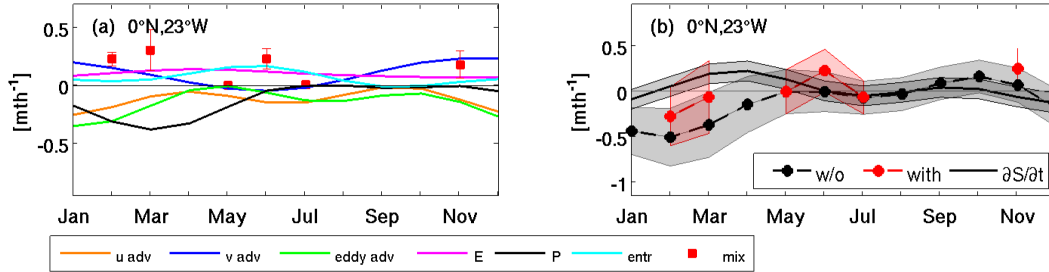


**Fig. 6.2:** Seasonal cycles of the contributing terms to the ML salinity budget (left) and the comparison of the local salinity tendency and the sum of the contributing terms (right) at the PIRATA buoy at 0°N, 23°W. Black dashed-dotted lines (right panels) are the sum without diapycnal mixing and red dots are the sum with diapycnal mixing.

The seasonal cycle of the salinity tendency at the equatorial PIRATA buoy at 23°W is weak, but shows a positive tendency during spring, which reduces and even reverses towards July (Fig. 6.2b). The weak variability of the MLS tendency is generally captured by the sum of the contributing terms. In February and March, the salinity-increasing contribution of the diapycnal salt flux decreases the imbalance between tendency and the sum of fluxes. During this period, large freshening contributions result from zonal advection, eddy advection as well as precipitation while the diapycnal flux increases MLS. Although the seasonal cycle was evaluated locally, the results generally agree with the findings during the CTE pointing towards the fact that the salinity variability observed during the CTE is typical for this season (Figs. 5.5d, 6.2b). However, some flux contributions, in particular entrainment, may vary locally within the ACT during the seasonal cycle.

### 6.3.2 0°N, 10°W

The zonal salinity advection at the buoy at 0°N, 10°W is different in all compared data sets (Fig. 6.3a). While the advection with OSCAR and the drifter velocities can be described with a semiannual cycle, the estimates from the YOMAHA '07 velocities and the combined product are described with an annual cycle. The strongest westward freshwater advection is during boreal spring in all datasets except OSCAR, where it is later in June. Positive zonal salinity advection, due to eastward velocities, are observed during early spring and



early fall with OSCAR. Advection estimated calculated with YOMAHA'07 and the combined product show weak positive salinity advection in September and October as well.

Meridional salinity advection to MLS changes is positive with all used velocity products except with OSCAR in September (Fig. 6.3c). Almost no advection is present when using OSCAR. This is again in agreement to the weak observed meridional velocities at the equator like at the buoy at 0°N, 23°W (cf. Figs. 6.1b and 3.8d). Using the YOMAHA'07 dataset, the meridional advection contributes during the whole year largely to a MLS increase. The meridional advection when using the combined product is similar to YOMAHA'07 but weaker in amplitude. The downstream northward current, resulting from a constant southern wind leads to the positive salinity advection by advecting saltier water from south of the equator northward.

The seasonal cycle in evaporation is similar in all considered data sets with a weak maximum in March/April/May and follows an annual cycle. Evaporation constantly contributes to a MLS increase all over the year (Fig. 6.3b). Precipitation in the central cold tongue region is present from the late fall until early summer with a maximum in February/March/April (Fig. 6.3d). This temporal evolution follows the migration of the ITCZ with its southernmost position at 10°W near the equator in early boreal spring. Although the seasonal cycle is similar in all datasets, the amplitude differs significantly. Satellite estimates are generally weaker than direct buoy observations and reanalysis datasets.

In winter and early spring, the mean seasonal cycles of evaporation and precipitation estimated for the years 1999-2012 at the equatorial PIRATA buoy at 10°W, are comparable in magnitude, resulting in a weak, negligible surface freshwater flux (Fig. 6.4a). During the rest of the year, evaporation exceeds precipitation, thus the surface freshwater flux leads to an increase of the MLS. This is comparable to the freshwater flux in the ACT region during the CTE period. Additionally, comparable results of the surface freshwater flux were obtained by *Da-Allada et al.* [2013] for the GG, suggesting that the surface freshwater flux is a large-scale phenomenon during this period.

Zonal advection is the largest contributing term to the mean seasonal cycle of the MLS balance at the equator at 10°W. It acts to reduce MLS and is most pronounced from December until July. Later in the year, its contribution weakens (Fig. 6.4a). Although zonal

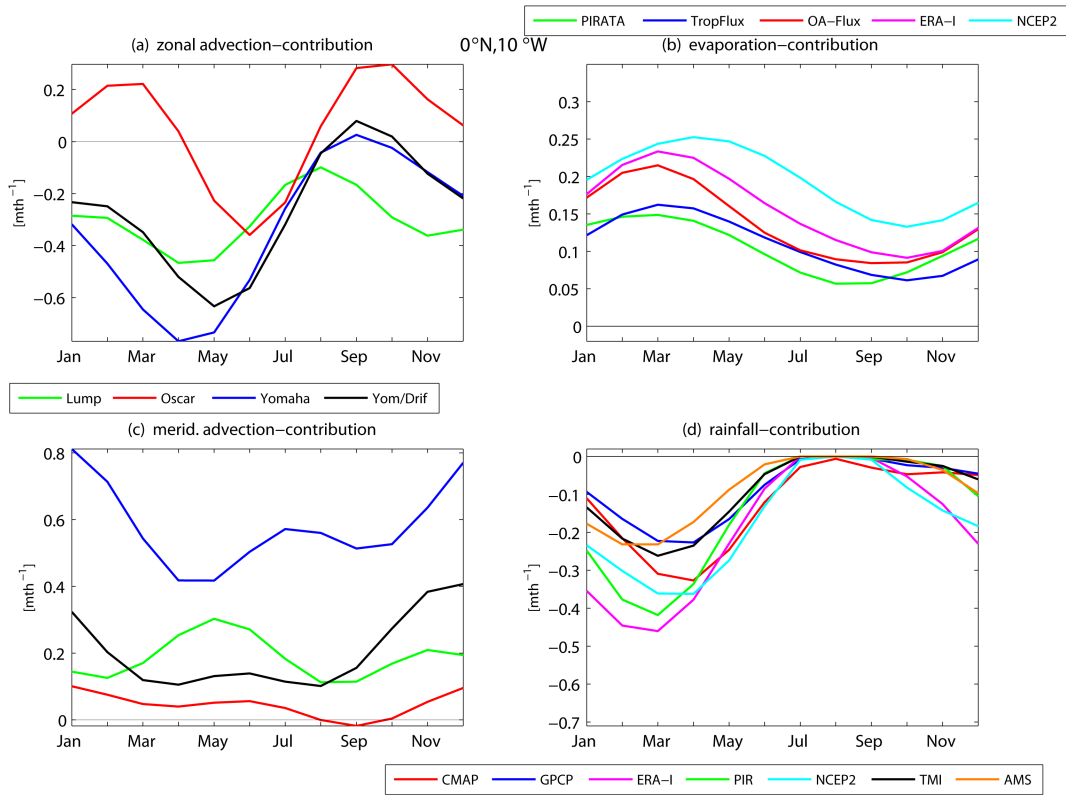


**Fig. 6.3:** Same as figure 6.1, but at  $0^{\circ}\text{N}, 10^{\circ}\text{W}$ .

advection at  $23^{\circ}\text{W}$  is reduced compared to  $10^{\circ}\text{W}$ , zonal advection in the ACT region during the CTE period is of similar magnitude compared to  $10^{\circ}\text{W}$  and also shows a similar temporal evolution. This freshening contribution to the mixed-layer balance can be explained by divergence of freshwater transport within the westward current branches, the northern SEC (nSEC) and the central SEC (cSEC). However, as will be discussed in chapter 7 the seasonal evolution of the zonal advection term is predominantly controlled by the seasonal evolution of zonal mixed-layer salinity gradients. In general, the spring/early summer dominance of zonal advection in the MLS budget found here also agrees with recent results from a model mixed-layer salinity balance study in the GG region reported by *Da-Allada et al.* [2013].

Similar to the results from  $23^{\circ}\text{W}$ , the MLS contribution from meridional advection has a maximum in late fall/early winter. During this period, the divergence of meridional salt transport represents the dominant MLS source at  $10^{\circ}\text{W}$  (Fig. 6.4a). Magnitude and phase of eddy salinity advection at  $10^{\circ}\text{W}$  is also very similar to  $23^{\circ}\text{W}$ . It exhibits a semiannual cycle with minimum in December/January and July/August. From August to October, eddy salt advection is the main freshening contributor for the ML. The sum of the seasonal cycle of mean meridional advection and eddy salt advection at the mooring site is again small (cf.  $23^{\circ}\text{W}$ ) in boreal summer, which is similar to the total meridional advection estimated during the CTE. Also as for  $23^{\circ}\text{W}$ , the sum during June and July is negative, indicating meridional freshwater advection, which was not found during the CTE.

The seasonal cycle of entrainment at the PIRATA buoy at  $10^{\circ}\text{W}$  has its maximum in March and April being the largest contribution to the MLS increase during this period (Fig. 6.4a). During the rest of the year the contribution of entrainment is weak. This is consistent with the estimate of entrainment during the CTE, when the contribution of entrainment was rather negligible due to weak salinity differences between the ML and below the ML albeit rather strong entrainment velocities. Weak positive and negative entrainment contributions to MLS changes were obtained due to sign changes in salinity difference between the ML and below the ML.

The diapycnal salt flux at the  $10^{\circ}\text{W}$ -PIRATA buoy increases the MLS in May and June, followed by a freshening contribution during July. Later in September and November again a positive salt flux from the subsurface layer into the ML through diapycnal mixing was observed. The findings for June and July are comparable with the CTE results that

showed a positive diapycnal flux, leading to a MLS increase during June, followed by a negligible MLS contribution in July 2011.

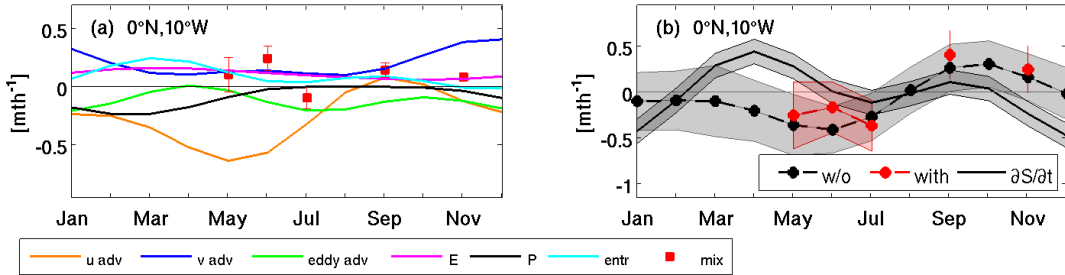


**Fig. 6.4:** Same as figure 6.2, but at 0°N, 10°W.

The observed ML salinity increase during May 2011 in the ACT region is identifiable in the seasonal cycle of the salinity tendency at 10°W (and 23°W) as well (Fig. 6.4b). This increase weakens during June and July in the central ACT region. The MLS increase at the equatorial PIRATA buoy at 10°W is not explained by the considered processes from equation 3.2. The remaining residual indicates either a missing source of salinity or an overestimate of the freshening contributions (Fig. 6.4b). The observed diapycnal salinity flux in May and June adds salt to the ML and thus reduces the residual, leading to a balanced salinity budget within the uncertainties during these months. For March through May, vertical salinity gradients between the ML and thermocline are largest (cf. Fig. 4.14). It is thus likely that diapycnal fluxes during this period contribute to increase MLS and thus decrease the residual. However, currently, no microstructure observations from 10°W during these months are available. The remaining imbalance between the sum of terms and the observed salinity tendency at this location also coincides with periods of elevated zonal advection (March to July) and periods of elevated meridional advection (September to December). If these terms would be responsible for the imbalance and hence overestimated this has to be either caused by overestimated velocities or horizontal salinity gradients. As the same velocity product did not cause imbalances in the ML heat budget at this location [Hummels *et al.*, 2014], it could be argued that the zonal and meridional salinity gradients are still not sufficiently well observed by Argo floats.

### 6.3.3 4°N, 23°W

The zonal salinity advection at the buoy at 4°N, 23°W is weaker in magnitude compared to the equatorial buoy sites (Fig. 6.5a). While the advection with OSCAR, the drifter velocities and the direct MCM observations at the mooring can be described with a semi-annual cycle, the estimates from the YOMAHA'07 velocities and the combined product are described with an annual cycle. The strongest eastward salinity advection is during boreal spring in the drifter dataset and the mooring observations. A second maximum in positive zonal salinity advection, due to eastward velocities, is observed in early fall with all datasets.

Meridional salinity advection to MLS changes can be described with a semiannual cycle in all datasets (Fig. 6.5c). A freshwater advection from the north during late winter/early spring is followed by northward salinity advection in May/June. Exactly between these two regimes the ITCZ has crossed the buoy position and therefore northerly winds in February/March were followed by southerlies. After a weakening in early fall the meridional salinity advection has its maximum in late fall. This resulted from enhanced southward meridional salinity gradients.

The seasonal cycle in evaporation is weak in all considered data sets with a weak maximum in May and follows an semiannual cycle. Evaporation constantly contributes to a MLS increase all over the year (Fig. 6.5b). Precipitation at the buoy site at 4°N, 23°W is present all over the year with a maximum in May and a second maximum in November (Fig. 6.5d). This temporal evolution follows the migration of the ITCZ with two buoy crossings. Although the seasonal cycle is similar in all datasets, the amplitude is significantly, in particular from the direct buoy observations.

Precipitation is the dominant flux contributing to the mean seasonal cycle at the PIRATA buoy at 4°N, 23°W. It follows a semiannual cycle caused by the seasonal migration of the ITCZ (Fig. 6.6a). During May-July the contribution weakens due to the northward migration of the ITCZ. However, although it is reduced during this period, precipitation was the dominant contributor to MLS changes in the northern box during the CTE (Fig. 5.7a). Monthly mean evaporation is nearly constant over the year, but reduced compared to evaporation at the two equatorial locations. Hence, the net surface freshwater flux at 4°N, 23°W is predominantly determined by the semiannual cycle of precipitation and is

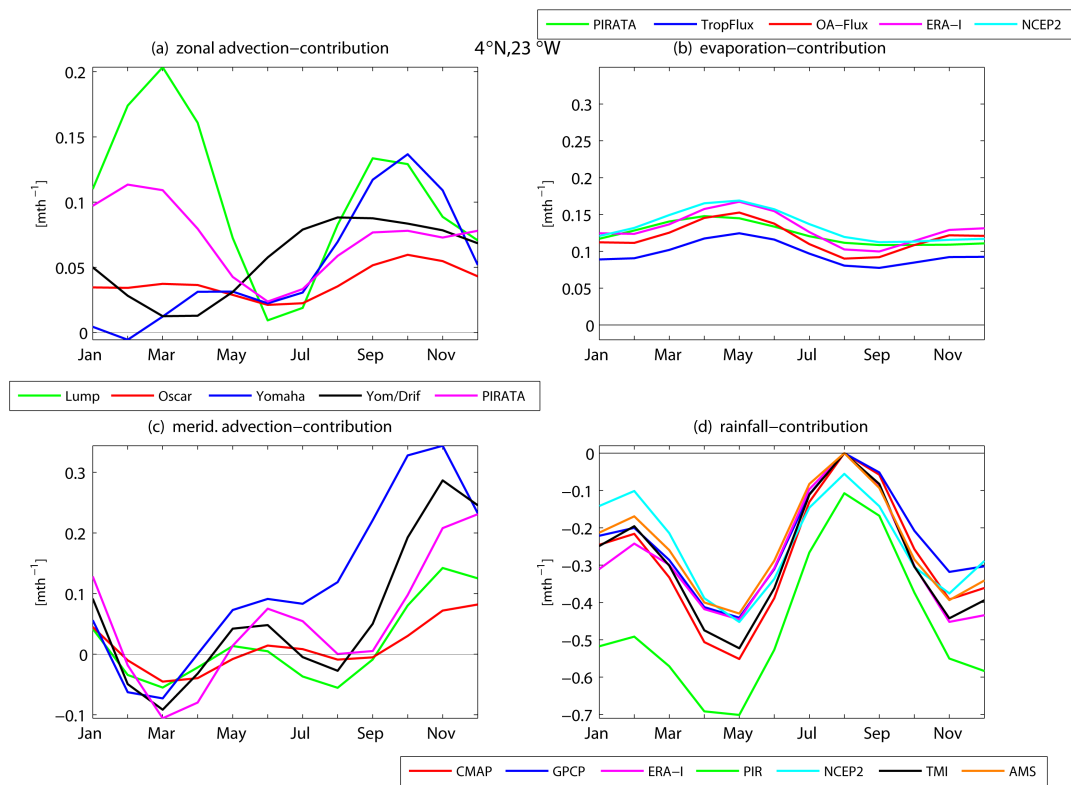


**Fig. 6.5:** Same as figure 6.1, but at  $4^{\circ}\text{N}, 23^{\circ}\text{W}$ .

only positive only in July and August, when precipitation is strongly reduced.

The seasonal cycle of zonal advection at the buoy site is weak and follows the seasonal cycle of the NECC, which strengthens from its minimum eastward velocity during boreal spring to the maximum in July [e.g. *Goes et al.*, 2013; *Richardson and Reverdin*, 1987]. The monthly mean zonal advection during May-July at the buoy site is much weaker than suggested for the northern box during the CTE period in 2011. In particular, the variability of zonal advection included a change in sign during the CTE, which is not captured in the seasonal estimate at the buoy location.

Meridional advection has its maximum in late fall/early winter and is the main contributor for the increase of the MLS in this period (Fig. 5.7a). Eddy salt advection exhibits a weak semiannual cycle with a freshening contribution in April/May and from October to December. During the latter period, eddy salt flux divergence is elevated but negative, leading to a decrease of MLS content. The sum of the seasonal cycle of mean meridional advection and eddy salt advection at the mooring site is small in boreal summer, which is similar to the total meridional advection estimated during the CTE. The sum during May is negative, indicating meridional freshwater advection, which was not determined from the data collected during the CTE period. During June and July the sum is positive, indicating meridional salinity advection, similar to the results found during the CTE.

While contributing to the MLS increase during the CTE period, entrainment exhibits a maximum in spring. This term represents the dominant salinity contribution to the ML during this period. During the CTE, the entrainment was variable and contributed strongly to a MLS increase in June as well. The diapycnal salt flux is negligible throughout the year. The sum of the contributing terms balances the observed salinity tendency within the uncertainties over the entire year at the PIRATA buoy at 4°N, 23°W (Fig. 5.7b).

## 6.4 Summary

To address the generality of the results obtained during the CTE period, the mean seasonal cycle of the flux contributions to MLS and its tendency was evaluated at three PIRATA buoy locations, on the equator at 23°W and 10°W and at 4°N, 23°W. Overall, the domi-

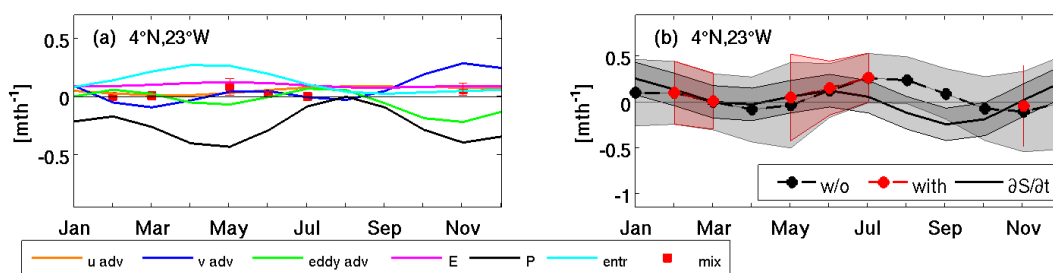


**Fig. 6.6:** Same as figure 6.2, but at 4°N, 23°W.

nant flux contributions determined at the buoy positions for the CTE period agreed well in magnitude and phase with the box averaged flux contributions. At the equatorial locations, zonal advective flux divergence is the dominant term contributing to a freshening of the ML from December until July. However, the magnitude of the contribution is a factor of two larger in the central ACT region at 10°W compared to the western ACT region 23°W. Precipitation and meridional eddy advection also significantly contribute to a freshening of the ML within the ACT region throughout the year. Meridional advection, entrainment and evaporation contribute to increasing salinity in the ML. All three fluxes vary in magnitude during the season. Finally, the divergence of diapycnal salinity flux increases salinity predominantly from November to June and is negligible during the other month of the year. The results emphasize that the mixed layer salinity tendency is largely balanced by ocean processes and to a lesser extent by the net surface freshwater flux.



## 7 Synthesis

This thesis presents new results from a two-month lasting experiment in the central and eastern equatorial Atlantic during the cold tongue development in 2011. The findings of this thesis increase the knowledge about the dynamics within the mixed layer during the development of the Atlantic cold tongue. The Atlantic cold tongue is the most striking annual phenomenon in the EEA with a SST and MLT decrease of up to 6°C in boreal summer. The cold tongue coincides with the seasonal evolution of the so-called zonal mode, a pattern of ocean-atmosphere variability similar to the El Niño-Southern Oscillation (ENSO) phenomenon in the Pacific. The interannual variability of the cold tongue onset is strongly correlated to the strength and the onset of the WAM and other rainfall patterns, which are of climatic relevance for the adjacent countries. The drivers of the cooling are rather well understood, but the exact contribution of the several processes to ML changes, in particular ML dynamics like horizontal advection and diapycnal mixing, as well as the predictability of the cold tongue SST/MLT is uncertain and of high interest in ocean science. The improved understanding of mixed layer dynamics might help to minimize these uncertainties. Observations are essential for the exact understanding of ML variability and the goal of this thesis was to describe the ML dynamics during the cold tongue development with observational data and, in particular, to highlight the role and the variability of salinity as the second density determining property beside the temperature.

With an extensive database it was possible to describe all processes, which are important for the upper ocean mixed layer as the interface from the ocean and the atmosphere. The year 2011 was remarkable in particular in the central cold tongue region compared to the average year. Here, an early onset together with a strong cooling and a large salinity increase in the ML was observed. Furthermore, the vertical salinity gradient changed sign in late June and July, which was not expected, but is an annual phenomenon in the central cold tongue and further east as shown in this thesis as well as in previous studies. However, the setup of the experiment in the year 2011 nicely fit the cold tongue development

and the results can be seen as generally valid, in particular when compared with results of previous studies. The region north of the cold tongue, strongly influenced by the ITCZ, and here also shown in a comparative manner to the cold tongue region, is in terms of heat changes mainly influenced by the net surface heat flux. For the Atlantic cold tongue between 23°W and 10°W, the main contribution of diapycnal mixing below the mixed layer, caused by the shear of the zonal currents, for the cooling of the ML was shown. The cooling contribution of zonal advection and entrainment was balanced by the warming due to the net surface heat flux. This is in outstanding agreement compared to former studies based on observations as well as models, which described seasonal cycles of ML heat variability. As an advancement to the previous studies, this thesis shows that the main cooling contribution of mixing is valid for the entire western cold tongue region. Within the CTE it was also shown that diapycnal mixing, compared to the cooling contribution of the SST and the mixed layer, has a reduced impact on salinity changes of the upper ocean. Generally, the variability of salinity in the central and eastern equatorial Atlantic is small during the development of the cold tongue. The contribution of diapycnal mixing as well as of entrainment in the central cold tongue region is higher on seasonal scales using almost 15 years of data from moored buoy observations. The year 2011 might be special in this context, because largely reduced vertical salinity gradients, compared to the mean year, were observed. Furthermore, it was shown that the salinity itself is not determining the ML characteristics, i.e. the pycnocline coincides with the thermocline, and also no salinity-effect on the cold tongue evolution could be pointed out.

It turned out that precipitation is the dominant salinity changing contribution in the northern region and the zonal advective flux divergence is the main driver for salinity changes in the ACT region. The precipitation in the ACT region weakened in spring with the northward migration of the ITCZ and the advection due to strong surface currents freshened the western cold tongue region during the early onset of the development. Later in boreal summer it was reduced due to weakened lateral gradients, which can be also seen in the seasonal cycles at two equatorial buoys. The results lead to the assumption that the evolution in the central equatorial Atlantic is strongly dependent from dynamics further east towards the African coast. In the northern region also strong variability of zonal advection during the CTE, related to the seasonal maximum of the NECC, was shown. Generally, zonal advection in this region follows the seasonal cycle of the NECC. In the EEA, in particular in the GG, also mixing might contribute stronger to subsurface dynamics, although observational studies show enhanced stratification. This stratification

is related to high vertical salinity gradients in the EEA, which reduce in boreal summer, along with the erosion of the EUC core, as shown in recent studies and also pointed out here for the central cold tongue region. The knowledge of the salinity variability, in particular related to the exchange of freshwater between the ocean and the atmosphere and between the mixed layer and the thermocline is a main question for future studies. The strong salinity increase in the eastern equatorial Atlantic during boreal spring and summer requires further knowledge of vertical or diapycnal exchange processes, which can be achieved by moored mixing observations or gliders equipped with microstructure probes. Together with these measurements of meridional and vertical velocity shear, the role of TIWs, generated by the shear instabilities, as well as other wave phenomena in the EEA for the salinity variability have to be further examined. Also the predictability of the surface freshwater flux is of strong interest, not least in relation to the observed as well as modeled intensification of the hydrologic cycle. For this a better observation and prediction of surface salinities is necessary, e.g. to use them in the framework of the ocean rain gauge concept.

Satellite observations more and more deliver the database of sea surface salinities. These data are constrained to the surface (the first few centimeters), but with satellite data global pictures of the oceans on daily scales are available. While temperature, altimetry and the lower atmosphere are observed from satellites for decades, the monitoring of the sea surface salinity is relatively new. Two missions are operating in parallel and the first results are promising. Within this thesis satellite salinity data used and compared with in-situ observations and reveal a rather good agreement. The experiment was used for testing several satellite and reanalysis datasets against in-situ observations. For the turbulent and radiative heat fluxes between the ocean and the atmosphere good agreements were shown between particular satellite products and the observation. Concerning precipitation, reanalysis as well as satellite observations are erroneous and have to be validated against in-situ observations. Regular observations at sea are sparse; only a few buoys and ships are constantly measuring precipitation far away from the coasts. In this study a large dataset of ship-based observations of precipitation was obtained and used for the validation of satellite data. The results showed a passably well agreement for two satellite products. The validation of satellite data with observations from all platforms persists a main topic for the next years, not only for salinity observations.

This dissertation was initiated with the goal to understand driving mechanisms of salinity

variability in the tropical Atlantic. Although a complete closure of the mixed layer salinity budget failed due to missing data and/or methodical limits, the setup and the experiment itself was a success story. It was possible to get a complete picture of mixed layer changes during the onset of the cold tongue in 2011. From an observational point of view this also includes the feasibility to observe and the usability of the observations from the surface to the depth. Nowadays several common observational platforms are in use, where the Argo program with more than 3000 floats is the most prominent. The Argo data provide an amazing dataset of ocean hydrography as well as an Lagrangian view of the surface circulation and a discret depth (usually 1000m). The floats work autonomously for up to 4 years. A second frequently used database are the timeseries of several oceanographic and atmospheric parameters observed at moored buoys within the TAO/PIRATA/RAMA program. The freely available data of these both platforms are the basis of countless studies about the ocean and are also used within this thesis.

However, both aforementioned platforms are limited when either short timescales or larger areas (or both together) come to the fore. The essential source of data from research cruises is irreplaceable. Observations of the hydrography, the vertical current field, the finescale structure of the currents and the hydrography and of local atmospheric parameters can be obtained for a limited period with an excellent resolution. Recently, additional autonomous devices entered the scientific community. One of these devices are gliders. The autonomous underwater vehicles can observe the hydrography and additional biological and chemical parameters in a determined area for a limited time in the order of weeks or months. Both, cruise data and the results from a glider swarm experiment, were the database for this thesis. This limited the duration of the experiment to two months, which outstandingly fit to the period of the cold tongue onset as described above.

# Bibliography

- Adler, R. F., G. J. Huffman, A. Chang, R. Ferraro, P.-P. Xie, J. Janowiak, B. Rudolf, U. Schneider, S. Curtis, D. Bolvin *et al.*: The Version-2 Global Precipitation Climatology Project (GPCP) Monthly Precipitation Analysis (1979-Present). *Journal of Hydrometeorology*, **4**, 1147–1167 (2003).
- Allen, M. R. and W. J. Ingram: Constraints on future changes in climate and the hydrologic cycle. *Nature*, **419**, 224–232 (2002), [10.1038/nature01092](https://doi.org/10.1038/nature01092).
- Alory, G., C. Maes, T. Delcroix, N. Reul and S. Illig: Seasonal dynamics of sea surface salinity off Panama: The far Eastern Pacific Fresh Pool. *Journal of Geophysical Research: Oceans*, **117**, C04028 (2012).
- Antonov, J. I., D. Seidov, T. P. Boyer, R. A. Locarnini, A. V. Mishonov, H. E. Garcia, O. K. Baranova, M. M. Zweng and D. R. Johnson: World Ocean Atlas 2009, vol. 2, Salinity, edited by S. Levitus. *NOAA Atlas NESDIS*, **69** (2010).
- Atlas, R., R. N. Hoffman, J. Ardizzone, S. M. Leidner, J. C. Jusem, D. K. Smith and D. Gombos: A cross-calibrated, multiplatform ocean surface wind velocity product for meteorological and oceanographic applications. *Bulletin of the American Meteorological Society*, **92**, 157–174 (2011).
- Berger, M., A. Camps, J. Font, Y. Kerr, J. Miller, J. Johannessen, J. Boutin, M. R. Drinkwater, N. Skou, N. Floury, M. Rast, H. Rebhan and E. Attema: Measuring ocean salinity with ESA’s SMOS mission - Advancing the science. *Esa Bulletin-European Space Agency*, pp. 113–121 (2002).
- Bingham, F. M., G. R. Foltz and M. J. McPhaden: Characteristics of the seasonal cycle of surface layer salinity in the global ocean. *Ocean Science*, **8**, 915–929 (2012), URL <http://www.ocean-sci.net/8/915/2012/>.
- Bonjean, F. and G. S. E. Lagerloef: Diagnostic model and analysis of the surface currents in the tropical Pacific Ocean. *Journal of Physical Oceanography*, **32**, 2938–2954 (2002).
- Bourlès, B., R. Lumpkin, M. J. McPhaden, F. Hernandez, P. Nobre, E. Campos, L. Yu, S. Planton, A. J. Busalacchi, A. D. Moura *et al.*: The PIRATA program: History, accomplishments, and future directions. *Bulletin of the American Meteorological Society* (2008).

- Boutin, J., N. Martin, G. Reverdin, X. Yin and F. Gaillard: Sea surface freshening inferred from SMOS and ARGO salinity: impact of rain. *Ocean Science*, **9**, 183–192 (2013).
- Boutin, J., N. Martin, X. B. Yin, J. Font, N. Reul and P. Spurgeon: First Assessment of SMOS Data Over Open Ocean: Part II-Sea Surface Salinity. *Ieee Transactions on Geoscience and Remote Sensing*, **50**, 1662–1675 (2012).
- Brandt, P., G. Caniaux, B. Bourles, A. Lazar, M. Dengler, A. Funk, V. Hormann, H. Giordani and F. Marin: Equatorial upper-ocean dynamics and their interaction with the West African monsoon. *Atmospheric Science Letters*, **12**, 24–30 (2011).
- Brandt, P., V. Hormann, A. Koertzing, M. Visbeck, G. Krahmann, L. Stramma, R. Lumpkin and C. Schmid: Changes in the Ventilation of the Oxygen Minimum Zone of the Tropical North Atlantic. *Journal of Physical Oceanography*, **40**, 1784–1801 (2010).
- Brandt, P., D. A. Martinez, M. Dengler, S.-H. Didwischus, A. Funk, J. Hahn, B. Hogue, T. Kemena, A. Kock, G. Krahmann, W. Martens, N. Martogli, M. Müller, G. Niehus, U. Papenburg, A. Pinck, K. Rother, M. Schlundt, F. Schütte, S. Tippenhauer, M. Vogt and R. J. Zantopp (2012): *Physical and Biogeochemical Studies in the Subtropical and Tropical Atlantic*. Fahrtbericht, Hamburg, Germany, URL <http://oceanrep.geomar.de/20727/>.
- Brandt, P., F. A. Schott, C. Provost, A. Kartavtseff, V. Hormann, B. Bourlès and J. Fischer: Circulation in the central equatorial atlantic: Mean and intraseasonal to seasonal variability. *Geophysical Research Letters*, **33**, L07609 (2006).
- Bumke, K., K. Fennig, A. Strehz, R. Mecking and M. Schroder: HOAPS precipitation validation with ship-borne rain gauge measurements over the Baltic Sea. *Tellus Series a-Dynamic Meteorology and Oceanography*, **64** (2012).
- Bumke, K., M. Schlundt, J. Kalisch, A. Macke and H. Kleta: Measured and Parameterized Energy Fluxes Estimated for Atlantic Transects of R/V Polarstern. *Journal of Physical Oceanography*, **44**, 482–491 (2014).
- Bumke, K. and J. Seltmann: Analysis of Measured Drop Size Spectra over Land and Sea. *ISRN Meteorology*, **2012**, 10 (2012).
- Caniaux, G., H. Giordani, J. L. Redelsperger, F. Guichard, E. Key and M. Wade: Coupling between the Atlantic cold tongue and the West African monsoon in boreal spring and summer. *Journal of Geophysical Research: Oceans*, **116** (2011).
- Carton, J. A. and Z. X. Zhou: Annual cycle of sea surface temperature in the tropical Atlantic ocean. *Journal of Geophysical Research: Oceans*, **102**, 27813–27824 (1997).
- Chang, P.: Seasonal cycle of sea surface temperature and mixed layer heat budget in the tropical Pacific Ocean. *Geophysical Research Letters*, **20**, 2079–2082 (1993).

- Chelton, D. B., S. K. Esbensen, M. G. Schlax, N. Thum, M. H. Freilich, F. J. Wentz, C. L. Gentemann, M. J. McPhaden and P. S. Schopf: Observations of coupling between surface wind stress and sea surface temperature in the eastern tropical Pacific. *Journal of Climate*, **14** (2001).
- Coëtlogon, G. d., S. Janicot and A. Lazar: Intraseasonal variability of the ocean—atmosphere coupling in the Gulf of Guinea during boreal spring and summer. *Quarterly Journal of the Royal Meteorological Society*, **136**, 426–441 (2010).
- Curry, R., B. Dickson, I. Yashayaev *et al.*: A change in the freshwater balance of the Atlantic Ocean over the past four decades. *Nature*, **426**, 826–829 (2003).
- Da-Allada, C. Y., G. Alory, Y. du Penhoat, E. Kestenare, F. Durand and N. M. Hounkonnou: Seasonal mixed-layer salinity balance in the tropical Atlantic Ocean: Mean state and seasonal cycle. *Journal of Geophysical Research: Oceans*, **118**, 332–345 (2013), URL <http://dx.doi.org/10.1029/2012JC008357>.
- da Silva, A. M., C. C. Young and S. Levitus: Atlas of surface marine data 1994, vol. 1: Algorithms and procedures. *NOAA Atlas NESDIS*, **6** (1994).
- de Boyer Montegut, C., G. Madec, A. S. Fischer, A. Lazar and D. Iudicone: Mixed layer depth over the global ocean: An examination of profile data and a profile-based climatology. *Journal of Geophysical Research: Oceans*, **109** (2004).
- de Boyer Montegut, C., J. Mignot, A. Lazar and S. Cravatte: Control of salinity on the mixed layer depth in the world ocean: 1. General description. *Journal of Geophysical Research: Oceans*, **112** (2007).
- Dee, D. P., S. M. Uppala, A. J. Simmons, P. Berrisford, P. Poli, S. Kobayashi, U. Andrae, M. A. Balmaseda, G. Balsamo, P. Bauer, P. Bechtold, A. C. M. Beljaars, L. van de Berg, J. Bidlot, N. Bormann, C. Delsol, R. Dragani, M. Fuentes, A. J. Geer, L. Haimberger, S. B. Healy, H. Hersbach, E. V. Holm, L. Isaksen, P. Kallberg, M. Kohler, M. Matricardi, A. P. McNally, B. M. Monge-Sanz, J. J. Morcrette, B. K. Park, C. Peubey, P. de Rosnay, C. Tavolato, J. N. Thepaut and F. Vitart: The ERA-Interim reanalysis: configuration and performance of the data assimilation system. *Quarterly Journal of the Royal Meteorological Society*, **137**, 553–597 (2011).
- Delcroix, T. and C. Henin: Seasonal and interannual variations of sea surface salinity in the tropical Pacific Ocean. *Journal of Geophysical Research: Oceans*, **96**, 22135–22150 (1991).
- Dessier, A. and J. R. Donguy: The sea surface salinity in the tropical Atlantic between 10 S and 30 N - Seasonal and interannual variations (1977-1989). *Deep-Sea Research Part I: Oceanographic Research Papers*, **41**, 81–100 (1994).
- Durack, P. J. and S. E. Wijffels: Fifty-Year Trends in Global Ocean Salinities and Their Relationship to Broad-Scale Warming. *Journal of Climate*, **23**, 4342–4362 (2010).

- Düing, W., P. Hisard, E. Katz, J. Meincke, L. Miller, K. V. Moroshkin, G. Philander, A. A. Ribnikov, K. Voigt and R. Weisberg: Meanders and long waves in the equatorial Atlantic. *Nature*, **257**, 280–284 (1975).
- Fahrbach, E., J. Meincke and A. Sy: Observations of the horizontal separation of the salinity core and the current core in the Atlantic equatorial undercurrent. *Journal of Marine Research*, **44**, 763–779 (1986).
- Fairall, C. W., E. F. Bradley, J. E. Hare, A. A. Grachev and J. B. Edson: Bulk parameterization of air-sea fluxes: Updates and verification for the COARE algorithm. *Journal of Climate*, **16**, 571–591 (2003).
- Ferrari, R. and K. L. Polzin: Finescale structure of the T-S relation in the eastern North Atlantic. *Journal of Physical Oceanography*, **35**, 1437–1454 (2005).
- Foltz, G. R., S. A. Grodsky, J. A. Carton and M. J. McPhaden: Seasonal mixed layer heat budget of the tropical Atlantic Ocean. *Journal of Geophysical Research: Oceans*, **108** (2003).
- Foltz, G. R., S. A. Grodsky, J. A. Carton and M. J. McPhaden: Seasonal salt budget of the northwestern tropical Atlantic Ocean along 38 degrees W. *Journal of Geophysical Research: Oceans*, **109** (2004).
- Foltz, G. R. and M. J. McPhaden: Seasonal mixed layer salinity balance of the tropical North Atlantic Ocean. *Journal of Geophysical Research: Oceans*, **113** (2008).
- Foltz, G. R., M. J. McPhaden and R. Lumpkin: A Strong Atlantic Meridional Mode Event in 2009: The Role of Mixed Layer Dynamics. *Journal of Climate*, **25**, 363–380 (2012).
- Foltz, G. R., C. Schmid and R. Lumpkin: Seasonal Cycle of the Mixed Layer Heat Budget in the Northeastern Tropical Atlantic Ocean. *Journal of Climate*, **26**, 8169–8188 (2013).
- Font, J., J. Boutin, N. Reul, P. Spurgeon, J. Ballabrera-Poy, A. Chuprin, C. Gabarró, J. Gourrion, S. Guimard, C. Hénocq *et al.*: SMOS first data analysis for sea surface salinity determination. *International Journal of Remote Sensing*, **34**, 3654–3670 (2013).
- Font, J., G. Lagerloef, Y. Kerr, N. Skou and M. Berger: Sea surface salinity mapping with SMOS space mission. *Elsevier Oceanography Series*, **69**, 186–189 (2003).
- Ganachaud, A. and C. Wunsch: Improved estimates of global ocean circulation, heat transport and mixing from hydrographic data. *Nature*, **408**, 453–457 (2000).
- Garau, B., S. Ruiz, W. F. G. Zhang, A. Pascual, E. Heslop, J. Kerfoot and J. Tintore: Thermal Lag Correction on Slocum CTD Glider Data. *Journal of Atmospheric and Oceanic Technology*, **28**, 1065–1071 (2011).



- Giordani, H., G. Caniaux and A. Voldoire: Intraseasonal mixed-layer heat budget in the equatorial Atlantic during the cold tongue development in 2006. *Journal of Geophysical Research: Oceans*, **118**, 650–671 (2013).
- Goes, M., G. Goni, V. Hormann and R. C. Perez: Variability of the atlantic off-equatorial eastward currents during 1993–2010 using a synthetic method. *Journal of Geophysical Research: Oceans*, **118**, 3026–3045 (2013).
- Gouriou, Y. and G. Reverdin: Isopycnal and diapycnal circulation of the upper equatorial Atlantic Ocean in 1983–1984. *Journal of Geophysical Research: Oceans*, **97**, 3543–3572 (1992).
- Grodsky, S. A. and J. A. Carton: Intense surface currents in the tropical Pacific during 1996–1998. *Journal of Geophysical Research: Oceans*, **106**, 16673–16684 (2001).
- Großklaus, M., K. Uhlig and L. Hasse: An optical disdrometer for use in high wind speeds. *Journal of Atmospheric and Oceanic Technology*, **15**, 1051–1059 (1998).
- Hall, A. and S. Manabe: Can local linear stochastic theory explain sea surface temperature and salinity variability? *Climate Dynamics*, **13**, 167–180 (1997).
- Hansen, D. V. and A. Herman: Evolution of isotherm depth anomalies in the eastern tropical Pacific Ocean during the El Nino event of 1982–1983. *Journal of Geophysical Research: Oceans*, **94**, 14461–14473 (1989).
- Hansen, D. V. and C. A. Paul: Genesis and effects of long waves in the equatorial Pacific. *Journal of Geophysical Research: Oceans*, **89**, 431–440 (1984).
- Hasse, L., M. Grossklaus, K. Uhlig and P. Timm: A ship rain gauge for use in high wind speeds. *Journal of Atmospheric and Oceanic Technology*, **15**, 380–386 (1998).
- Hayes, S. P., P. Chang and M. J. McPhaden: Variability of the sea surface temperature in the eastern equatorial Pacific during 1986–1988. *Journal of Geophysical Research: Oceans*, **96**, 10553–10566 (1991).
- Hisard, P. and A. Morlière: La terminaison du contre courant équatorial subsuperficiel Atlantique (courant de Lomonosov) dans le golfe de Guinée. *Cahiers ORSTOM Series Oceanographique*, **XI**, **4**, 455–464 (1973).
- Hormann, V. and P. Brandt: Atlantic Equatorial Undercurrent and associated cold tongue variability. *Journal of Geophysical Research: Oceans*, **112** (2007).
- Hosoda, S., T. Ohira and T. Nakamura: A monthly mean dataset of global oceanic temperature and salinity derived from Argo float observations. *JAMSTEC Report of Research and Development*, **8**, 47–59 (2008).
- Hummels, R., M. Dengler and B. Bourlès: Seasonal and regional variability of upper ocean diapycnal heat flux in the Atlantic cold tongue. *Progress in Oceanography*, **111**, 52–74 (2013).

- Hummels, R., M. Dengler, P. Brandt and M. Schlundt: Diapycnal heat flux and mixed layer heat budget within the Atlantic Cold Tongue. *submitted to Climate Dynamics* (2014).
- Jochum, M., M. F. Cronin, W. S. Kessler and D. Shea: Observed horizontal temperature advection by tropical instability waves. *Geophysical Research Letters*, **34** (2007).
- Johns, W., P. Brandt, B. Bourlès, A. Tantet, A. Papapostolou and A. Houk: Zonal structure and seasonal variability of the Atlantic Equatorial Undercurrent. *Climate Dynamics*, pp. 1–23 (2014).
- Johnson, E. S., F. Bonjean, G. S. E. Lagerloef, J. T. Gunn and G. T. Mitchum: Validation and Error Analysis of OSCAR Sea Surface Currents. *Journal of Atmospheric and Oceanic Technology*, **24**, 688–701 (2007).
- Jouanno, J., F. Marin, Y. Du Penhoat, J. M. Molines and J. Sheinbaum: Seasonal Modes of Surface Cooling in the Gulf of Guinea. *Journal of Physical Oceanography*, **41**, 1408–1416 (2011a).
- Jouanno, J., F. Marin, Y. du Penhoat, J. Sheinbaum and J.-M. Molines: Seasonal heat balance in the upper 100 m of the equatorial Atlantic Ocean. *Journal of Geophysical Research*, **116**, C09003 (2011b).
- Kalisch, J. and A. Macke: Radiative budget and cloud radiative effect over the Atlantic from ship-based observations. *Atmospheric Measurement Techniques*, **5**, 2391–2401 (2012).
- Kanamitsu, M., W. Ebisuzaki, J. Woollen, S. Yang, J. Hnilo, M. Fiorino and G. Potter: NCEP-DOE AMIP-II Reanalysis (R-2). *Bulletin of the American Meteorological Society*, **83**, 1631–1644 (2002).
- Karstensen, J. and D. Quadfasel: Formation of Southern Hemisphere thermocline waters: Water mass conversion and subduction. *Journal of Physical Oceanography*, **32** (2002).
- Kinzel, J. (2013): *Validation of HOAPS latent heat fluxes against parameterizations applied to RV Polarstern data for 1995-1997*. Master thesis, Christian-Albrechts-Universität Kiel, Kiel, Germany.
- Kolodziejczyk, N., B. Bourlès, F. Marin, J. Grelet and R. Chuchla: Seasonal variability of the Equatorial Undercurrent at 10°W as inferred from recent in situ observations. *Journal of Geophysical Research: Oceans*, **114**, C06014 (2009).
- Kolodziejczyk, N., F. Marin, B. Bourlès, Y. Gouriou and H. Berger: Seasonal variability of the equatorial undercurrent termination and associated salinity maximum in the Gulf of Guinea. *Climate Dynamics*, pp. 1–22 (2014).

- Körtzinger, A. (2011): *Short Cruise Report RV MARIA S. MERIAN Cruise MSM18-3 Mindelo - Libreville 22 June - 21 July 2011*. Fahrtbericht doi:10.3289/SCR\_MSM\_18\_3, Kiel, Germany, URL <http://oceanrep.geomar.de/13649/>.
- Kraus, E. B.: The Evaporation-Precipitation Cycle of the Trades. *Tellus*, **11**, 147–158 (1959).
- Kubota, M., A. Kano, H. Muramatsu and H. Tomita: Intercomparison of various surface latent heat flux fields. *Journal of Climate*, **16**, 670–678 (2003).
- Kuhlbrodt, T., A. Griesel, M. Montoya, A. Levermann, M. Hofmann and S. Rahmstorf: On the driving processes of the Atlantic meridional overturning circulation. *Reviews of Geophysics*, **45** (2007).
- Lagerloef, G. S. E., F. R. Colomb, D. Le Vine, F. Wentz, S. Yueh, C. Ruf, J. Lilly, J. Gunn, Y. Chao, A. deCharon, G. Feldman and C. Swift: The Aquarius/SAC-D Mission: Designed to meet the salinity remote-sensing challenge. *Oceanography*, **21**, 68–81 (2008).
- Lagerloef, G. S. E., G. T. Mitchum, R. B. Lukas and P. P. Niiler: Tropical Pacific near-surface currents estimated from altimeter, wind, and drifter data. *Journal of Geophysical Research: Oceans*, **104**, 23313–23326 (1999).
- Lebedev, K. V., H. Yoshinari, N. A. Maximenko and P. W. Hacker: YoMaHa'07: Velocity data assessed from trajectories of Argo floats at parking level and at the sea surface. *IPRC Technical Note*, **4**, 1–16 (2007).
- Lee, T., G. S. E. Lagerloef, M. M. Gierach, H. Y. Kao, S. Yueh and K. Dohan: Aquarius reveals salinity structure of tropical instability waves. *Geophysical Research Letters*, **39** (2012).
- Legeckis, R.: Long Waves in the Eastern Equatorial Pacific Ocean: A View from a Geostationary Satellite. *Science*, **197**, 1179–1181 (1977).
- Lellouche, J. M., O. Le Galloudec, M. Drevillon, C. Regnier, E. Greiner, G. Garric, N. Ferry, C. Desportes, C. E. Testut, C. Bricaud, R. Bourdalle-Badie, B. Tranchant, M. Benkiran, Y. Drillet, A. Daudin and C. De Nicola: Evaluation of global monitoring and forecasting systems at Mercator Ocean. *Ocean Science*, **9**, 57–81 (2013).
- Lien, R. C., E. A. D'Asaro and C. E. Menkes: Modulation of equatorial turbulence by tropical instability waves. *Geophysical Research Letters*, **35** (2008).
- Locarnini, R. A., A. V. Mishonov, J. I. Antonov, T. P. Boyer, H. E. Garcia, O. K. Baranova, M. M. Zweng and D. R. Johnson: World Ocean Atlas 2009, vol. 1, Temperature, edited by S. Levitus. *NOAA Atlas NESDIS*, **68** (2010).
- Lumpkin, R. and S. L. Garzoli: Near-surface circulation in the tropical Atlantic Ocean. *Deep Sea Research Part I: Oceanographic Research Papers*, **52**, 495–518 (2005).

- Marin, F., G. Caniaux, B. Bourlès, H. Giordani, Y. Gouriou and E. Key: Why were sea surface temperatures so different in the eastern equatorial Atlantic in June 2005 and 2006? *Journal of Physical Oceanography*, **39** (2009).
- McCreary, J. P. and P. Lu: Interaction between the subtropical and equatorial ocean circulations: The subtropical cell. *Journal of Physical Oceanography*, **24**, 466–497 (1994).
- Moum, J. N., D. R. Caldwell and C. A. Paulson: Mixing in the equatorial surface layer and thermocline. *Journal of Geophysical Research: Oceans*, **94**, 2005–2021 (1989).
- Munk, W. and C. Wunsch: Abyssal recipes II: Energetics of tidal and wind mixing. *Deep-Sea Research Part I*, **45**, 1977–2010 (1998).
- Oakey, N. S.: Determination of the rate of dissipation of turbulent energy from simultaneous temperature and velocity shear microstructure measurements. *Journal of Physical Oceanography*, **12**, 256–271 (1982).
- Okumura, Y. and S.-P. Xie: Some overlooked features of tropical Atlantic climate leading to a new Niño-like phenomenon. *Journal of climate*, **19** (2006).
- Osborn, T. R.: Estimates of the local rate of vertical diffusion from dissipation measurements. *Journal of Physical Oceanography*, **10**, 83–89 (1980).
- Osborn, T. R. and C. S. Cox: Oceanic fine structure. *Geophysical & Astrophysical Fluid Dynamics*, **3**, 321–345 (1972).
- Perez, R. C., V. Hormann, R. Lumpkin, P. Brandt, W. E. Johns, F. Hernandez, C. Schmid and B. Bourlès: Mean meridional currents in the central and eastern equatorial Atlantic. *Climate Dynamics* (2013).
- Peter, A. C., M. Le Henaff, Y. du Penhoat, C. E. Menkes, F. Marin, J. Vialard, G. Caniaux and A. Lazar: A model study of the seasonal mixed layer heat budget in the equatorial Atlantic. *Journal of Geophysical Research: Oceans*, **111** (2006).
- Peters, H., M. C. Gregg and J. M. Toole: On the parameterization of equatorial turbulence. *Journal of Geophysical Research: Oceans*, **93**, 1199–1218 (1988).
- Philander, S. (1990): *El Niño, La Niña, and the southern oscillation*, Vol. 46. Academic Press.
- Philander, S. G. H.: Instabilities of zonal equatorial currents, 2. *Journal of Geophysical Research: Oceans*, **83**, 3679–3682 (1978).
- Philander, S. G. H., D. Gu, D. Halpern, G. Lambert, N. C. Lau, T. Li and R. C. Pacanowski: Why the ITCZ is mostly north of the equator. *Journal of Climate*, **9**, 2958–2972 (1996).
- Philander, S. G. H. and R. C. Pacanowski: The oceanic response to cross-equatorial winds (with application to coastal upwelling in low latitudes). *Tellus*, **33**, 201–210 (1981).

- Prandke, H. and A. Stips: Test measurements with an operational microstructure-turbulence profiler: Detection limit of dissipation rates. *Aquatic Sciences*, **60**, 191–209 (1998).
- Praveen Kumar, B., J. Vialard, M. Lengaigne, V. Murty and M. McPhaden: TropFlux: air-sea fluxes for the global tropical oceans—description and evaluation. *Climate Dynamics*, **38**, 1521–1543 (2012), URL <http://dx.doi.org/10.1007/s00382-011-1115-0>.
- Qiu, B. and R. X. Huang: Ventilation of the North Atlantic and North Pacific: subduction versus obduction. *Journal of Physical Oceanography*, **25**, 2374–2390 (1995).
- Reul, N., J. Tenerelli, J. Boutin, B. Chapron, F. Paul, E. Brion, F. Gaillard and O. Archer: Overview of the First SMOS Sea Surface Salinity Products. Part I: Quality Assessment for the Second Half of 2010. *Ieee Transactions on Geoscience and Remote Sensing*, **50**, 1636–1647 (2012).
- Reynolds, R. W. and T. M. Smith: Improved global sea surface temperature analyses using optimum interpolation. *Journal of Climate*, **7**, 929–948 (1994).
- Rhein, M., M. Dengler, J. Sültenfuß, R. Hummels, S. Hüttl-Kabus and B. Bourles: Upwelling and associated heat flux in the equatorial Atlantic inferred from helium isotope disequilibrium. *Journal of Geophysical Research: Oceans*, **115**, C08021 (2010).
- Richardson, P. and G. Reverdin: Seasonal cycle of velocity in the Atlantic North Equatorial Countercurrent as measured by surface drifters, current meters, and ship drifts. *Journal of Geophysical Research*, **92**, 3691–3708 (1987).
- Sandström, J. W.: Dynamische Versuche mit Meerwasser. *Ann. Hydrogr. Mar. Meteorol*, **36**, 6–23 (1908).
- Schafstall, J., M. Dengler, P. Brandt and H. W. Bange: Tidal-induced mixing and diapycnal nutrient fluxes in the Mauritanian upwelling region. *Journal of Geophysical Research: Oceans*, **115** (2010).
- Schmitt, R. W., P. S. Bogden and C. E. Dorman: Evaporation Minus Precipitation and Density Fluxes for the North Atlantic. *Journal of Physical Oceanography*, **19**, 1208–1221 (1989).
- Schmitt, R. W., J. R. Ledwell, E. T. Montgomery, K. L. Polzin and J. M. Toole: Enhanced diapycnal mixing by salt fingers in the thermocline of the tropical Atlantic. *Science*, **308**, 685–688 (2005).
- Schott, F., J. McCreary Jr and G. Johnson: Shallow overturning circulations of the tropical-subtropical oceans. *Geophysical Monograph Series*, **147**, 261–304 (2004).
- Seager, R., S. E. Zebiak and M. A. Cane: A model of the tropical Pacific sea surface temperature climatology. *Journal of Geophysical Research: Oceans*, **93**, 1265–1280 (1988).

- Stevenson, J. W. and P. P. Niiler: Upper ocean heat budget during the Hawaii-to-Tahiti shuttle experiment. *Journal of Physical Oceanography*, **13**, 1894–1907 (1983).
- Stramma, L. and F. Schott: The mean flow field of the tropical Atlantic Ocean. *Deep-Sea Research Part II: Topical Studies in Oceanography*, **46**, 279–303 (1999).
- Sverdrup, H. U.: Wind-driven currents in a baroclinic ocean; with application to the equatorial currents of the eastern Pacific. *Proceedings of the National Academy of Sciences of the United States of America*, **33**, 318 (1947).
- Swenson, M. S. and D. V. Hansen: Tropical Pacific Ocean mixed layer heat budget: The Pacific cold tongue. *Journal of Physical Oceanography*, **29**, 69–81 (1999).
- Taylor, J., J. Edwards, M. Glew, P. Hignett and A. Slingo: Studies with a flexible new radiation code. II: Comparisons with aircraft short-wave observations. *Quarterly Journal of the Royal Meteorological Society*, **122**, 839–861 (1996).
- Toggweiler, J. and B. Samuels: On the ocean’s large-scale circulation near the limit of no vertical mixing. *Journal of Physical Oceanography*, **28**, 1832–1852 (1998).
- Trenberth, K. E., L. Smith, T. Qian, A. Dai and J. Fasullo: Estimates of the global water budget and its annual cycle using observational and model data. *Journal of Hydrometeorology*, **8** (2007).
- Tzortzi, E., S. A. Josey, M. Srokosz and C. Gommenginger: Tropical Atlantic salinity variability: New insights from SMOS. *Geophysical Research Letters*, **40**, 2143–2147 (2013), URL <http://dx.doi.org/10.1002/grl.50225>.
- von Schuckmann, K., P. Brandt and C. Eden: Generation of tropical instability waves in the Atlantic Ocean. *Journal of Geophysical Research*, **113**, C08034 (2008).
- Wade, M., G. Caniaux and Y. du Penhoat: Variability of the mixed layer heat budget in the eastern equatorial Atlantic during 2005–2007 as inferred using Argo floats. *Journal of Geophysical Research: Oceans*, **116** (2011).
- Wallace, J. M., T. Mitchell and C. Deser: The influence of sea-surface temperature on surface wind in the eastern equatorial Pacific: Seasonal and interannual variability. *Journal of Climate*, **2**, 1492–1499 (1989).
- Wang, W. M. and M. J. McPhaden: The surface-layer heat balance in the equatorial Pacific Ocean. Part I: Mean seasonal cycle. *Journal of Physical Oceanography*, **29**, 1812–1831 (1999).
- Wyrtki, K.: An estimate of equatorial upwelling in the Pacific. *Journal of Physical Oceanography*, **11**, 1205–1214 (1981).
- Xie, P. and P. A. Arkin: Global precipitation: A 17-year monthly analysis based on gauge observations, satellite estimates, and numerical model outputs. *Bulletin of the American Meteorological Society*, **78**, 2539–2558 (1997).

- Xie, S. P. and J. A. Carton: Tropical Atlantic variability: Patterns, mechanisms, and impacts. *Geophysical Monograph Series*, **147**, 121–142 (2004).
- Yu, L.: A global relationship between the ocean water cycle and near-surface salinity. *Journal of Geophysical Research: Oceans (1978–2012)*, **116** (2011).
- Yu, L., X. Jin and R. Weller (2008): *Multidecade Global Flux Datasets from the Objectively Analyzed Air-sea Fluxes (OAFlux) Project: Latent and Sensible Heat Fluxes, Ocean Evaporation, and Related Surface Meteorological Variables*. Tech. rep., OAFlux Project Tech. Rep. OA-2008-01.
- Zhang, D., M. J. McPhaden and W. E. Johns: Observational Evidence for Flow between the Subtropical and Tropical Atlantic: The Atlantic Subtropical Cells\*. *Journal of Physical Oceanography*, **33**, 1783–1797 (2003).





# List of Figures

1.1	Hydrological cycle. . . . .	2
1.2	MOC. . . . .	2
1.3	Mixed layer schematic. . . . .	4
2.1	Annual mean sea surface temperature from WOA2009. . . . .	9
2.2	Monthly mean sea surface temperature climatology from TMI. . . . .	10
2.3	Meridional section of annual mean temperature . . . . .	11
2.4	Annual mean sea surface salinity from WOA2009. . . . .	12
2.5	Monthly mean sea surface salinity climatology from SMOS. . . . .	14
2.6	Meridional section of annual mean salinity . . . . .	15
2.7	Hovmoeller plot of mean seasonal cycle. . . . .	18
2.8	Circulation in the Atlantic. . . . .	20
2.9	Meridional section of mean zonal velocity. . . . .	22
3.1	Definition of boxes. . . . .	25
3.2	Cold tongue experiment conducted between May and July 2011. . . . .	27
3.3	Overview of glider deployment times. . . . .	28
3.4	Position of Argo floats and PIRATA buoys. . . . .	30
3.5	Comparison of ship data and reanalysis and satellite data. . . . .	33
3.6	Comparison of ship data and reanalysis and satellite data. . . . .	34
3.7	Scatter plots of SST and SSS. . . . .	36
3.8	Zonal and meridional velocities at the equator at 23°W and at 10°W. . . . .	39
3.9	Box-averaged zonal advection from satellite and model. . . . .	44
3.10	Box-averaged meridional advection from satellite and model. . . . .	45
4.1	Seasonal cycle of SST and SSS at PIRATA at 23°W and 10°W. . . . .	52
4.2	Monthly mean SST and SSS in summer 2011. . . . .	54
4.3	Monthly mean zonal temperature advection in 2011. . . . .	55
4.4	Monthly mean zonal salinity advection in 2011. . . . .	57
4.5	Monthly mean surface winds and precipitation in summer 2011. . . . .	58
4.6	Time series of glider ifm02. . . . .	59
4.7	Time series of glider ifm11. . . . .	60
4.8	Time series of glider ifm09. . . . .	61
4.9	MLS from glider, CTD and Argo float profiles. . . . .	62
4.10	Meridional section of salinity and zonal velocity at 23°W. . . . .	63
4.11	Meridional section of salinity and zonal velocity at 10°W in May. . . . .	64
4.12	Meridional section of salinity and zonal velocity at 10°W in July. . . . .	65

4.13	Maximum salinity in the TL from glider, CTD, and Argo float profiles. . .	66
4.14	Salinity differences between ML and TL . . . . .	68
4.15	Dissipation rates and diapycnal diffusivities . . . . .	69
4.16	Vertical temperature and salinity gradient . . . . .	70
4.17	Diapycnal heat and salt flux . . . . .	71
5.1	MLD, MLS, and MLT during the CTE. . . . .	74
5.2	Heat budget in the ACT. . . . .	75
5.3	Heat budget in the ACT. . . . .	77
5.4	Heat budget in the northern box. . . . .	77
5.5	salinity budget in the ACT. . . . .	79
5.6	salinity budget in the ACT. . . . .	80
5.7	salinity budget in the northern box. . . . .	81
6.1	Seasonal cycles at 0°N,23°W. . . . .	94
6.2	Seasonal cycles and ML salinity budget at 0°N,23°W. . . . .	96
6.3	Same as figure 6.1, but at 0°N, 10°W. . . . .	98
6.4	Same as figure 6.2, but at 0°N, 10°W. . . . .	100
6.5	Same as figure 6.1, but at 4°N, 23°W. . . . .	102
6.6	Same as figure 6.2, but at 4°N, 23°W. . . . .	104

# List of Tables

3.1	Amount of profiles for every glider deployment. . . . .	29
3.2	Depth coverage at PIRATA buoys. . . . .	31
3.3	Bias, std and rmsd between atmospheric datasets. . . . .	35
3.4	Annual mean and std of regression coefficients between SSSs and SSTs. .	48
5.1	Diapycnal diffusivities. . . . .	84



# Danksagung

Größter Dank gilt meinem Betreuer Prof. Dr. Peter Brandt für das in mich gesetzte Vertrauen, die Hilfe und den Glauben diese Doktorarbeit zu meistern. Nicht zuletzt habe ich von dem unglaublichen Fachwissen profitiert und oftmals war auch eine Kurskorrektur zum rechten Zeitpunkt hilfreich.

Ich danke Prof. Dr. Claus Böning für die Bereitschaft als Zweitgutachter und Kommissionsmitglied zu fungieren.

Unzählige Kollegen haben mich in verschiedenster Weise begleitet. Da wären zum einen meine Chefs Jürgen Fischer und Johannes Kastensen, wie auch meine Koautoren Marcus Dengler, Gerd Krahmann, Tim Fischer, Rebecca Hummels und Karl Bumke, die mir alle mit Rat und Tat zur Seite standen. Der B11-Crew in verschiedenster Besetzung danke ich für eine super Arbeitsatmosphäre und auch alle anderen Mitarbeiter der PO inklusive der Technikercrew sowie viele weitere sollen nicht zu kurz kommen. Natürlich soll auch Arne Körtzinger als Fahrtleiter gedankt werden, der mir die Teilnahme an einer seiner Seereisen ermöglichte.

Den Dank an Jana und Cathleen kann man nicht in Worte fassen, aber um es zu versuchen: Danke vor allem fürs Ertragen und das ungezählte Lesen von Fragmenten in den letzten Zügen der Arbeit .

Ein paar Projekte sollen auch erwähnt werden, zwischen denen ich in den Jahren hin und her sprang und die es ermöglichten dass man zwischendurch auch mal Mittagessen gehen konnte: Euro-Argo, SFB754, Nordatlantik, SOPRAN, GROOM und SACUS.

Diese Arbeit wurde mit der Textverarbeitung  $\text{\LaTeX}$  angefertigt.



## **Erklärung**

Hiermit erkläre ich, dass ich die vorliegende Arbeit - abgesehen von der Beratung durch meinen Betreuer - unter Einhaltung der Regeln guter wissenschaftlicher Praxis der Deutschen Forschungsgemeinschaft selbständig erarbeitet und verfasst habe. Diese Arbeit hat weder ganz, noch zum Teil, an anderer Stelle im Rahmen eines Prüfungsverfahrens vorgelegen, ist nicht veröffentlicht und auch nicht zur Veröffentlichung eingereicht.

Kiel, April 2014

---

(Michael Schlundt)